

**In operando phase transition and
lithium ion transportation in
 LiFePO_4**

Xiaoyu Zhang

张晓禹

In operando phase transitions and Lithium ion transport in LiFePO_4

Proefschrift

ter verkrijging van de graad van doctor

aan de Technische Universiteit Delft,

op gezag van de Rector Magnificus prof. Ir. K.C.A.M. Luyben;

voorzitter van het College voor Promoties,

in het openbaar te verdedigen op

Woensdag 11 November 2015 om 10:00 uur

Door

Xiaoyu Zhang

Master in Condensed Matter Physics, Nanjing University of

Aeronautics and Astronautics , geboren te Xuzhou, Jiangsu

province, China

This dissertation has been approved by the promotor:

Prof. dr. F. M. Mulder

copromotor: Dr.Ir. M. Wagemaker

Composition of the doctoral committee:

Rector Magnificus

Prof. dr. F. M. Mulder Technische Universiteit Delft, promotor

Dr. Ir. M. Wagemaker Technische Universiteit Delft, copromotor

Independent members:

Prof. dr. Ir. E.H.Brück Technische Universiteit Delft

Prof. dr. S.J. Picken Technische Universiteit Delft

Dr. Ir. N. H. van Dijk Technische Universiteit Delft

Prof. dr. Ir. J. E. ten Elshof Universiteit Twente

Prof. dr. C. Masquelier Université de Picardie Jules Verne, France



This research carried out in this thesis was financially supported by the China Scholarship Council (CSC)

ISBN: 978-90-8593-235-2

Copyright © 2015 by Xiaoyu Zhang (张晓禹)

All right reserve. No part of the material protected by this copyright notice may be reproduced or utilized in any form or by any means, electronic or mechanical, including photocopying, recording or by any information storage and retrieval system, without the prior permission of the author. (Author email: xiaoyuzhang0724@gmail.com)

Printed in The Netherlands by Uitgeverij BOXPress

Dedicate to my parents

献给我的父母

Contents

CHAPTER 1 INTRODUCTION	1
1.1 GENERAL INTRODUCTION OF LI-ION BATTERIES	1
1.2 CATHODE MATERIALS	4
1.2.1 <i>Progress of fundamental LiFePO₄ research</i>	4
1.3 ANODE MATERIALS	7
1.4 OUTLINE OF THIS THESIS: SCIENTIFIC QUESTIONS AND THE TECHNIQUES INVOLVED	8
REFERENCES	12
CHAPTER 2 EXPERIMENTAL TECHNIQUES.....	15
2.1 2D-XRD DIFFRACTION	15
2.1.1 <i>Experiment set up</i>	15
2.1.2 <i>Theory of 2D-XRD diffraction microscopy</i>	17
2.2 NEUTRON DEPTH PROFILING (NDP).....	18
2.2.1 <i>Introduction</i>	18
2.2.2 <i>NDP data analysis</i>	20
REFERENCES	23
CHAPTER 3 RATE INDUCED SOLUBILITY AND SUPPRESSION OF THE FIRST- ORDER PHASE TRANSITION IN OLIVINE LiFePO₄	25
3.1 INTRODUCTION	26
3.2 EXPERIMENT METHOD	28
3.3 RESULTS AND DISCUSSION	29
3.4 CONCLUSIONS	40
REFERENCES	41
CHAPTER 4 DIRECT VIEW ON THE PHASE EVOLUTION IN INDIVIDUAL LiFePO₄ NANOPARTICLES DURING CYCLING OF LI-ION BATTERY ELECTRODES.....	47
4.1 INTRODUCTION	48

4.2 EXPERIMENTAL METHODS	51
4.3 ANALYTICAL METHODS	52
4.4 RESULTS AND DISCUSSION	55
4.5 CONCLUSIONS	65
REFERENCES	68
CHAPTER 5 DIRECT OBSERVATION OF LI-ION TRANSPORT IN ELECTRODE UNDER NON-EQUILIBRIUM CONDITION USING NEUTRON DEPTH PROFILING.....	71
5.1 INTRODUCTION.....	72
5.2 EXPERIMENTAL AND ANALYTICAL METHOD	76
5.2.1 <i>Sample Preparation And Experiment Method.....</i>	76
5.2.2 <i>Depth Calibration</i>	77
5.2.3 <i>Intensity Calibration</i>	78
5.2.4 <i>Ex-situ measurements.....</i>	80
5.2.5 <i>Electrospray electrode preparation.....</i>	81
5.3 RESULTS AND DISCUSSION	82
5.4 CONCLUSIONS	95
REFERENCES	96
CHAPTER 6 MAGNÉLI-PHASE Ti_4O_7 AS NEGATIVE ELECTRODE FOR LI-ION BATTERIES.....	101
6.1 INTRODUCTION.....	102
6.2 METHODS	103
6.2.1 <i>Density Functional Theory.....</i>	103
6.2.2 <i>Sample preparation.....</i>	104
6.3 RESULTS.....	105
6.3.1 <i>DFT calculations</i>	105
6.3.2 <i>Electrochemical Tests.....</i>	108
6.4 DISCUSSION	110
6.5 CONCLUSIONS	113
REFERENCES	114
SUMMARY	117
SAMENVATTING	121

ACKNOWLEDGEMENT	125
LIST OF PUBLICATIONS	133
CURRICULUM VITAE	135

Chapter 1

Introduction

1.1 General introduction of Li-ion batteries

Nowadays, the abundant use of the traditional energy resources, especially fossil fuels, brings many environmental and social problems. Renewable energy sources, such as solar radiation, wind and waves, are receiving increasingly wide attention and also bear the promise to become a huge new industry. The intermittent nature of renewable energy sources requires energy storage, preferably with a high conversion efficiency¹. Among energy storage techniques, batteries, especially Li-ion batteries, have enabled the development of small-scale portable electronic applications and have been viewed as the prime candidate for the next generation hybrid and electrical vehicles due to their high energy and power density.

The storage of electronic energy can be traced back to the 18th century. In 1745 Pieter van Musschenbroek first invented the so called 'Leyden jar' by using metal sheets and rods. The electricity was stored in the jar without the use of an electrolyte, making this a capacitor. The first electrochemical cell was designed by Alessandro Volta in 1800s and improved by John Daniell. This battery was made up by two electrodes, zinc and copper plates, separated by a sulphuric acid electrolyte, referred to as the Daniell cell. After that numerous primary (single used) batteries were invented.

The secondary battery, so called rechargeable battery, was invented by Gaston Planté in 1859² using the name 'Lead-acid battery'. After that more and more secondary batteries were reported including Nickel-Cadmium (Ni-Cd), Nickel Metal hydride (Ni-MH)³. In 1976 Whittingham reported, a reversible Li battery

using the electrochemical reaction between layered titanium disulfide and lithium metal that delivered a 2.0 V output potential at room temperature^{4,5}. However, the use of lithium metal is not considered safe because the formation of lithium dendrites that can potentially short circuit the battery, thus becoming responsible for safety hazards^{6,7}. The replacement of lithium metal by a lithium insertion compound as negative electrode successfully solved this problem. This type of battery is called the Li-ion, or rocking chair battery. Compared with other kinds of rechargeable batteries, Li-ion batteries have a higher output voltage responsible for the large energy density⁷, making Li-ion batteries the most promising candidates for hybrid electric vehicles (HEVs), electric vehicles (EVs).

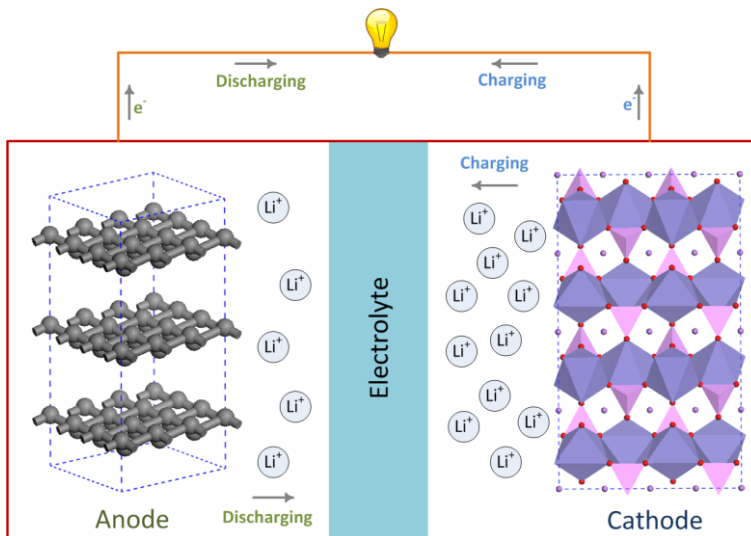


Figure 1.1 The schematic of Li-ion battery

A Li-ion battery consists of two electrodes, a cathode and an anode, which are separated by the electrolyte (see Figure. 1.1). The electrolyte allows Li-ions to migrate between the anode and the cathode and blocks electron transport. When the electrodes are connected externally, the chemical reactions proceed at both electrodes due to the difference in the chemical potential of Li in the two electrodes, thereby providing an electrical current through the external circuit.

The large demands of mobile electronic devices and mobile transport requires Li-ion batteries with high energy and power density. The gravimetric or volumetric energy density of a Li-ion battery is determined by the total amount of lithium ions that can be stored in the electrode materials, per unit mass or volume, respectively, and the output voltage. The power density is the specific amount of energy that can be stored in or released by a battery in a certain (dis)charge time. The cycle life of batteries depends both on the structural changes within the electrodes upon Li-ion insertion and extraction, and on the stability of the electrolyte towards the electrode potentials. The latter requires the electrochemical potentials of the two electrodes to fall within the stability window of the electrolyte.⁸ An anode with a potential above the lowest unoccupied molecular orbital (LUMO) will reduce the electrolyte unless a Solid Electrolyte Interface (SEI) develops that passivates further electron transfer from the negative electrode to the electrolyte LUMO. Similarly, when the cathode has a potential higher than the highest occupied molecular orbital (HOMO) the electrolyte will be oxidized⁸. In this way the irreversible formation of an SEI may provide a metastable situation, but on the long term it reduces the cycle life and has the additional disadvantage of an initial capacity loss required for the SEI development.

The power density, or the (dis)charge time of Li-ion batteries, is determined by the internal resistance of the system. Up to date it is unclear what microscopic process determines the internal resistance under what condition. Possible contributions to the internal resistance include (1) the electronic wiring, (the contact between the active electrode material and current collector), (2) the ionic network formed by the liquid electrolyte in the pores of the composite electrodes connecting the active electrode material and the electrolyte, (3) the charge transfer reaction between the liquid electrolyte and the active electrode material and (4) the solid state transport and phase nucleation/transformation kinetics within the active electrode material. In particular first-order phase transitions that occur upon Li-ion insertion and extraction appear to be decisive for the power density and cycle life of Li-ion batteries.

Therefore it is highly important to gain more understanding of the structural changes and charge transport during battery operation, enabling the improvement of future battery design and performance. This is the main objective of this thesis. In the following the electrode materials on the topic of this thesis research are introduced in detail.

1.2 Cathode materials

For Li-ion batteries, the energy and power density is largely determined by the positive electrode material. In 1980, Goodenough et al, for the first time, reported LiCoO_2 as a positive electrode material for Li-ion batteries with a high energy density⁹. Quickly, LiCoO_2 became the first commercial cathode material, realized by the Sony Company, for mobile energy storage devices, being applied even today¹⁰. However, the high cost and the large environmental foot print make this material not suitable for large-scale application in the renewable energy industry for applications, such as hybrid and electrical vehicles. This initiated the search for alternative positive electrode materials resulting in many options such as Spinel materials including $\text{LiNi}_x\text{Mn}_{2-x}\text{O}_4$ ^{11,12,13}, layered materials including $\text{LiNi}_x\text{Mn}_y\text{Co}_z\text{O}_2$ ¹⁴⁻¹⁶ and olivines including LiFePO_4 . In particular the latter is considered very promising, and nowadays it is already frequently applied due to its low cost, high cycling performance and safety characteristics.

1.2.1 Progress of fundamental LiFePO_4 research

LiFePO_4 was first introduced by Goodenough *et al.* in 1997¹⁷, it shows the ability to accommodate lithium ions reversibly by the first-order phase transition between FePO_4 and LiFePO_4 ¹⁷. Although it showed poor intrinsic electronic conductivity, particle size reduction in combination with adding a conductive phase have overcome this limitation¹⁸⁻²¹. These key innovations have greatly improved the rate performance of LiFePO_4 and made it the most promising candidate for high rate applications. Reaching an even better kinetic performance requires fundamental understanding of the lithium diffusion kinetics and the

phase transformation mechanism²². To develop a complete picture of the lithium intercalation kinetics within a LiFePO_4 electrode many efforts have been made during the last decade.

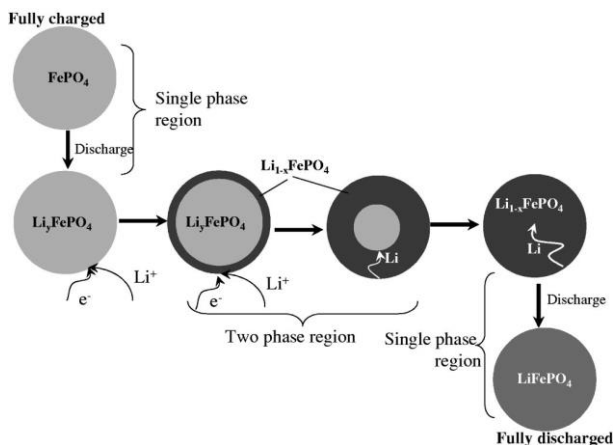


Figure 1.2 Illustration of the Shrinking-Core model by Srinivasan and Newman²³.

Andersson proposed a core-shell model to describe the phase transformation of LiFePO_4 during charging and discharging²⁴, which was further developed by Srinivasan and Newman²³. In the shrinking core model one phase is covered with a shell of the second phase. The reaction front for both lithiation and delithiation moves radially inward or outward. The transport of Li ions in the shell is the driving force for the phase boundary movement (see Figure.1.2)²³. This model was initially used to explain the current bottleneck that limits the capacity at high currents for LiFePO_4 materials²⁵. However, it appears both energetically and kinetically unfavorable as the 'core-shell' mechanism requires an isotropic diffusion through the crystalline lattice^{24,25}.

Using Density Functional Theory (DFT) Morgan et al. proposed lithium ions to diffuse through one-dimensional channels in LiFePO_4 . High-energy barriers separate the different channels²⁶. Their theoretical result was experimentally proven by Yamada *et al* using neutron diffraction in 2008²⁷, proving an anisotropic charge transfer which is in conflict with the core-shell model.

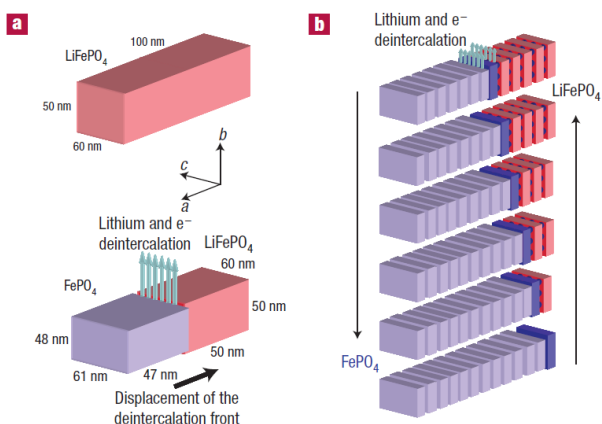


Figure 1.3 Schematic picture of the Domino Cascade model by Delmas et al.²⁸

In 2008 the group of Delmas proposed a new model for the phase transition in LiFePO_4 ²⁸. Using ex-situ X-ray diffraction they claimed that electrode particles were composed of only one end-member phase, either the Li-poor or the Li-rich phase during charging and discharging, suggesting a very fast transformation of the electrode particles. The diffusion along the [010] direction is very fast and would spread quickly along the [100] axis followed by the next [010] channel, just like a domino cascade model (see Figure. 1.3). Thereby proposed a layer-by-layer anisotropic phase transformation mechanism for single particle. The physical framework that describes the many-particle discrete transformations in a porous electrode was proposed by Dreyer^{29,30} et al. which called this the ‘mosaic instability’ or ‘mosaic transformation’ of the electrode material. This model successfully explained the hysteresis in insertion electrodes²⁹. Both the Shrinking-core²³ and domino-cascade models²⁸ have been proposed based on ex-situ characterization, and have not been tested during realistic non-equilibrium conditions that occur upon battery cycling.

The impact of defects, particle size, and charge rate on the phase transition in LiFePO_4 has been studied intensively. The existence of metastable states during the phase transition has been observed³¹⁻³³. Particle-size induced extended solid-solution compositions were first reported by Yamada et al³¹. The end-member

phases, lithium-rich triphylite $\text{Li}_{1-\beta}\text{FePO}_4$ (LFP) and lithium-poor heterosite $\text{Li}_\alpha\text{FePO}_4$ (FP), demonstrate narrow solid-solution domains in micron-size particles at room temperature³¹ and a solid-solution over the entire compositional range was observed above 520 K^{34,35}. Recently, the particle-size induced solid solutions were experimentally proven³⁶ and explained as the consequence of the diffuse interface^{36,37} and coherency strain³⁸. The actual phase transformation mechanism under in-situ (dis)charge (non-equilibrium) conditions appears to be more complicated, displaying concurrent solid solution and two-phase reaction structural evolution³⁹. Recent in-situ high-rate diffraction studies by Orikasa *et al.*^{32,33} revealed a metastable $\text{Li}_{x\sim 0.6}\text{FePO}_4$ phase, in addition to the thermodynamically stable LiFePO_4 and FePO_4 phases, rather than the predicted solid-solution transformation.^{38,40,41}

Theoretically, using a 1D phase field model Bai *et al.*⁴⁰ predicted a critical current for the suppression of the phase separation in single particles and the existence of an intermediate, quasi solid-solution transient state. This model was further developed, including coherency strain and 2D pattern formation, by Cogswell *et al.*³⁸ showing that the overpotential overwhelms the relatively small free energy gain from phase separation, which drives the formation of the quasi solid-solution state. Additionally, the suppression of phase separation by the overpotential was predicted by DFT simulations using the argument that bulk nucleation is energetically costly compared to the solid solution transformation⁴¹. Recent phase-field modelling⁴², including the impact of surface energies, predicted a limited role of nucleation in LiFePO_4 as the nucleation barrier becomes smaller, or even vanishing, when the particle size reduces originating from the complete wetting of surface facets.

1.3 Anode Materials

Compared to the many commercially available cathode materials, graphite remains the material of choice for the negative electrode⁴³ having a reversible capacity of approximately 350 mAh/g. Searching for alternatives with higher capacities, much attention has been devoted to Li alloys⁴⁴ as the breakthrough in

capacity can be achieved by moving from classical intercalation reactions to alloying reactions. Among the various Li alloy (Sn, Pb, Al, Au, Pt, Zn, Ag, Mg and others⁴⁵), Si has been considered as one of the most attractive anode materials for Li-ion batteries because of its high gravimetric (4200 mAhg^{-1}) and volumetric (2400 mAhcm^{-3}) capacity⁴⁶, as well as for its abundance, low costs and environmental benign properties. Aiming at an improved cycle life, a different approach may be to search for a negative electrode with a reduction potential just above the stability of common electrolytes, amounting approximately to 0.8 V vs Li/Li^+ for LiPF_6 in EC/DMC (1:1). Because graphite operates around 0.3 V vs Li/Li^+ , the disadvantage of a negative electrode potential working around 1 V would be the lower battery voltage, which compromises the energy density. The current options include mainly titanium oxides where, anatase⁴⁷, rutile⁴⁸, brookite⁴⁹ and spinel $\text{Li}_4\text{Ti}_5\text{O}_{12}$ ⁵⁰ all operate above 1.5V vs Li/Li^+ , with capacities around 150 mAh/g. The reduction of the Li insertion potential is the motivation within this thesis to study the Magnéli-phase Ti_4O_7 as a potential negative electrode having a potential close to 1 V.

1.4 Outline of this thesis: Scientific questions and the techniques involved

Despite the intensive research activity described, up to date fundamental debates remain on the phase transition mechanism of LiFePO_4 . This has led to the first two research questions of this thesis:

(1) How does the cycling rate affect the phase transition behaviour?

In Chapter 3, the impact of (dis)charge rate on the phase transition mechanism in LiFePO_4 electrodes is revealed by in-operando synchrotron X-ray diffraction. Diffraction allows one to determine the evolution of the phase composition, giving a complete and consistent picture of the equilibrium and non-equilibrium phase transformations in LiFePO_4 . At low (dis)charge rates the generally accepted mosaic transformation (characterized by a small fraction actively transforming LiFePO_4

grains that supply the overall current) is observed, whereas at high (dis)charge rates an increasing fraction of solid-solution phases is observed. This indicates that at high rates the electrode transforms through a solid solution reaction, rather than through the expected first order phase transition, consistent with recent phase field modelling. The results demonstrate that the phase transformation path in the Li_xFePO_4 system depends on the (dis)charge rate (overpotential) providing a rationale for the remarkable fast kinetics of LiFePO_4 . Because only a limited fraction of the electrode appears active, it is concluded that nucleation rates are not limiting the transformation rate and thereby these new findings indicate that improvement of electrode performance should focus on optimization the ionic/electronic transport in LiFePO_4 electrodes.

(2) What is the phase transition behaviour of single particles during lithium cycling?

Where powder diffraction, as applied in chapter 3, gives average phase information, reducing the X-ray beam to micrometer dimensions gives the opportunity to monitor the phase transition in individual grains. In chapter 4 this technique, micro-beam 2D diffraction was applied for the first time during in-operando cycling of a Li-ion battery electrode. At low (dis)charge rates nanometer thin plate-shaped domains nucleate, growing slowly and concurrently in specific crystallographic orientations proving phase coexistence in single grains, defying the long assumed mosaic or domino cascade transformation model. As the (dis)charge rate increases the number of these plate shaped domains decreases and their width increases, driving the local compositions of the coexisting phases towards each other. The unique direct observation of a diffuse interface in a single grain at high (dis)charge rates reveals the growth mechanism at high rates, consistent with the in-operando powder diffraction in Chapter 3. Measuring the transformation process of individual LiFePO_4 particles allows for the first time quantification of local current densities in Li-ion battery electrodes under realistic (dis)charge conditions. The results suggest the (dis)charge rate is dependent on the local current density, which was derived from the average transformation times of individual grains. The 2DXRD technique opens new opportunities for the

characterization and understanding of phase transitions taking place in battery electrodes.

The phase transition behaviour in individual LiFePO_4 grains represent only one aspect of the charge transport that takes place in Li-ion battery electrodes. Electrodes exist of millions of LiFePO_4 grains, which build up a porous matrix in combination with a binder and an electronic conducting additive (i.e. Carbon Black). During operation this solid matrix should allow electronic transport compensating the Li-ion transport. The latter takes place throughout the electrolyte in the pores of the electrode and in the solid state. Whether the electronic or Li-ion transport through these heterogeneous porous electrode systems is rate limiting, is a crucial question for battery improvement. This initiated the third scientific question of this thesis:

(3) How does the Li-ion transport behave under realistic charge/discharge conditions

Throughout the literature it is very hard to distinguish a consensus on what charge transport process in Li-ion battery electrodes determines the internal resistance, and thereby governs the (dis)charge times, under varying conditions. This is in the first place related to the difficulty to probe the Li-ion transport directly under realistic in-operando conditions.

Using the ability of Neutron Depth Profiling (NDP) to probe the Li-ion concentration as a function of electrode depth is exploited in chapter 5. In-Operando NDP is performed for the first time on conventional Li-ion batteries, providing a direct observation of the evolution of Li-ion concentration gradient in LiFePO_4 electrodes at different electrochemical conditions for different types of electrodes. The results give unique direct insight, unavailable up to date, revealing what charge transport mechanism dominates at what condition. It is demonstrated that the rate limiting charge transport mechanism, determining the internal resistance and overpotential of Li-ion batteries, depends both on the electrode composition and, more surprisingly, on the actual (dis)charge rate. At

low (dis)charge rates LiFePO_4 nucleation barriers appear rate limiting, proving lower nucleation barriers for smaller particles. At intermediate rates depletion at the current collector side of the electrode indicates that the ohmic electronic resistance in the electrode is rate limiting, an unexpected result with important implications. In contrast, at high (dis)charge rates the observed Li-ion concentration gradients indicate that ionic diffusion throughout the porous electrode matrix is rate limiting. These results indicate that depending on the applied (dis)charge rate a different route should be chosen to lower the internal resistance, and hence improve rate capacities and overall efficiency.

Finally, in this thesis an alternative negative electrode material was considered aiming at a working potential inside the stability window of typical commercial electrolytes. This leads to the following question:

(4) Is the Magnéli-phase Ti_4O_7 material, working around 1.0 V vs Li/Li^+ a possible negative electrode material suitable for Li-ion batteries?

In Chapter 6, theoretical and experimental studies were performed on the Magnéli-phase Ti_4O_7 system as a potential negative electrode material for Li-ion batteries. Based on the first principle calculations, using the DFT generalized gradient approximation (GGA), we investigated the structure of Ti_4O_7 as well as $\text{Li}_2\text{Ti}_4\text{O}_7$. Our calculation resulted in an average voltage of 0.92 V which is at the lower stability window of commonly used electrolytes (such as LiPF_6 EC/DMC), suggesting a higher stability and longer cycle life compared to negative electrodes working at lower potentials. Galvanostatic charging and discharging results in an average voltage of about 1.0 V. For 278 nm particles only a reversible capacity of 90 mAh/g is found. However, ballmilling and carbon coating improves this to 140 mAh/g for 50 cycles.

References

- (1) Mulder, F. M. *J. Renewable Sustainable Energy* **2014**, *6*, 033105.
- (2) Schöllhorn, R.; Kuhlmann, R.; Besenhard, J. O. *Materials Research Bulletin* **1976**, *11*, 83.
- (3) D., L.; B., R. T. *Hand book of battery* 3rd ed.; The McGraw-Hill Companies, Inc., 2002.
- (4) Murphy, D. W.; Cava, R. J.; Zahurak, S. M.; Santoro, A. *Solid State Ionics* **1983**, *9-10*, 413.
- (5) Whittingham M. S. *Science* **1976**, *192*, 1126.
- (6) Yoshimatsu, I.; Hirai, T.; Yamaki, J. *J. Electrochem. Soc.* **1988**, *135*, 2422.
- (7) Tarascon, J. M.; Armand, M. *Nature* **2001**, *414*, 359.
- (8) Tarascon, J. M.; Recham, N.; Armand, M.; Chotard, J.-N.; Barpanda, P.; Walker, W.; Dupont, L. *Chem. Mater.* **2009**, *22*, 724.
- (9) Mizushima, K.; Jones, P. C.; Wiseman, J. B.; Goodenough, J. B. *Materials Research Bulletin* **1980**, *15*, 783.
- (10) Nagaura, T.; Tazawa, K. *Prog. Batteries Solar Cells* **1990**, *9*, 20.
- (11) Thackeray, M. M.; David, W. I. F.; Bruce, P. G.; Goodenough, J. B. *Materials Research Bulletin* **1983**, *18*, 461.
- (12) Thackeray, M. M. *Progress in Solid State Chemistry* **1997**, *25*, 1.
- (13) Amine, K.; Tukamoto, H.; Yasuda, H. F., Y. *J. Electrochem. Soc.* **1996**, *143*, 1607.
- (14) Weaving, J. S.; Coowar, F.; Teagle, D. A.; Cullen, J.; Dass, V.; Bindin, P.; Green, R.; Macklin, W. J. *J. Power Sources* **2001**, *97-97*, 733.
- (15) Lee, K. K.; Yoon, W. S.; Kim, K. B.; Lee, K. Y.; Hong, S. T. *J. Power Sources* **2001**, *97-98*, 308.
- (16) Yabuuchi, N.; Ohzuku, T. *J. Power Sources* **2003**, *119*, 171.
- (17) Padhi, A. K.; Nanjundaswamy, K. S.; Goodenough, J. B. *J. Electrochem. Soc.* **1997**, *144*, 1188.
- (180) Huang, H.; Yin, S. C.; Nazar, L. F. *Electrochem. Solid State Lett.* **2001**, *4*, A170.
- (19) Herle, P. S.; Ellis, B.; Coombs, N.; Nazar, L. F. *Nat. Mater.* **2004**, *3*, 147.

- (20) Gaberscek, M.; Dominko, R.; Jamnik, J. *Electrochem. Commun.* **2007**, *9*, 2778.
- (21) Wang, Y.; Wang, Y.; Hosono, E.; Wang, K.; Zhou, H. *Angew. Chem., Int. Ed.* **2008**, *47*, 7461.
- (22) Wang, J.; Sun, X. *Energy and Environmental Science* **2015**, *8*, 1110.
- (23) Srinivasan, V.; Newman, J. J. *Electrochem. Soc.* **2004**, *151*, A1517.
- (24) Andersson, A. S.; Thomas, J. O. *J. Power Source* **2001**, *97-98*, 498.
- (25) Malik, R.; Abdellahi, A.; Ceder, G. J. *Electrochem. Soc.* **2013**, *160*, A3179.
- (26) Morgan, D.; Van der Ven, A.; Ceder, G. *Electrochem. Solid State Lett.* **2004**, *7*, A30.
- (27) Nishimura, S.; Kobayashi, G.; Ohoyama, K.; Kanno, R.; Yashima, M.; Yamada, A. *Nat. Mater.* **2008**, *7*, 707.
- (28) Delmas, C.; Maccario, M.; Croguennec, L.; Le Cras, F.; Weill, F. *Nat. Mater.* **2008**, *7*, 665.
- (29) Dreyer, W.; Jamnik, J.; Gohlke, C.; Huth, R.; Moskon, J.; Gaberscek, M. *Nat. Mater.* **2010**, *9*, 448.
- (30) Dreyer, W.; Gohlke, C.; Huth, R. *Physica D* **2011**, *240*, 1008.
- (31) Yamada, A.; Koizumi, H.; Nishimura, S. I.; Sonoyama, N.; Kanno, R.; Yonemura, M.; Nakamura, T.; Kobayashi, Y. *Nat. Mater.* **2006**, *5*, 357.
- (32) Orikasa, Y.; Maeda, T.; Koyama, Y.; Murayama, H.; Fukuda, K.; Tanida, H.; Arai, H. *J. Am. Chem. Soc.* **2013**, *135*, 5497.
- (33) Orikasa, Y.; Maeda, T.; Koyama, Y.; Murayama, H.; Fukuda, K.; Tanida, H.; Arai, H. *Chem. Mater.* **2013**, *25*, 1032.
- (34) Delacourt, C.; Poizot, P.; Tarascon, J. M.; Masquelier, C. *Nat. Mater.* **2005**, *4*, 254.
- (35) Stevens, R.; Dodd, J. L.; Kresch, M. G.; Yazami, R.; Fultz, B. *J. Phys. Chem. B* **2006**, *110*, 22732.
- (36) Wagemaker, M.; Singh, D.; Borghols, W.; Lafont, U.; Haverkate, L.; Peterson, V.; Mulder, F. J. *J. Am. Chem. Soc.* **2011**, *133*, 10222.
- (37) Burch, D.; Bazant, M. Z. *Nano Lett.* **2009**, *9*, 3795.
- (38) Cogswell, D. A.; Bazant, M. Z. *ACS Nano* **2012**, *6*, 2215.

- (39) Sharma, N.; Guo, X.; Du, G.; Guo, Z.; Wang, J.; Wang, Z.; Peterson, V. J, *Am. Chem. Soc.* **2012**, *134*, 7867.
- (40) P., B.; Cogswell, D. A.; Bazant, M. Z. *Nano Lett.* **2011**, *11*, 4890.
- (41) Mialik, R.; Zhou, F.; Ceder, G. *Nat. Mater.* **2012**, *10*, 587.
- (42) Cogswell, D. A.; Bazant, M. Z. *Nano Lett.* **2013**, *13*, 3036.
- (43) Shodai, T.; Okada, S.; Yamabi, S. *Solid State Ionics* **1996**, *86-88*, 785.
- (44) Winter, M.; Besenhard, J. *Electrochem. Acta* **1999**, *45*, 31.
- (45) Dey, A. N. *J. Electrochem. Soc.* **1971**, *118*, 1547.
- (46) Park, C. M.; Kim, J. H.; H., K.; Sohn, H. J. *Chem. Soc. Rev.* **2010**, *39*, 3115.
- (47) Olson, C. L.; Nelson, J.; Islam, M. S. *J. Phys. Chem. B* **2006**, *110*, 9995.
- (48) Ohzuku, T.; Takehara, Z.; Yoshizawa, S. *Acta* **1979** *24*, 219.
- (49) Reddy, M. A.; Kishore, M. S.; Pralong, V.; Varadaraju, U. V.; Raveau, B. *Solid-State Lett.* **2007**, *10*, A29.
- (50) Ferg, E.; Gummow, R. J.; Dekock, A.; Thackeray, M. M. *J. Electrochem. Soc.* **1994**, *141*, L147.

Chapter 2

Experimental Techniques

In this chapter, the two main experimental techniques that were used in this thesis are described. In-operando X-Ray micro-beam 2D synchrotron diffraction (2D-XRD) was applied to study the phase transformation in individual LiFePO_4 grains. In-operando and ex-situ Neutron Depth Profiling (NDP) was used to directly probe the evolution of the Li concentration during battery cycling.

2.1 2D-XRD diffraction

2.1.1 Experiment set up

The two dimensional X-ray diffraction experiments described in this thesis were performed at beamline ID11 of the European Synchrotron Radiation Facility (ESRF) in Grenoble, France. The experiment setup is shown in figure 2.1. Monochromatic X-rays with the energy of 40 keV (wavelength of 0.30996 Å) were used to illuminate the coffee bag cells. For powder diffraction experiments the beam size was $50 \times 50 \mu\text{m}^2$ whereas for the single-grain experiments the beam size is $1.7 \times 1.7 \mu\text{m}^2$ in order to detect separate reflections in the electrodes. The grains that fulfilled the Bragg condition generated a diffraction spot on the 2D CCD detector placed behind the sample. During exposure the sample was continuously rotated around the axis perpendicular to the X-ray beam in steps of $\Delta\omega = 0.5^\circ$ with an exposure time of 10 s (C/5, C/2), 5 s (2C). By collecting several subsequent angular exposures a total angular range of 6° (2C, C/50) or 12° (C/2, C/5) was covered, resulting in a time resolution for individual measurements cycles of 1 min

(2C), 4 min (C/2, C/5) and 2 min (C/50). The instrumental parameters were determined using a CeO_2 as calibration material.

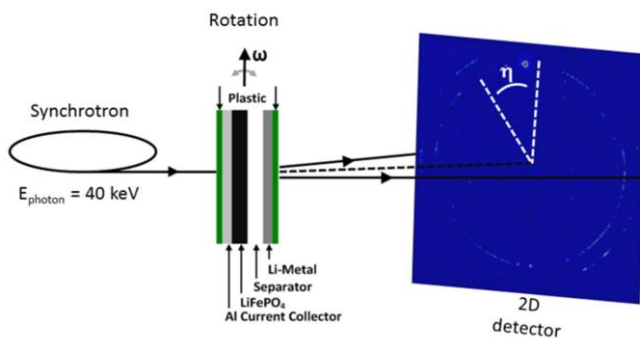


Figure 2.1 Schematic representation of the in-situ synchrotron X-Ray diffraction set up. During exposure the sample was continuously rotated over a small angle around the vertical axis

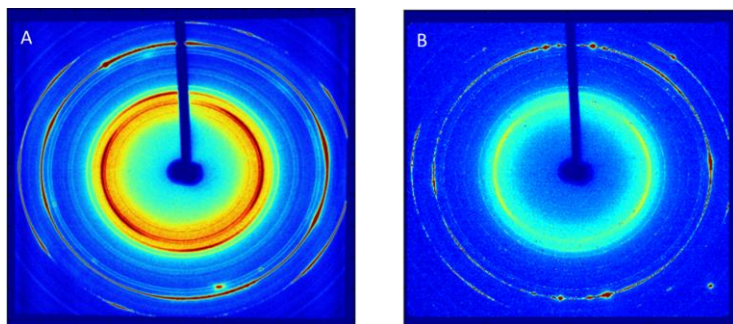


Figure 2.2 Two dimensional X-ray diffraction pattern for (a) powder diffraction with a beam size of $50 \times 50 \mu\text{m}^2$, and (b) micro-beam diffraction with beam size of $1.7 \times 1.7 \mu\text{m}^2$.

For the powder diffraction full diffraction rings are observed due to a large number of grains that obey the Bragg conditions, as shown in Figure 2.2. However, for the single-grain experiments, separated diffraction spots could be distinguished as the smaller beam size only leads to a small amount of grains obeying Bragg's law, as shown in Figure 2.2.

2.1.2 Theory of 2D-XRD diffraction microscopy

The diffracted intensity I_g of a diffraction spot is related to the volume of the grain V_g and can be written in the kinematic approximation as^{1,2}

$$I_g = \Phi_0 r_0^2 \frac{\lambda^3 |F_{hkl}|^2 V_g}{\Delta\omega |\sin\eta| V^2} L_g P T_r \exp(-2M) \quad (2-1)$$

where Φ_0 is the incident flux of photons, F_{hkl} is the structure factor of the $\{hkl\}$ reflection, λ is the photon wavelength, $\Delta\omega$ is the angular range over which the grain is rotated, V is the volume of the unit cell, P is the polarization factor and T_r is the transmission factor. The Lorentz factor of the grain is given by $L_g = 1/\sin(2\theta)$, where 2θ is the scattering angle. The angles η and ω are the azimuthal angle and the sample rotation angle, respectively (see Fig 2.1). The Thomson scattering length r_0 is given by

$$r_0 = \frac{e^2}{4\pi\epsilon_0 m_e c^2} = 2.82 \times 10^{-15} \text{ m} \quad (2-2)$$

where $e = 1.602 \times 10^{-19}$ C is the electron charge, $m_e = 9.1094 \times 10^{-31}$ kg is the electron mass, $c = 2.9979 \times 10^8$ m/s is the velocity of light, and $\epsilon_0 = 8.85419 \times 10^{-12}$ F/m is the permittivity of vacuum. The Debye-Waller factor $\exp(-2M)$ accounts for the thermal vibrations of the atoms⁴ with

$$M = \frac{6h^2 T}{mk_B \Theta^2} \left[\phi(x) + \frac{x}{4} \left(\frac{\sin\theta}{\lambda} \right)^2 \right] \quad (2-3)$$

where $h = 6.62608 \times 10^{-34}$ Js is the Planck constant, m is the mass of the vibrating atom, $k_B = 1.381 \times 10^{-23}$ J/K is the Boltzmann constant, Θ is the Debye temperature, $x = \Theta/T$ is the relative temperature, T is the temperature, and ϕ is given by:

$$\phi(x) = \frac{1}{x} \int_0^x \frac{\zeta}{\exp(\zeta) - 1} d\zeta \quad (2-4)$$

For powder diffraction the integrated intensity I_p of a $\{hkl\}$ -diffraction ring of a polycrystalline material with randomly oriented grains is given by

$$I_p = \Phi_0 r_0^2 \frac{m_{hkl} \lambda^3 |F_{hkl}|^2 V(t)}{V^2} L_p P \exp(-2M) \quad (2-5)$$

where m_{hkl} is the multiplicity factor of the $\{hkl\}$ -ring and V is the volume of the diffracted phase. The Lorentz factor for a powder is given by $L_p = 1/(4\sin(\theta))$. The volume of the diffracted phase is given by

$$V = f_i V_{gauge} \quad (2-6)$$

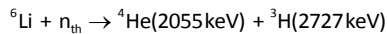
where f_i is the volume fraction of the diffracted phase and V_{gauge} is the gauge volume, which is defined by the beam size and the thickness of the sample. The volume of an individual grain is calculated from the integrated Bragg peak intensity of a grain I_g normalized by the powder intensity of the $\{hkl\}$ -ring in which the reflection from the individual grain appeared by

$$V_g = \frac{1}{2} m_{hkl} \Delta\omega |\sin \eta| \cos(\theta) f_i V_{gauge} \frac{I_g}{I_p} \quad (2-7)$$

2.2 Neutron Depth Profiling (NDP)

2.2.1 Introduction

The Neutron Depth Profiling (NDP) technique is based on neutron capture reactions. Specific isotopes of elements have a significant cross section for a capture reaction generating either a proton or an alpha particle and a residual nucleus that carries the remainder of the nucleons. The energy that is generated by the capture reaction will distribute between the proton (or the alpha particle) and recoiling nucleus according to the laws of conservation of energy and momentum. For the ${}^6\text{Li}$ isotope this reaction is:



When the incoming thermal neutrons are captured by the ${}^6\text{Li}$ (natural abundance $\sim 7.5\%$) it will generate ${}^3\text{H}$ and ${}^4\text{He}$ particles with a specific kinetic starting energy. Both particles will dissipate part of their kinetic energy due to the scattering. The interaction with the material leads to a specific stopping power that can be

determined based on the chemical composition with for instance SRIM⁵. Since the batteries were placed under vacuum the ^4He and ^3H particles will lose negligible energy after leaving the battery towards the detector. By measuring the energy of the particles when reaching the detector, the depth at which the capture reaction took place, i.e. the location of the Li-ion, can be determined. The loss in Li concentration due to the capture reactions is negligible because the incoming thermal neutron flux is very small compared to the amount of Li ions available. This makes NDP a non-destructive technique.

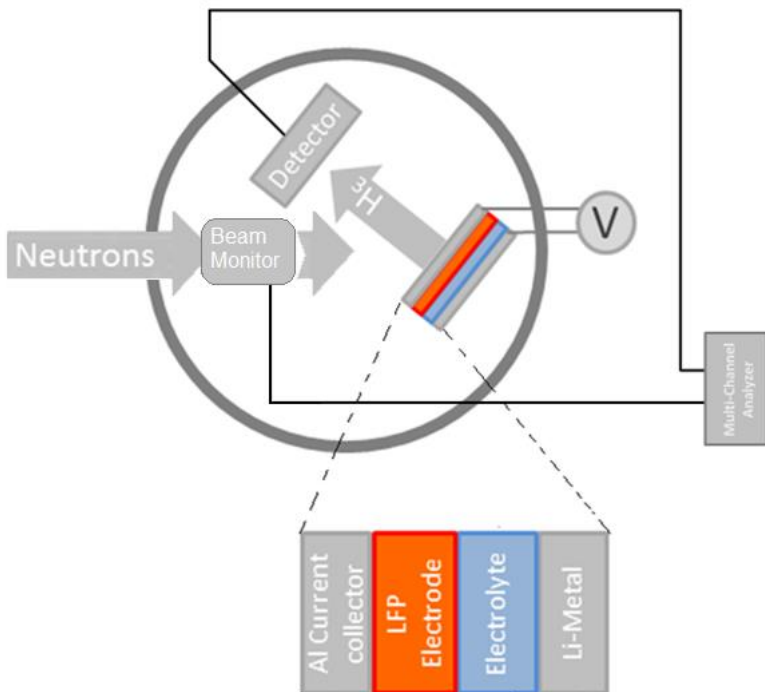


Figure 2.3 The Schematic NDP setup at the Reactor Institute Delft.

The NDP set-up and principle of the in-situ NDP is schematically shown in Figure.2.3 The NDP cell is positioned inside a vacuum chamber at an angle of 30 degrees towards the incident neutron beam facing to the detector. The energy of

the ^4He and ^3H particles leaving the in-situ battery are measured using a charged particle implanted Si detector. The energy spectrum is then collected by a Multi Channel Analyzer (MCA).

2.2.2 NDP data analysis

To analyse the NDP data we have to relate the energy to the depth in the electrode, and perform background and intensity corrections.

SRIM can be used to estimate the thickness of the probed sample via the stopping power tables. In addition, it allows one to construct the depth calibration. A LiFePO_4 electrode coating on approximately $10\ \mu\text{m}$ Al foil is shown below as an example of the obtained NDP data.

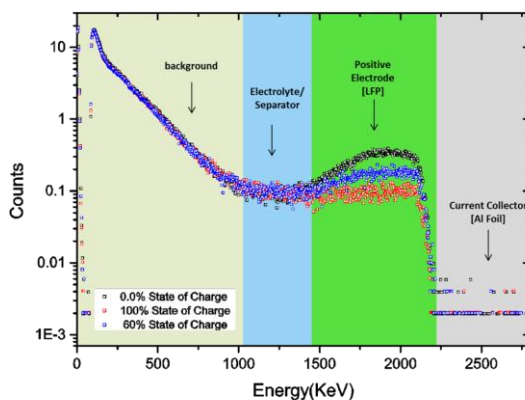


Figure 2.4 In-situ NDP spectra at different states of charge of an approximately $16\ \mu\text{m}$ thick LiFePO_4 electrode coated on Al foil.

2.2.2.1 Thickness estimation of the Al foil

The thickness of the Al foil can be estimated as follows. In Figure 2.4 the highest energy of triton ions escaping from the electrode have an energy of approximately 2140 keV, which means that these triton ions lose approximately 587 keV. Already

the stopping power for the ^4He particles in the Al layer is large enough to lose all their initial kinetic energy, and therefore ^4He particles are not measured in the experiments presented in this thesis. In the SRIM table for ^3H of Al stopping power at 2750 keV is 49 keV/ μm . Therefore the aluminium foil thickness is approximately 12.0 μm .

2.2.2.2 Depth calibration and stopping power calculation

When a neutron capture reaction occurs at a certain distance from the surface of the sample, the generated charged particles, that move in the direction of the detector, will lose part of their energy in the sample. To correlate the measured energy with the distance that the triton ion travelled through the sample, a calibration curve needs to be constructed based on the stopping power of the material. For the experiment in Figure 2.4 the LiFePO_4 density is approximately 2 g/cm^3 . With SRIM⁵ the residual energy of a triton ion after passing through different thicknesses of the LiFePO_4 electrode and the Al foil are calculated (from 0 μm to approximately 35 μm with regular steps). A third-order polynomial function is used to fit the residual energy versus the LiFePO_4 layer thickness to obtain in a calibration relation between the energy of the triton ions and the depth of the capture reaction in the electrode, for this example it leads to:

$$d(E) = 45.94 - 0.00828 \times E - 3.608 \cdot 10^{-6} \times E^2 - 3.276 \cdot 10^{-11} \times E^3 \quad (2-8)$$

The stopping power of the material is equal to the loss of energy per unit path length. It is defined as the retarding force acting on charged particles due to interaction with matter⁶, which can be determined from the depth calibration values by taking the difference in energy (keV) divided by the difference (μm) in depth. After fitting these values with a third order polynomial the stopping power dependence on the energy is determined. In our experiment, the stopping power of LFP (2 g/cm^3) on top of 10.5 μm Al results in formula (2-9)

$$S(E) = 119.94 - 0.0886 \times E + 3.824 \cdot 10^{-5} \times E^2 - 6.531 \cdot 10^{-9} \times E^3 \quad (2-9)$$

2.2.2.3 Intensity correction

In all NDP measurements a background is present, which decreases approximately exponentially with increasing energy. This is mainly caused by the activation of the bulk sample material by the neutron beam. The background can be subtracted by either fitting an appropriate function such as e^{-ax^2-bx-c} to the data points, or by actually measuring it. For example, in the case of battery electrodes the delithiated state of the testing electrode in the same experiment setting can be used to subtract as the background.

Since a ${}^6\text{Li}$ standard for calibrating the intensities is not available, the Li concentration calibration was obtained with a boron concentration standard⁷. This can be performed as follows: A ${}^{10}\text{B}$ containing sample with a known concentration was measured in exactly the same geometrical setting in the in-situ electrochemical cell. In this way calibration factor is determined a converting from cnts/s to atoms/cm²:

$$C = \frac{n_{10B}[\text{atoms} / \text{cm}^2] \sigma_{10B}[\text{barn}]}{c_{10B}[\text{cnts} / \text{s}]} \quad (2-10)$$

Where n_{10B} and σ_{10B} refers to the atom density and the neutron cross section respectively. Normally C is of the order of 1.22×10^{19} ($n_{10B} = 9.543 \times 10^{15}$ atoms/cm², $\sigma_{10B} = 3837$ barn, $c_{10B} = 3$ cnts/s). This allows one to determine n_{Li} [Li/cm²] in the electrodes given the cross section for the capture reactions of ${}^{10}\text{B}$ ($\sigma_{10B} = 3837$ barn) and ${}^6\text{Li}$ ($\sigma_{6Li} = 940$ barn) and the natural abundance of ${}^6\text{Li}$ ($A_{6Li} = 0.075$):

$$n_{Li}[\text{Li} / \text{cm}^2] = \frac{n_{10B}[\text{atoms} / \text{cm}^2] \times \sigma_{10B}[\text{barn}]}{A_{6Li} \times c_{10B}[\text{cnts} / \text{s}] \times \sigma_{6Li}[\text{barn}]} \times c_{6Li}[\text{cnts} / \text{s}] \quad (2-11)$$

To convert this into the Li-ion density [Li/cm³] it is necessary to correct for the energy dependent stopping power, which in combination with the constant energy resolution of the detector (3.3 keV), results in a depth dependent resolution:

$$t(E)[\mu\text{m}] = \frac{3.3[\text{keV}]}{S(E)[\text{keV} / \mu\text{m}]} \quad (2-12)$$

References

- (1) Als-Nielsen, J.; McMorrow, D. *Elements of Modern X-ray Physics*; Wiley: West Sussex, 2001.
- (2) Warren, B. E. *X-ray Diffraction*; Dover Publications: New York, 1990.
- (3) Kavan, L.; Rathousky, J.; Gratzel, M.; Shklover, V.; Zukal, A. *J. Phys. Chem. B* **2000**, *104*, 12012.
- (4) Cullity, B. D.; Stock, S. R. *Elements of X-ray Diffraction*; Prentice-Hall: New Jersey, 2001.
- (5) Ziegler, J. F.; Ziegler, M. D.; Biersack, J. P. *Nucl. Instrum. Methods B* **2010**, *268*, 1818.
- (6) Bimbot, R.; Geissel, H.; Paul, H.; Schinner, A.; Sigmund, P. *Stopping of Ions heavier than Helium*, Journal of the ICRU Oxford Univ Press, 2005.
- (7) Liu, X.; Wang, J.; Pan, K.; Qiu, J.; Canova, M.; Cao, L.; Co, A. C. *Angew.* **2014**, *53*, 9498.

Chapter 3

Rate induced solubility and suppression of the first-order phase transition in olivine LiFePO_4

Based on the paper : '*Rate induced solubility and suppression of the first-order phase transition in olivine LiFePO_4* '

Xiaoyu Zhang, Martijn van Hulzen, Deepak P. Singh, Alex Brownrigg, Jonathan P. Wright, Niels H. van Dijk and Marnix Wagemaker*, *Nano Letters*, 14, 2279-2285

Abstract

The impact of ultra-high (dis)charge rates on the phase transition mechanism in LiFePO_4 Li-ion electrodes is revealed by in-situ synchrotron diffraction. At high rates the solubility limits in both phases increase dramatically causing a fraction of the electrode to bypass the first-order phase transition. Nucleation rates are consequently not limiting the transformation rate and thereby these new findings reveal that improvement of electrode performance should focus on optimization the ionic/electronic transport in LiFePO_4 electrodes.

3.1 Introduction

Chemical energy storage in Li-ion batteries is key technology for the future renewable society. Their energy and power density is largely determined by cathode materials that are able to host lithium in their crystal structure. State of the art LiFePO₄¹ stores lithium by the reversible first order phase transition between FePO₄ and LiFePO₄. The practical interest for this material is based on its stability, low costs and excellent battery performance after the initial hurdle of poor intrinsic electronic conduction was overcome using small particles in combination with conductive phases.²⁻⁶ Electrode phase transitions are of large practical importance in Li-ion batteries determining the voltage profile and as a decisive factor in the transition kinetics. The impact of defects, particle size, and charge rate on the phase transition in LiFePO₄, has been studied intensively⁷⁻²⁰. The end-member phases, lithium-rich triphylite Li_{1-β}FePO₄ (LFP) and lithium-poor heterosite Li_αFePO₄ (FP), demonstrate narrow solid-solution domains in micron-size particles at room temperature⁸ and a solid-solution over the entire compositional range above 520 K^{21,22}. Particle-size induced extended solid-solution compositions were first reported by Yamada et al.⁸ A systematic decrease of the miscibility gap with decreasing particle size was suggested based on Vegard's law¹⁰ and isolated solid-solution phases⁹. The latter recently experimentally proven¹¹ and explained as the consequence of the diffuse interface^{11,23} and coherency strain¹³. Interestingly, these size dependent phenomena appear to be a general phenomenon for two-phase intercalation systems as indicated by results on Li_xTiO₂ and MgH_x systems²⁴⁻²⁶. The actual phase transformation mechanism under in-situ (dis)charge (non-equilibrium) conditions appears to be more complicated displaying concurrent solid solution and two-phase reaction structural evolution.²⁷ Dreyer et al. proposed a mosaic transformation of the LiFePO₄ particles^{28,29}, consistent with ex-situ observations^{15,30,31}, explaining hysteresis in insertion electrodes²⁸ and the memory effect³². In contrast, chemically lithiated materials instead result in the existence

of interfaces between the coexisting phases within each particle^{11,20,33}. Using a simple statistical model of the mosaic transformation based on three populations of empty, transforming and full particles Bai et al.³⁴ were able to predict the experimentally observed transient current responds³⁵ further establishing the mosaic transition in LiFePO₄ under in-situ conditions. Using a 1D phase field model Bai et al.¹² predicted a critical current for the suppression of phase separation in single particles and the existence of an intermediate, quasi solid solution transient state. This model was further developed including coherency strain and 2D pattern formation by Cogswell et al.¹³ showing that the overpotential overwhelms the relatively small free energy gain from phase separation which drives the formation of the quasi solid solution state. Also DFT simulations predicted the suppression of phase separation by overpotentials using the argument that bulk nucleation is energetically costly compared to the solid solution transformation¹⁴. Recent phase field modelling¹⁸, including the impact of surface energies, predicted a limited role of nucleation in LiFePO₄ as the nucleation barrier becomes smaller, or even vanishing, when the particle size reduces originating from the complete wetting of surface facets. These findings give a rationale for the intrinsically fast kinetics of the LiFePO₄ material when the rate limitations of the full electrodes are lifted by effective electronic and ionic wiring^{6,36-40}. Although, up to date modelling gives largely a consistent picture⁴¹, direct experimental insight in the phase transition mechanism at high (dis)charge rates is largely unavailable. Recent in-situ high-rate diffraction studies by Orikasa et al.^{16,42} revealed a metastable Li_{x~0.6}FePO₄ phase in addition to the thermodynamically stable LiFePO₄ and FePO₄ phases rather than the predicted solid-solution transformation¹²⁻¹⁴. The metastable Li_{x~0.6}FePO₄ was suggested to reduce the strain of the coexisting end-members^{9,23} giving a different picture compared to phase field^{12,13,18} and DFT¹⁴ calculations.

3.2 Experiment Method

Sample preparation. The starting material was carbon coated LiFePO₄ from Phostech with an average particle size of 140 nm. Regular LiFePO₄ cathodes were prepared through mixing a slurry of LiFePO₄, Carbon Black (Super P), PVDF, (polyvinylidene fluoride, Solvay) in NMP (N-methylpyrrolidone, with a mass ratio of the active material (LiFePO₄), carbon black (SuperP) and binder (PVDF) of 80:10:10. In addition carbonate template electrodes were prepared to reach high capacities at high rates as reported recently³⁶. For the electrodes, 40 wt% NaHCO₃ (Aldrich) is added to the electrode slurry mixing, a large part which is lost by dissolution in the solvent. The final slurry was casted on carbon coated Aluminium current collectors by doctor blading. The coatings were dried on a heater plate under air at approximately 155 °C overnight followed by drying under vacuum at around 60 °C for more than 24 hours. The resulting coatings were pressed using a roller hand press to enhance the electronic contact. After mechanical compaction the NaHCO₃ templated electrodes were washed in demineralized water that reacts with the NaHCO₃ to form NaOH and gaseous CO₂, resulting in an electrode where the interconnectivity of the porosity in the electrodes is improved as demonstrated previously³⁶. Finally, the electrodes are dried for at least 3 hours under vacuum at 100 °C. The results are reported on electrodes with loading density between 2 and 4 mg/cm² and thickness approximately 10-20 μm.

Battery preparing and testing. The electrode were assembled in 'coffee-bag' type cells built following the plastic Li-ion cell procedure. All the samples were assembled under argon atmosphere (<0.1 ppm O₂/H₂O). The electrodes were separated by glass microfiber filters (Whatman) with a few droplets of 1 mol/liter LiPF₆ (EC:DMC 1:1, Novolyte) electrolyte. All the electrochemical tests were performed galvanostatically within a voltage window of 4.3 and 2.5 V vs Li/Li⁺ using an Autolab PGSTAT302N potentiostat/galvanostat.

In situ synchrotron X-ray diffraction. The in situ XRD measurements were performed at the ID11 beam line of the ESRF (France), using a monochromatic X-ray beam with $\lambda = 0.30996 \text{ \AA}$ ($E=40 \text{ keV}$), a beam size of $50 \text{ }\mu\text{m}$ and a FReLoN2k CCD detector. During exposure the sample was continuously rotated around the axis perpendicular to the X-ray beam over an angular range of 1° with an exposure time of 10 s (C/5, 5C), 5 s (10C) and 1 s (60C). The sloping background in the diffraction patterns is due to small angle and incoherent scattering of the plastic of the pouch cells and the electrolyte and separator.

3.3 Results and Discussion

To determine the phase transition mechanism dependence on the (dis)charge rate we performed an in-situ synchrotron diffraction study with (dis)charge rates ranging from a very low rate of C/5 up to ultra-high rates of 60C, where C/n denotes the rate at which a full charge or discharge takes n hours. In Figure 3.1a the rate-dependent charge and subsequent discharge voltage profiles demonstrate the anticipated decreasing capacities and growing overpotentials upon increasing rates. The performance of these electrodes prepared with a recently developed templating method³⁸ is excellent as reflected by the $\sim 70\%$ capacity retention upon 60C charge. Note that the smaller discharge capacity is the consequence of the antecedent 60C charging leaving 30% already in the discharged state. The in-situ diffraction shows a marked difference in the evolution of the $\{200\}^{13,18}$ reflection between C/5 and 60C charging as demonstrated in Figures 3.1b-c.

At C/5 the $\{200\}$ reflection of the Li-rich phase gradually diminishes as the $\{200\}$ reflection of the Li-poor phase grows, consistent with the established first-order phase transition that occurs upon delithiating LiFePO_4 . During this phase transition the initial LFP phase is converted into the FP phase both having the orthorhombic $Pnma$ space group. This is associated with a reduction in the a -lattice parameter, which is responsible for the shift of the $\{200\}$ reflection towards higher diffraction angles. A surprising observation during 60C charging is the gradual shift of the $\{200\}$ from the Li- rich phase position towards the Li-poor position showing

considerable intensity between the two reflections, which is absent at C/5 charging.

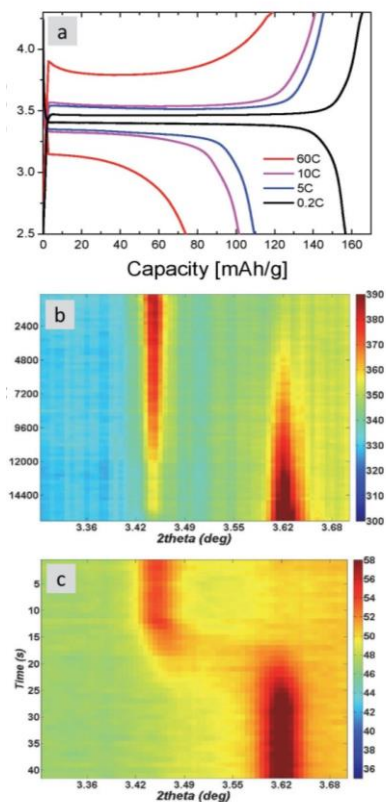


Figure 3.1. (a) Rate dependent electrochemistry of the in-situ LiFePO_4 electrodes showing one charge and subsequent discharge after slow initial cycling. C/n denotes the rate at which a full charge or discharge takes n hours. (b) 2D figure displaying the time evolution of the {200} reflection during C/5 charging. (c) 2D figure displaying the time evolution of the {200} reflection during 60C charging.

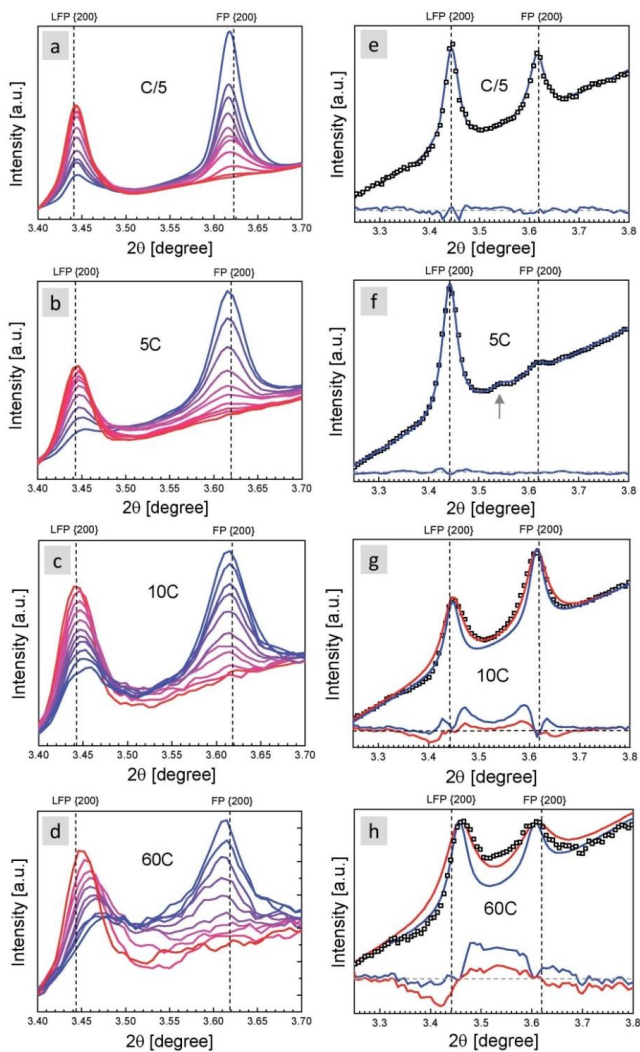


Figure 3.2. (a-d) Evolution of the {200} reflection during C/5, 5C, 10C and 60C charging. The vertical lines indicate the equilibrium {200} position reflecting the equilibrium unit cell parameters a in both the Li-rich (LFP) and Li-poor (FP) phases. (e) Diffraction pattern at approximately 50% state of charge during C/5 charging illustrating excellent fit quality with the equilibrium LFP and FP a -unit cell parameter. (f) Diffraction pattern at approximately 5% state of charge during 5C charging displaying a weak intermediate reflection with the a -lattice parameter equal to 10.03 Å representing a metastable composition between the FP and LFP

phase. (g),(h) Diffraction patterns at approximately 50% state of charge during 10C and 60C charging including two fits. Allowing the peak width to vary results in a better agreement between the fit and the observed intensity, which is sandwiched between the two {200} reflections, but results in a large disagreement between the fit and observed data at the left and right wings of the {200} LFP and {200} FP reflections, respectively. For the blue fit the C/5 peak width (no broadening) is used, which reveals the rate-induced intensity between the two {200} reflections representing intermediate solid-solutions. The Rietveld refinement was performed over the complete patterns (0.03° to 13.3° for the 2θ range at $\lambda = 0.30996 \text{ \AA}$).

This is also reflected in the series of patterns shown in Figure 3.2a-d, again focussing on the {200} reflection for C/5, 5C, 10C and 60C charge rates. In addition to the emergent intensity between the LFP {200} and FP {200} reflections, both reflections increasingly shift towards each other as the phase fractions decrease, an effect that becomes stronger as the charge rate increases. This evidences that the *a*-lattice parameters, directly related to the position of the {200} reflections, progressively approach each other as the charge rate increases. This is also observed for the *b* and *c*-lattice parameters (see figure 3.4.), resulting in the refined unit cell volume displayed in Figure 3.3a. At low rates the unit cell parameters scarcely vary with (dis)charging, as expected from equilibrium thermodynamics. However, at high (dis)charge rates the unit cell parameters change dramatically. Assuming that Vegard's law applies¹⁰ (which is not true if phase coexistence is present¹¹, see below) the unit cell volume is linearly related to the lithium composition. Therefore the unit cell volumes in Figure 3.3a for 60C infer (dis)charge rate induced solid-solution compositions α and β in $\text{Li}_\alpha\text{FePO}_4$ (FP) and $\text{Li}_{1-\beta}\text{FePO}_4$ (LFP) that have not been observed for defect free LiFePO_4 having this relatively large pristine particle size (140 nm). Figure 3.3b shows a difference in unit cell evolution between charging and discharging, demonstrating that the deviation of the unit cell volume from the equilibrium value is largest for the nucleating phase, LFP during discharge and FP during charge. Because diffraction probes the average of all diffracting particles the large shift in unit cell volume for

small phase fractions (both FP and LFP), observed in Figure 3.3a, is in particularly found for the nucleating phase. The increasing phase fraction masks the nucleating fraction explaining the gradual disappearance of the shift in unit cell volume observed in Figure 3.3a. The results imply larger solid-solutions, larger α and β in $\text{Li}_\alpha\text{FePO}_4$ and $\text{Li}_{1-\beta}\text{FePO}_4$, when the LFP and FP phases are nucleating. This is most likely the consequence of the local overpotential required to pass the substantial nucleation barrier¹⁴ initiating larger solid-solution compositions.

The emergent intensity between the Bragg reflections with increasing rate observed in Figure 3.2a-d cannot be explained by the FP and LFP end members. This is illustrated in Figures 3.2e-h where for C/5 rate accurate fits are obtained, however at 60C the patterns cannot be well fitted even if the reflections are allowed to broaden. Interestingly, during the initial charge stages of 5C charging (and 10C charging see figure 3.5), shown in Figure 3.2f, an additional reflection is observed between the LFP and FP {200} reflections. Though weaker, and only observed at the initial stages of charging, it is very similar to the recent observation of a metastable $\text{Li}_{\sim 0.6}\text{FePO}_4$ phase by Orikasa et al.¹⁶ at 10C charge rate in 1 μm particles. This metastable phase is not predicted by modelling studies, that calculate a solid-solution transformation at high (dis)charge rates¹²⁻¹⁴. Most likely this is the consequence of the use of a regular solution model for the Gibbs free energy^{12,13}, disregarding the eutectoid⁴³ which predicts the relative stability of the $\text{Li}_{\sim 0.6}\text{FePO}_4$ phase⁴⁴. The present results indicate the metastable phase to occur at intermediate charge rates when the (dis)charge rate induced phenomena start to set in.

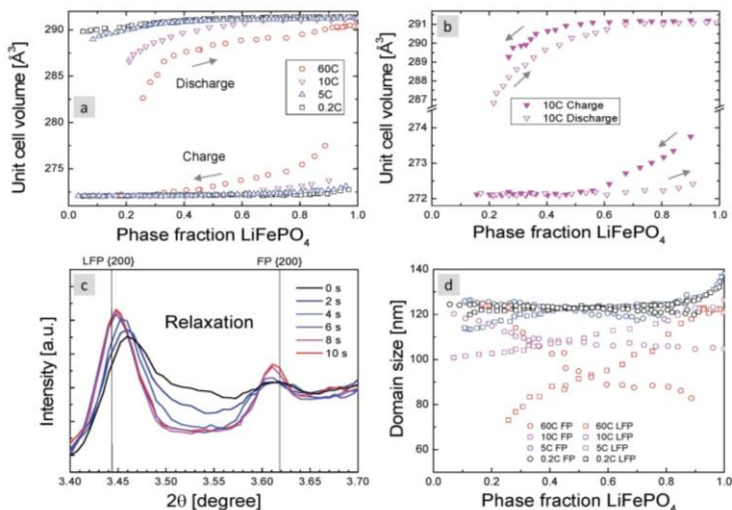


Figure 3.3. (a) Rietveld refined unit cell volume for both the lithium-rich triphylite $\text{Li}_{1-\beta}\text{FePO}_4$ (LFP) and lithium-poor heterosite $\text{Li}_\alpha\text{FePO}_4$ (FP) phases at different (dis)charge rates. (b) Rietveld refined unit cell volume for both the lithium rich triphylite $\text{Li}_{1-\beta}\text{FePO}_4$ (LFP) and lithium poor heterosite $\text{Li}_\alpha\text{FePO}_4$ (FP) phases at 10C during charge and discharge. (c) Relaxation at zero current of the {200} reflections of the Li-rich $\text{Li}_{1-\beta}\text{FePO}_4$ (LFP) and Li-poor $\text{Li}_\alpha\text{FePO}_4$ (FP) phases after 60C charging to approximately 50% state of charge. The diffracted intensity between the {200} LFP and FP end member reflections, indicating the presence of a distribution of solid-solution compositions, disappears in several seconds recovering the (non-shifted) equilibrium {200} LFP and FP end member reflections. This indicates that the solid-solutions are indeed unstable and occur due to the high rate conditions. (d) Evolution of the domains size resulting from Rietveld refinement for both Li-rich $\text{Li}_{1-\beta}\text{FePO}_4$ (LFP) and Li-poor $\text{Li}_\alpha\text{FePO}_4$ (FP) phases.

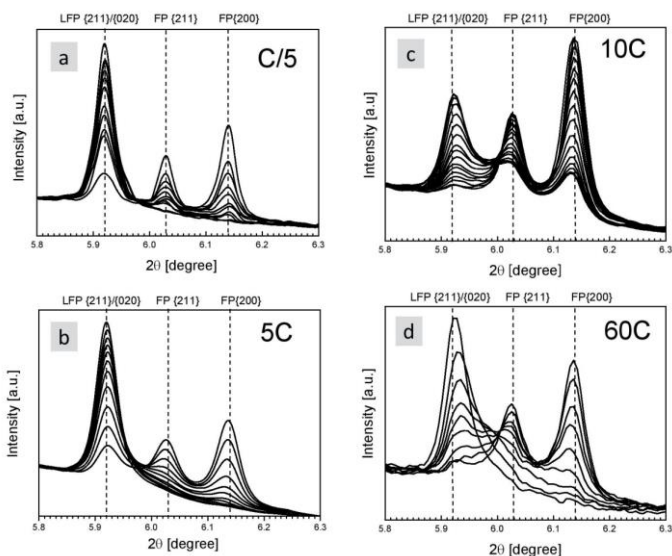


Figure 3.4. (a-d) Evolution of the $\{211\}$ and $\{020\}$ reflections during C/5, 5C, 10C and 60C charging. The vertical lines indicate the equilibrium $\{211\}$ and $\{020\}$ position reflecting the equilibrium unit cell parameters in both the Li-rich (LFP) and Li-poor (FP) phases.

However, the data in Figures 3.2g-h, obtained at 60C and 10C rates, are inconsistent with a single metastable phase. Instead, the intensity distribution between the FP and LFP $\{200\}$ reflections indicates a distribution in lattice parameters. This discloses the presence of a distribution of solid-solution compositions rather than a single metastable phase. Figure 3.3c illustrates that these solid-solution compositions are induced by the dynamic conditions as the distribution of intensities disappears within a few seconds after the 60C charging is interrupted. At low rates the integrated intensity of the reflections during the in-situ (dis)charge experiments remains constant. However, at increasing (dis)charge rate part of the integrated intensity of the end-members Bragg reflections is (reversibly) converted into the distribution of solid solution compositions. The total integrated intensity however remains constant independent of the (dis)charge rate providing no proof for the presence of amorphous phases.⁴⁵

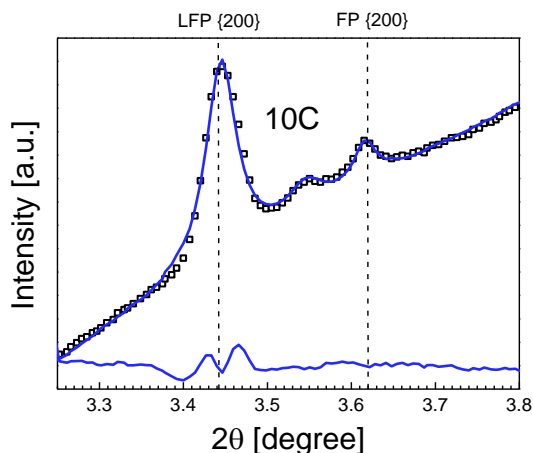


Figure 3.5. Diffraction pattern at approximately 5% state of charge during 10C charging displaying a weak intermediate reflection with the a -lattice parameter equal to 10.03 Å representing a meta stable composition between the FP and LFP phase.

Modelling on a particle level predicts a complete solid-solution transition at high overpotentials¹²⁻¹⁴, in which case diffraction should display a homogeneous shift of the Li-rich phase towards the Li-poor phase. Instead diffraction on the actual electrodes, Figure 3.2c-d, 3.2g-h, shows the presence of the end-member reflections in addition to a distribution of solid-solution compositions. The observed distribution of environments is consistent with the conditions at high (dis)charge rates, which results in a concentration/potential gradient responsible for the observed overpotentials in Figure 3.1a. In these electrodes (carbon coated LFP) the gradient is caused by the rate limiting ionic transport through the electrolyte in the pores of the electrode^{36,38,40,46-48}. At high rates the best ionic wired parts of the electrode will be converted first the worst wired parts last⁴⁸. Locally at the gradient the electrode material is exposed to the overpotential, which is the driving force for the solid-solution transition, bypassing the first-order phase transition. Absent at equilibrium, the increasing potential gradient with increasing rate is responsible for the emerging solid-solution compositions observed. The single phase transition is only induced at the position of the

potential gradient explaining the observation that only a fraction of the electrode material is transforming. The complete physical picture, shown in Figure 3.6a, explains the presence of the observed distribution of environments at 60C. The observation that at low rates a small fraction of particles actively undergo the phase transformation and that this fraction increases with higher rates is in agreement with a modelling study combining the mosaic phase transition by phase fields with ionic and electronic transport in macroscopic porous electrodes⁴⁹. The present results show that at high rates this transforming fraction has a distribution of solid solution compositions between the end-members, except at intermediate rates where in a large fraction of the transforming particles has the metastable $\text{Li}_{0.6}\text{FePO}_4$ phase.

The width of the diffraction peaks is inversely related to the domain size of the crystalline phases assuming no strain-broadening. Figure 3.3d shows that after a small initial drop the LFP and FP domain sizes hardly vary at C/5 rate, whereas higher rates lead to increasing broadening of the reflections, suggesting a smaller size of the phase domains. A complicating factor determining the domain size at higher rates (above 5C) is the distribution of environments that leads to an apparent broadening, see Figure 3.2g-h, not related to domain size broadening. Nevertheless, the Rietveld refinements indicate a significant broadening, independent of the intensity between the Bragg reflections, which increases with the discharge rate. Assuming this broadening is due a reduction in domain size this is qualitatively consistent with phase growth and shrinking of the FP and LFP phases within one particle. However, phase coexistence within each particle should lead to much larger variations in the domain size¹¹. As diffraction probes the average domain size this suggests that phase coexistence only occurs in a small fraction of the particles, while the majority of the particle either has the FP or LFP phase. The greater variation in domain sizes at higher rates indicates a larger fraction of transforming particles at higher rates, consistent with ex-situ diffraction^{30,31} and nano-scale state-of-charge mapping performed after 1C charging¹⁵. The observation of a larger fraction of transforming particles at higher (dis)charge rates is in excellent agreement with the phase field modelling by Bai et al.³⁴ who proposed a statistical model including three populations of particles,

empty, transforming and full. At these high rates particles have less time to exchange lithium to reach the mosaic phase distribution in which the particles either have the FP or the LFP phase, avoiding the energy penalty for intra particle phase boundaries^{12-14,24,50}.

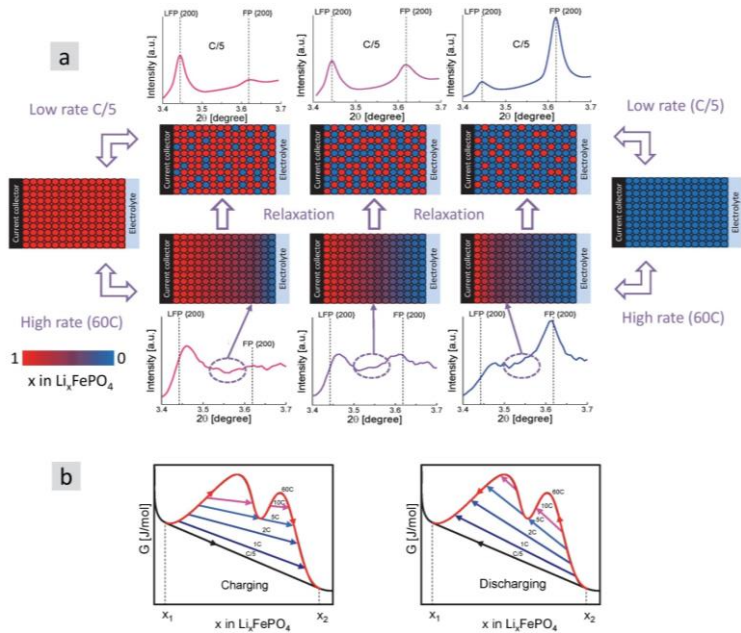


Figure 3.6. (a) Model for the phase distribution in LiFePO_4 electrodes at high and low rates and upon relaxation. At low rates the electrode is near equilibrium and no significant Li-concentrations/overpotentials exist through the electrode. As a consequence, the phase transition occurs randomly throughout the electrode and only the LFP and FP end member phases are observed. At high rates the overpotential results in a potential gradient that moves through the electrode from the easy to the difficult Li-ion accessed/depleted region, assuming Li-ion transport to be rate limiting. For simplicity the model assumes the easy accessible part of the electrode to be located at the interface with the electrolyte, and the difficult accessible part to be located at the electrode side. At the location of the potential gradient the electrode material experiences the high overpotentials that

are responsible for the solid-solution compositions observed. In addition parts of the electrode that have been converted and are not converted yet explain the simultaneous observation of the end members and the distribution of solid-solution compositions at high rates. (b) Schematic explanation of the rate dependent phase transformation mechanism for a single particle based on the Gibbs free energy, left during charging, right during discharging. At low rates the phase transformation follows the common tangent predicted by thermodynamics leading to the solid solution compositions $Li_{\alpha=x_1}FePO_4$ and $Li_{1-\beta=x_2}FePO_4$ in FP and LFP, respectively. Increasing the rate results in larger overpotentials that raise the Gibbs Free energy leading to larger solid solutions α and β , the observation of the metastable $Li_{x\sim 0.6}FePO_4$ composition and finally to bypassing the first order phase transition completely.

For individual particles three stages can be distinguished in the Li_xFePO_4 phase transition kinetics, summarized in the schematic Gibbs free energy diagram in Figure 3.6b, which includes the relative stability of the $Li_{\sim 0.6}FePO_4$ phase consistent with experimental observations^{43,44}. At C/5, (dis)charging leads to the first-order phase transition predicted by bulk thermodynamics, following the common tangent construction in the Gibbs free energy diagram. This leads to the appearance and disappearance of the FP and LFP phases without a change in compositions/lattice parameters, reflected by Figure 3.3a. The larger overpotentials due to higher (dis)charge rates drive the LFP and FP phases to higher free energies, resulting in larger solid-solutions and a gradual decrease of the miscibility gap as illustrated by Figure 3.3a. At this stage the first-order phase transition is not able to keep up with the fast diffusion through the electrode material. The angle of the transition lines reflects the impact of the potential gradient, imposing a larger solid-solution in the nucleating phase, which explains the difference between charging and discharging observed in Figure 3.3b. At 5C/10C the higher transition line hits the metastable $Li_{\sim 0.6}FePO_4$ phase, resulting in the observation in Figure 3.2f consistent with Orikasa et al.¹⁶ Finally, at 60C the movement of the large potential gradient locally drives the electrode material through a complete solid-solution transition, as predicted by

phase field modelling^{12,13}, resulting in the presence of all intermediate compositions as observed in Figure 3.2d and 3.2h.

3.4 Conclusions

In summary, a complete and consistent picture of the equilibrium and non-equilibrium phase transformations in LiFePO_4 is presented based on the rate dependent diffraction experiments categorized in three phase transformation stages; (1) near equilibrium displaying the expected first-order phase transition between FP and LFP is displayed. (2) Intermediate rates lead to the observation of the $\text{Li}_{\sim 0.6}\text{FePO}_4$ metastable phase challenging the use of a regular solution model by theorists. (3) The most spectacular observation is at 10C up to 60C where the solubility limits in both phases increase dramatically with increasing (dis)charge rate causing a fraction of the electrode material to follow a single phase transformation path, bypassing the first-order phase transition. At low (dis)charge rates the mosaic transformation is observed whereas at high (dis)charge rates an increasing fraction of transforming particles is observed as recently predicted by phase field modelling. The results demonstrate that the phase transformation path in the Li_xFePO_4 system depends on the (dis)charge rate (overpotential) providing a rationale for the remarkable fast kinetics of LiFePO_4 . Nucleation rates are consequently not limiting the transformation rate and thereby these new findings reveal that improvement of electrode performance should focus on optimization the ionic/electronic transport in LiFePO_4 electrodes.

References

- 1 Padhi, A. K., Nanjundaswamy, K. S. & Goodenough, J. B. Phospho-olivines as positive-electrode materials for rechargeable lithium batteries. *J. Electrochem. Soc.* **144**, 1188-1194 (1997).
- 2 Ravet, N. e. a. in *Electrochemical Society Fall Meeting, Honolulu, Hawaii (Electrochemical Society, Pennington, New Jersey, 1999)* (1999).
- 3 Huang, H., Yin, S. C. & Nazar, L. F. Approaching theoretical capacity of LiFePO₄ at room temperature at high rates. *Electrochemical and Solid State Letters* **4**, A170-A172 (2001).
- 4 Herle, P. S., Ellis, B., Coombs, N. & Nazar, L. F. Nano-network electronic conduction in iron and nickel olivine phosphates. *Nat. Mater.* **3**, 147-152 (2004).
- 5 Gaberscek, M., Dominko, R. & Jamnik, J. Is small particle size more important than carbon coating? An example study on LiFePO₄ cathodes. *Electrochemistry Communications* **9**, 2778-2783, doi:10.1016/j.elecom.2007.09.020 (2007).
- 6 Wang, Y., Wang, Y., Hosono, E., Wang, K. & Zhou, H. The design of a LiFePO₄/carbon nanocomposite with a core-shell structure and its synthesis by an in situ polymerization restriction method. *Angewandte Chemie-International Edition* **47**, 7461-7465, doi:10.1002/anie.200802539 (2008).
- 7 Gibot, P. *et al.* Room-temperature single-phase Li insertion/extraction in nanoscale Li_xFePO₄. *Nature Materials* **7**, 741-747, doi:10.1038/nmat2245 (2008).
- 8 Yamada, A. *et al.* Room-temperature miscibility gap in Li_xFePO₄. *Nat. Mater.* **5**, 357-360 (2006).
- 9 Kobayashi, G. *et al.* Isolation of Solid Solution Phases in Size-Controlled Li_xFePO₄ at Room Temperature. *Advanced Functional Materials* **19**, 395-403, doi:10.1002/adfm.200801522 (2009).
- 10 Meethong, N., Huang, H. Y. S., Carter, W. C. & Chiang, Y. M. Size-dependent lithium miscibility gap in nanoscale Li_{1-x}FePO₄. *Electrochemical and Solid State Letters* **10**, A134-A138 (2007).

- 11 Wagemaker, M. *et al.* Dynamic Solubility Limits in Nanosized Olivine LiFePO_4 . *Journal of the American Chemical Society* **133**, 10222-10228, doi:10.1021/ja2026213 (2011).
- 12 Bai, P., Cogswell, D. A. & Bazant, M. Z. Suppression of Phase Separation in LiFePO_4 Nanoparticles During Battery Discharge. *Nano Letters* **11**, 4890-4896, doi:10.1021/nl202764f (2011).
- 13 Cogswell, D. A. & Bazant, M. Z. Coherency Strain and the Kinetics of Phase Separation in LiFePO_4 Nanoparticles. *Acs Nano* **6**, 2215-2225, doi:10.1021/nn204177u (2012).
- 14 Malik, R., Zhou, F. & Ceder, G. Kinetics of non-equilibrium lithium incorporation in LiFePO_4 . *Nature Materials* **10**, 587-590, doi:10.1038/nmat3065 (2012).
- 15 Chueh, W. C. *et al.* Intercalation Pathway in Many-Particle LiFePO_4 Electrode Revealed by Nanoscale State-of-Charge Mapping. *Nano Letters* **13**, 866-872, doi:10.1021/nl3031899 (2013).
- 16 Orikasa, Y. *et al.* Direct Observation of a Metastable Crystal Phase of Li_xFePO_4 under Electrochemical Phase Transition. *Journal of the American Chemical Society* **135**, 5497-5500, doi:10.1021/ja312527x (2013).
- 17 Zhou, F., Marianetti, C. A., Cococcioni, M., Morgan, D. & Ceder, G. Phase separation in Li_xFePO_4 induced by correlation effects. *Physical Review B* **69** (2004).
- 18 Cogswell, D. A. & Bazant, M. Z. Theory of Coherent Nucleation in Phase-Separating Nanoparticles. *Nano Letters* **13**, 3036-3041, doi:10.1021/nl400497t (2013).
- 19 Rodriguez-Carvajal, J. *Recent Developments of the Program FULLPROF, in CPD Newsletter 2001, 26, 12, available at* <<http://www.ill.eu/sites/fullprof/index.html>>.
- 20 Badi, S.-P. *et al.* Direct synthesis of nanocrystalline $\text{Li}_{0.90}\text{FePO}_4$: observation of phase segregation of anti-site defects on delithiation. *Journal of Materials Chemistry* **21**, 10085-10093, doi:10.1039/c0jm04378h (2011).

- 21 Delacourt, C., Poizot, P., Tarascon, J. M. & Masquelier, C. The existence of a temperature-driven solid solution in Li_xFePO_4 for $0 \leq x \leq 1$. *Nat. Mater.* **4**, 254-260 (2005).
- 22 Stevens, R. *et al.* Phonons and thermodynamics of unmixed and disordered $\text{Li}_{0.6}\text{FePO}_4$. *Journal of Physical Chemistry B* **110**, 22732-22735, doi:10.1021/jp0638311 (2006).
- 23 Burch, D. & Bazant, M. Z. Size-Dependent Spinodal and Miscibility Gaps for Intercalation in Nanoparticles. *Nano Letters* **9**, 3795-3800, doi:10.1021/nl9019787 (2009).
- 24 Wagemaker, M., Borghols, W. J. H. & Mulder, F. M. Large impact of particle size on insertion reactions, A case of anatase LiTiO_2 . *J. Am. Chem. Soc.* **129**, 4323 (2007).
- 25 Schimmel, H. G., Huot, J., Chapon, L. C., Tichelaar, F. D. & Mulder, F. M. Hydrogen cycling of niobium and vanadium catalyzed nanostructured magnesium. *J. Am. Chem. Soc.* **127**, 14348-14354 (2005).
- 26 Borghols, W. J. H., Wagemaker, M., Lafont, U., Kelder, E. M. & Mulder, F. M. Impact of nanosizing on lithiated rutile TiO_2 . *Chemistry of Materials* **20**, 2949-2955, doi:10.1021/cm703376e (2008).
- 27 Sharma, N. *et al.* Direct Evidence of Concurrent Solid-Solution and Two-Phase Reactions and the Nonequilibrium Structural Evolution of LiFePO_4 . *Journal of the American Chemical Society* **134**, 7867-7873, doi:10.1021/ja301187u (2012).
- 28 Dreyer, W. *et al.* The thermodynamic origin of hysteresis in insertion batteries. *Nature Materials* **9**, 448-453, doi:10.1038/nmat2730 (2010).
- 29 Dreyer, W., Guhlke, C. & Huth, R. The behavior of a many-particle electrode in a lithium-ion battery. *Physica D-Nonlinear Phenomena* **240**, 1008-1019, doi:10.1016/j.physd.2011.02.011 (2011).
- 30 Delmas, C., Maccario, M., Croguennec, L., Le Cras, F. & Weill, F. Lithium deintercalation in LiFePO_4 nanoparticles via a domino-cascade model. *Nature Materials* **7**, 665-671, doi:10.1038/nmat2230 (2008).

- 31 Brunetti, G. *et al.* Confirmation of the Domino-Cascade Model by LiFePO₄/FePO₄ Precession Electron Diffraction. *Chemistry of Materials* **23**, 4515-4524, doi:10.1021/cm201783z (2011).
- 32 Sasaki, T., Ukyo, Y. & Novak, P. Memory effect in a lithium-ion battery. *Nature Materials* **12**, 569-575, doi:10.1038/nmat3623 (2013).
- 33 Laffont, L. *et al.* Study of the LiFePO₄/FePO₄ two-phase system by high-resolution electron energy loss spectroscopy. *Chemistry of Materials* **18**, 5520-5529, doi:10.1021/cm0617182 (2006).
- 34 Bai, P. & Tian, G. Y. Statistical kinetics of phase-transforming nanoparticles in LiFePO₄ porous electrodes. *Electrochimica Acta* **89**, 644-651, doi:10.1016/j.electacta.2012.11.070 (2013).
- 35 Levi, M. D. *et al.* Collective Phase Transition Dynamics in Microarray Composite Li_xFePO₄ Electrodes Tracked by in Situ Electrochemical Quartz Crystal Admittance. *Journal of Physical Chemistry C* **117**, 15505-15514, doi:10.1021/jp403653d (2013).
- 36 Jamnik, J. *et al.* Stabilizers of Particle Size and Morphology: a Road Towards High-Rate Performance Insertion Materials. *Advanced Materials* **21**, 2715-+, doi:10.1002/adma.200803032 (2009).
- 37 Kang, B. & Ceder, G. Battery materials for ultrafast charging and discharging. *Nature* **458**, 190-193, doi:10.1038/nature07853 (2009).
- 38 Singh, D. P., Mulder, F. M., Abdelkader, A. M. & Wagemaker, M. Facile Micro Templating LiFePO₄ Electrodes for High Performance Li-Ion Batteries. *Advanced Energy Materials* **3**, 572-578, doi:10.1002/aenm.201200704 (2013).
- 39 Kim, D. H. & Kim, J. Synthesis of LiFePO₄ nanoparticles in polyol medium and their electrochemical properties. *Electrochemical and Solid State Letters* **9**, A439-A442, doi:10.1149/1.2218308 (2006).
- 40 Gaberscek, M. & Jamnik, J. Impact of electrochemical wiring topology on the kinetics of insertion electrodes. *Solid State Ionics* **177**, 2647-2651, doi:10.1016/j.ssi.2006.02.035 (2006).

- 41 Bazant, M. Z. Theory of Chemical Kinetics and Charge Transfer based on Nonequilibrium Thermodynamics. *Accounts of Chemical Research* **46**, 1144-1160, doi:10.1021/ar300145c (2013).
- 42 Orikasa, Y. *et al.* Transient Phase Change in Two Phase Reaction between LiFePO₄ and FePO₄ under Battery Operation. *Chemistry of Materials* **25**, 1032-1039, doi:10.1021/cm303411t (2013).
- 43 Dodd, J. L., Yazami, R. & Fultz, B. Phase diagram of Li(x)FePO₄. *Electrochemical and Solid State Letters* **9**, A151-A155, doi:10.1149/1.2164548 (2006).
- 44 Delacourt, C., Rodriguez-Carvajal, J., Schmitt, B., Tarascon, J. M. & Masquelier, C. Crystal chemistry of the olivine-type Li_xFePO₄ system (0 <= x <= 1) between 25 and 370 degrees C. *Solid State Sciences* **7**, 1506-1516, doi:10.1016/j.solidstatesciences.2005.08.019 (2005).
- 45 Meethong, N. *et al.* Electrochemically Induced Phase Transformation in Nanoscale Olivines Li_{1-x}MPO₄ (M = Fe, Mn). *Chemistry of Materials* **20**, 6189-6198, doi:10.1021/cm801722f (2008).
- 46 Doyle, M. & Newman, J. Analysis of capacity-rate data for lithium batteries using simplified models of the discharge process. *Journal of Applied Electrochemistry* **27**, 846-856, doi:10.1023/a:1018481030499 (1997).
- 47 Fongy, C., Jouanneau, S., Guyomard, D., Badot, J. C. & Lestriez, B. Electronic and Ionic Wirings Versus the Insertion Reaction Contributions to the Polarization in LiFePO₄ Composite Electrodes. *Journal of the Electrochemical Society* **157**, A1347-A1353, doi:10.1149/1.3497353 (2010).
- 48 Wiedemann, A. H., Goldin, G. M., Barnett, S. A., Zhu, H. Y. & Kee, R. J. Effects of three-dimensional cathode microstructure on the performance of lithium-ion battery cathodes. *Electrochimica Acta* **88**, 580-588, doi:10.1016/j.electacta.2012.10.104 (2013).
- 49 Ferguson, T. R. & Bazant, M. Z. Nonequilibrium Thermodynamics of Porous Electrodes. *Journal of the Electrochemical Society* **159**, A1967-A1985, doi:10.1149/2.048212jes (2012).

- 50 Wagemaker, M., Mulder, F. M. & van der Ven, A. The role of surface and interface energy on phase stability of nanosized insertion compounds. *Adv.Mater.***21**,1-7(2009).

Chapter 4

Direct view on the phase evolution in individual LiFePO₄ nanoparticles during cycling of Li-ion battery electrodes

Based on the paper : '*Direct view on the phase evolution in individual LiFePO₄ nanoparticles during cycling of Li-ion battery electrodes*'

Xiaoyu Zhang, Martijn van Hulzen, Deepak P. Singh, Alex Brownrigg, Jonathan P. Wright, Niels H. van Dijk and Marnix Wagemaker* *Nature Communication*, 6, 8333, (2015)

Abstract

Phase transitions in Li-ion electrode materials during (dis)charge are decisive for battery performance, limiting high-rate capabilities and playing a crucial role in the cycle life of Li-ion batteries. However, the difficulty to probe the phase nucleation and growth in individual grains is hindering fundamental understanding and progress. Here we present a novel approach using synchrotron micro-beam diffraction disclosing the cycling-rate dependent phase transition mechanism within individual particles of LiFePO₄, a key Li-ion electrode material. At low (dis)charge rates well-defined nanometer thin-plate shaped domains coexist and transform much slower and concurrent as compared to the commonly assumed mosaic transformation mechanism. As the (dis)charge rate increases, phase boundaries become diffuse, speeding up the transformation rates of individual grains. Direct observation of the transformation of individual grains reveals that local current densities significantly differ from what has previously been assumed, giving new insights in the working of Li-ion battery electrodes and their potential improvements.

4.1 Introduction

Electrochemical energy storage in Li-ion batteries has enabled the development of today's portable electronics and is expected to be the key technology for electrical vehicles, as well as for lifting the difference between supply and demand of renewable energy sources. The working of Li-ion batteries is based on the reversible insertion and extraction of Li-ions in the crystal structure of the positive and negative electrode materials resulting in highly efficient and high density energy storage. Large volume changes, associated with phase transitions in the electrode material, typically result in poor cycle performance by mechanical failure. In addition, the formation of interfaces, that occur as a result of the phase transformation, are associated with a poor rate performance, whereas solid solution reactions typically lead to high (dis)charge rates.

Generally, the overall phase transformation behavior of Li-ion battery electrode materials is well known. For instance the intensively studied model system and important LiFePO_4 ^{1,2} positive electrode material combines a first-order phase transition with surprisingly high-rate performance and cycle life³⁻⁸. The high rate performance has recently been explained by the possibility to bypass the two-phase reaction through a solid solution reaction at high rates^{9,10} as predicted by modelling¹¹⁻¹³.

However, even for well-studied electrode materials such as LiFePO_4 ^{1,2} it is unknown how the transformation proceeds in individual grains and how it is distributed over the many particles present in an electrode. This is crucial information as the local conditions govern the Li-ion battery cycle life and rate performance, and are key towards the interpretation of easy to measure macroscopic electrochemical parameters. For example, the transformation rate of individual grains defines the maximum (dis)charge current that can be achieved by Li-ion battery electrodes. In addition, it determines what fraction of the electrode is concurrently transforming, which in case of a small active fraction carries a large fraction of the overall current¹⁴ leading to local hotspots that are detrimental for the cycle life^{15,16}. Large local current densities in LiFePO_4 are predicted based on the particle-by-particle, or mosaic, transformation^{14,17-25} mechanism, avoiding

phase coexistence within individual crystallites. The formulation of the particle-by-particle transformation is based on the absence of phase coexistence within individual crystallites as first suggested by ex-situ powder X-ray diffraction¹⁷ and subsequently supported by ex-situ electron^{18,19} and X-ray microscopy^{14,20}. However, the particle-by-particle (mosaic) transformation at low rates is not undisputed, as in-situ Neutron Diffraction²⁶ supports a more concurrent transformation in LiFePO_4 . The associated phase coexistence has also been observed with ex-situ²⁷⁻²⁹ TEM, recent in-situ TEM^{30,31} and IR spectroscopy³², challenging the particle-by-particle transformation mechanism.

The restricted knowledge of the local phase transition behaviour in LiFePO_4 , and of insertion electrodes in general, is at least partially the consequence of the absence of experimental techniques with sufficient space and time resolution to monitor the nucleation and growth mechanism within individual grains and their distribution over the electrode grains under realistic (dis)charge conditions. This hinders direct insight in crucial battery properties, such as the cycling rate and cycle life, which is paramount for the development of electrodes with improved rate and cycle performance.

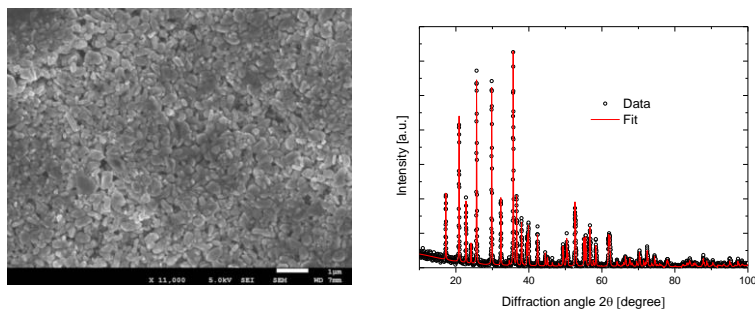


Figure 4.1. Left: SEM picture of the pristine LiFePO_4 material with an average particle size of 140 nm. Right: XRD ($\text{Cu-K}\alpha$) of the pristine LiFePO_4 material including fit (orthorhombic $Pnma$ space group) yielding lattice parameters $a = 10.329 \text{ \AA}$, $b = 6.007 \text{ \AA}$ and $c = 4.691 \text{ \AA}$.

In this study for the first time operando micro-beam X-ray diffraction is employed to monitor the transformation of many individual LiFePO_4 particles inside a Li-ion battery electrode from low to high cycling rates. Due to the micron sized and bright X-ray beam, the diffraction rings that are observed by powder diffraction break up into individual spots, each representing an individual nanosized LiFePO_4 grain (140 nm average particle size with no apparent preferential shape, XRD and SEM shown in Figure 4.1) in the battery electrode, as schematically shown in Figure 4.2a (See also Figure 4.2b for a typical raw data 2D micro beam diffraction pattern). Here we refer to a single grain or particle as a single crystallite as opposed to particles that exist of a number of agglomerated crystallites. The high X-ray energy of 40 keV is transmitted by the coffee bag cells which comprise of a Li-metal negative electrode and a LiFePO_4 (carbon-coated 140 nm crystallites) positive electrode. For the prepared LiFePO_4 electrodes the micron sized beam leads to typically tens of LiFePO_4 grains that are in the diffraction conditions.

Rotation of the cells over an angle ω perpendicular to the X-ray beam brings more grains in the diffraction condition and hence increases the chance to monitor transforming grains over time. In this way the phase transition behaviour of many individual grains (≈ 150 in the present experiment) is monitored as a function of time, while varying the electrochemical conditions from slow ($C/50$) up to fast rates ($2C$), where C/n denotes the rate at which a full charge or discharge takes n hours.

4.2 Experimental Methods

Sample preparation. The starting material was carbon coated LiFePO₄ from Phostech with an average particle size of 140 nm. LiFePO₄ cathodes were prepared through mixing a slurry of LiFePO₄, Carbon Black (Super P), PVDF, (polyvinylidene fluoride, Solvay) in NMP (N-methylpyrrolidone, with a mass ratio of the active material (LiFePO₄), carbon black (SuperP) and binder (PVDF) of 80:10:10. The final slurry was casted on carbon coated Aluminium current collectors by doctor blading. The coatings were dried on a heater plate under air at approximately 155 °C overnight followed by drying under vacuum at around 60 °C for more than 24 hours. The resulting coatings were pressed using a roller hand press to enhance the electronic contact. Finally, the electrodes are dried for at least 3 hours under vacuum at 100 °C.

Battery preparation and testing. The electrodes were assembled in 'coffee-bag' type cells under argon atmosphere (<0.1 ppm O₂/H₂O). The electrodes were separated by glass microfiber filters (Whatman) with a few droplets of 1 mol/liter LiPF₆ (EC:DMC 1:1, Novolyte) electrolyte. All the electrochemical tests were performed galvanostatically within a voltage window of 4.3 and 2.5 V vs Li/Li⁺ using an Autolab PGSTAT302N potentiostat/galvanostat.

Operando Synchrotron X-Ray Diffraction. The in-situ synchrotron XRD experiments were performed at the ID11 beam line of the European Synchrotron Radiation Facility (ESRF Grenoble, France). Figure 4.2a shows the experiment set up. A monochromatic X-ray with an energy of 40 keV (wavelength 0.30996 Å) and a beam size of 1.7 μm was used to illuminate the coffee bag cell. The grains that fulfilled the Bragg condition generated a diffraction spot on the 2D FReLoN2k CCD detector placed behind the sample. During exposure the sample was continuously rotated around the axis perpendicular to the X-ray beam over an angular range 0.5° with an exposure time of 10 s (C/50, C/5, C/2) or 5 s (2C). By collecting several subsequent angular exposures a total angular range of 6° (2C, C/50) or 12° (C/2, C/5) was covered, resulting in a time resolution for individual measurements

cycles of 1 min (2C), 4 min (C/2, C/5) and 2 min (C/50). The instrument parameter were determined using CeO₂ as calibrant. (NIST SRM 674b)

4.3 Analytical Methods

Relation between the streak peak profile and the platelet domain thickness

The peak profile $I(\mathbf{Q})$ of the scattered intensity originating from a single particle at the Bragg condition $\mathbf{Q} = \mathbf{Q}_{hkl} + \mathbf{q}$ can be described by the form factor of the particle $F(\mathbf{q})$ as $I(\mathbf{Q}) \propto |F(\mathbf{q})|^2$. The form factor of a uniform rectangular bar (parallelepiped) corresponds to³³⁻³⁵:

$$F(\mathbf{q}) = L_x L_y L_z \left(\frac{\sin(q_x L_x / 2)}{q_x L_x / 2} \right) \left(\frac{\sin(q_y L_y / 2)}{q_y L_y / 2} \right) \left(\frac{\sin(q_z L_z / 2)}{q_z L_z / 2} \right) \quad (4-1)$$

where L_x , L_y and L_z are the dimensions of the bar along the x , y and z directions. When the two in-plane dimensions can be assumed to be large only the plate thickness results in peak broadening. The scattered intensity then corresponds to:

$$I(\mathbf{Q}) \propto |F(\mathbf{q})|^2 \rightarrow (2\pi)^2 L_x L_y L_z^2 \delta(q_x) \delta(q_y) \left(\frac{\sin(q_z L_z / 2)}{q_z L_z / 2} \right)^2 \quad (4-2)$$

where the plate normal is along the z direction. The full width at half maximum (FWHM) amounts to $\Delta q_z \approx 0.886 \times 2\pi / L_z$.

Reflection condition for streaks

For a scattering angle 2θ and an azimuth angle η on the 2D detector the \mathbf{Q} vector corresponds to $\mathbf{Q} = (Q_x, Q_y, Q_z) = (-\sin\theta, -\cos(\theta)\sin(\eta), \cos(\theta)\cos(\eta))$ in laboratory coordinates. For a given rotation angle $\Delta\omega$ around the vertical axis the rotated coordinates are given by:

$$\mathbf{Q}' = (Q_x \cos(\Delta\omega) - Q_y \sin(\Delta\omega), Q_x \sin(\Delta\omega) + Q_y \cos(\Delta\omega), Q_z) \quad (4-3)$$

As the form factor is sharply peaked in reciprocal space, we only expect to observe streaks, originating from nanoscale plate structures, when Q_z is unaffected by the continuous sample rotation of 0.5° during exposure. This is only the case when the plate normal is aligned along the z direction. Otherwise, the plate will quickly rotate out of the reflection condition. The measured peak intensity after exposure at a constant rotation speed corresponds to:

$$I = \int_{\omega}^{\omega+\Delta\omega} I(\mathbf{Q}) d\omega' \quad (4-4)$$

For randomly plates the effective time the particle is in reflection is short, while for aligned particles streaks will be visible.

Orientation of the plate normal with respect to the crystalline \mathbf{a} axis

For observed (200) reflections of the LFP and FP phases the \mathbf{Q} vector corresponds to $\mathbf{Q} = \mathbf{Q}_{200} = (-\sin\theta, -\cos(\theta)\sin(\eta), \cos(\theta)\cos(\eta))$, where 2θ is the scattering angle and an azimuth angle η on the 2D detector. The orientation of \mathbf{Q} is equal to the reciprocal-space \mathbf{a}^* axis, which for an orthorhombic lattice is aligned to the real-space \mathbf{a} axis ($Q_{200} \parallel \mathbf{a}^* \parallel \mathbf{a}$). For our current experimental conditions streaks are only observed when the plate normal \mathbf{n} is oriented vertical ($\mathbf{n} \parallel \mathbf{z}$). As the scattering angle 2θ of the (200) reflections for and are 3.44° (LFP) and 3.62° (FP), we find $\mathbf{Q}_{200} \approx (0, -\sin(\eta), \cos(\eta))$. This means that the azimuth angle η is about equal to the angle between the plate normal and the \mathbf{a} axis of the LFP and FP phases when the (200) reflection is analyzed. For reflections on top ($\eta = 0^\circ$) and bottom ($\eta = 180^\circ$) of the diffraction ring the plate normal is aligned with the \mathbf{a} axis. For reflections at the left and right extremes on the diffraction ring ($\eta = 90^\circ$ and $\eta = 270^\circ$) the plate normal is perpendicular to the \mathbf{a} axis.

Determination of the grain volume

For diffraction spots the integrated intensity I_g is directly related to the grain volume V_g ^{36,37} by:

$$I_g = \Phi_0 r_0^2 \frac{\lambda^3 |F_{hkl}|^2 V_g}{\Delta\omega |\sin \eta| v^2} L_g P T_r \exp(-2M) \quad (4-5)$$

where Φ_0 is the incident flux of photons, F_{hkl} is the structure factor of the (hkl) reflection, λ is the photon wavelength, $\Delta\omega$ is the angular range over which the grain is rotated, v is the volume of the unit cell, P is the polarization factor, and T_r is the transmission factor. The Lorentz factor of the grain is given by $L_g = 1/\sin(2\theta)$, where 2θ is the scattering angle, r_0 is the Thomson scattering length and $\exp(-2M)$ is the Debye-Waller factor.

For a powder diffraction experiment, the integrated intensity I_p of a diffraction ring of a polycrystalline material with randomly oriented grains is given by:

$$I_p = \Phi_0 r_0^2 \frac{m_{hkl} \lambda^3 |F_{hkl}|^2 V}{v^2} L_p P T_r \exp(-2M) \quad (4-6)$$

where m_{hkl} is the multiplicity factor of the ring and V is the volume of the diffracting phase, and $L_p = 1/\{4\sin(\theta)\}$ is the Lorentz factor for an integrated powder ring. The volume of the diffracted phase is equal to $V = f V_{\text{gauge}}$, where f is the volume fraction of the diffracted phase and V_{gauge} is the gauge volume, which is defined by the beam size and the thickness of the sample. The layer thickness was 10.8(4) μm . With a phase fraction of 80% for the active phase and a porosity of 34% the phase fraction is $f = 0.80 \times 0.66 \times f_{\text{LFP/FP}} = 0.53 \times f_{\text{LFP/FP}}$.

The volume of an individual grain is calculated from the integrated intensity of an individual (hkl) reflection normalized by the powder intensity of the ring in which the reflection from the individual grain appeared:

$$V_g = \frac{1}{2} m_{hkl} \Delta\omega |\sin \eta| \cos(\theta) f V_{\text{gauge}} \left(\frac{I_g}{I_p} \right) \quad (4-7)$$

4.4 Results and Discussion

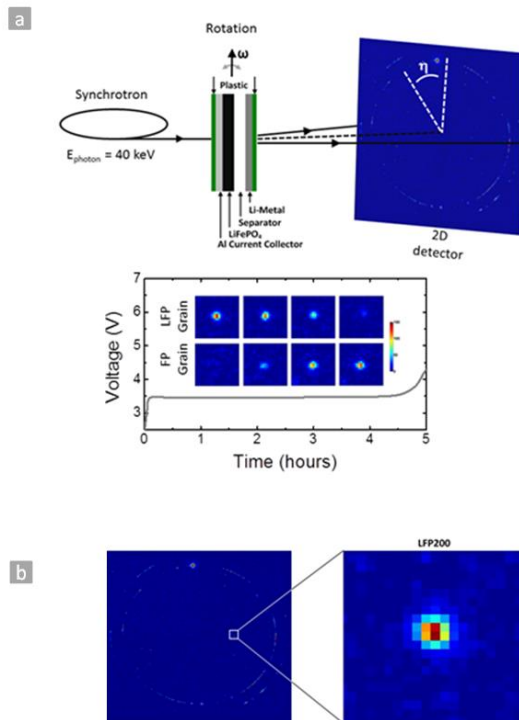


Figure 4.2. (a)Top: Schematic representation of the in-situ synchrotron X-Ray diffraction experiment. During the exposure the sample was continuously rotated around the vertical axis. Bottom: Charging voltage curve (C/5) including the evolution of a 2D (200) LFP and (200) FP peak showing the progressive FP formation and LFP disappearance. (b) Example of a 2D XRD micro-beam pattern with an enlarged picture of a single (200) reflection of the LiFePO_4 phase, representing a single grain in the electrode.

The intensity of a single diffraction spot on a specific diffraction ring (defined by the diffraction angle θ) and position on the diffraction ring (defined by the azimuth angle η) represents the phase volume (of the phase corresponding that specific θ) in an individual LiFePO_4 grain. Therefore, measuring the 2D diffraction patterns as shown in Figure 4.2(a) allows to monitor the intensity of many individual LiFePO_4 grains during operando (dis)charging, providing direct

information on the time evolution and shape of phase domains in individual LiFePO_4 grains. This is illustrated in Figure 4.2(a) showing the evolution of the (200) reflection of a single LFP grain and a single FP grain during charge, where the gradual disappearance of the (200) LFP and appearance of the (200) FP diffraction peaks reflect the first-order phase transition (in a second order transition the peak would shift gradually in position).

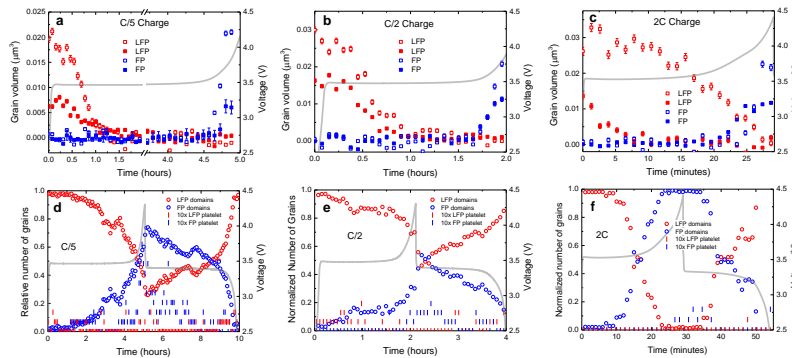


Figure 4.3. (a-c) Volume evolution of two LFP and FP domains during C/5, C/2 and 2C (dis)charge rate including the corresponding voltage curves. (d-f) Evolution of the relative number of LFP and FP grains, and the fraction 10x of which are streaks during different (dis)charge rates including the corresponding voltage curves.

Counting the number of FP and LFP reflections from individual grains during cycling, shown in Figures 4.3d-f, reflects the reversible transformation from LFP to FP and back for the approximately 150 grains that were monitored. The intensity evolution of the reflections reveals for the first time the transformation of individual grains in electrode materials during cycling, as shown for two FP and two LFP grains in Figures 4.3a-c for cycling rates of C/5 up to 2C. Averaging the transformation time of the approximately 150 grains, the distribution of which is shown in 4.4 Figure 4.4, results in the average transformation time. At a relatively slow cycling rate of C/5 the average transformation time of individual crystallites is found to be $\langle \Delta t \rangle_{\text{LFP}} = 66$ min and $\langle \Delta t \rangle_{\text{FP}} = 37$ min (see Figure 4.4). This relatively slow transformation of individual LiFePO_4 crystallites opposes the fast

transformation suggested by the currently most widely accepted particle-by-particle transformation^{14,17-20}.

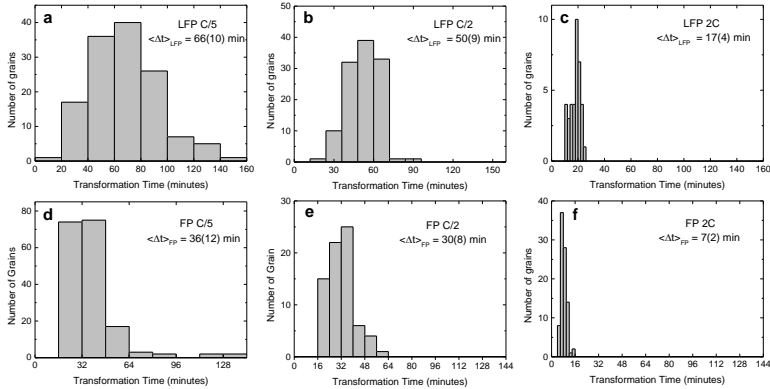


Figure 4.4. Distribution of grain transformation times with the average transformation time $\langle \Delta t \rangle$ for individual LFP and FP grains at different cycling rates.

The transformation time for 100-200 nm particles has been suggested to be of the order of a minute at these relatively low (dis)charge rates, assuming a surface reaction limited process¹⁴. The consequence of the much larger transformation times observed at present is that also the fraction of actively transforming particles (on average 22% during charge and 12% during discharge) is much larger than expected based on the particle-by-particle transformation¹⁴. Interestingly, Figures 4.3a-c show that increasing the (dis)charge rate also increases the transformation rate. At C/2 the average transformation time decreases slightly to $\langle \Delta t \rangle_{LFP} = 50$ min and $\langle \Delta t \rangle_{FP} = 31$ min, whereas it decreases significantly at 2C to $\langle \Delta t \rangle_{LFP} = 17.6$ min and $\langle \Delta t \rangle_{FP} = 7.8$ min (see Figure 4.4). Although the transformation time decreases, the shorter (dis)charge time results in an increasing actively transforming fraction for increasing (dis)charge rates in qualitative agreement with recent findings¹⁴, albeit having much larger values, amounting almost 60% during 2C charge and 26% during 2C discharge. This shows that the increased current at higher (dis)charge rates is realized by both increasing

the transformation rate of individual grains and by increasing the actively transforming fraction.

Figures 4.3a-c show that, in contrast to previous suggestions^{38,39}, the transformation rate during discharge from Li-poor heterosite to Li-rich triphylite appears to be larger. Whether this will result in a faster discharge also depends in the asymmetry of the charge transfer and of the Li-ion transport through the electrolyte. The cycling-rate dependent transformation times may be explained by either a charge transfer dependence, i.e. Butler-Volmer, or a different transformation mechanism when the rate increases, allowing for much higher local current densities and larger actively transforming fractions, as will be discussed below. A surprising observation is that a significant fraction of the (200) LFP and (200) FP reflections during C/5 (dis)charge appear as streaks as illustrated by the reflections in Figure 4.5a-c, rather than symmetric peaks as shown in Figure 4.2.

The considerable one dimensional broadening (the instrumental resolution is about 2-3 pixels) infers platelet shaped domains of both FP and LFP, where the plate thickness is inversely proportional to the length of the streaks⁴⁰ (see Analytical methods). For the observed streaks this results in a distribution in the plate thickness with an average value of approximately 37 nm at C/5 (see Figure 4.6). This is considerably smaller than the pristine particle size (140 nm). The dimensions in the plate direction must be closer to the pristine particle size given the absence of broadening in these directions. It should be realized that in the present measurements streaks are only observable for the platelet domains that are aligned with the rotation axis ω ⁴⁰, and as a consequence the number of platelet domains, shown in Figure 4.3d-f, is significantly underestimated.

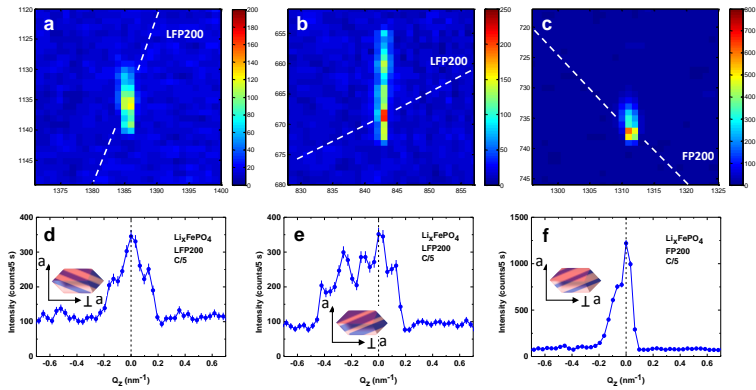


Figure 4.5. (a-c) For the slow C/5 charge rate vertical streaks are observed for the (200) reflections of both the transforming LFP (a,b) and forming FP (c) phases. The horizontal and vertical axis of the 2D diffraction patterns are the detector positions. The dashed line indicates the (200) powder diffraction ring. (d-f) Distribution in intensity of the reflections (a,b) as a function of the vertical wave vector transfer ΔQ_z with respect to the central value. The position of the streak on the (200) diffraction ring, expressed in the azimuth angle η , defines the relative orientation of the normal of the platelet shaped domain with respect to the a -axis, and the broadening in the z -direction the thickness of the platelet domains for the streaks shown leading to: (a) $\eta = 70^\circ$, $\Delta = 20$ nm, (b) $\eta = 209^\circ$, $\Delta = 10$ nm, (c) $\eta = 132^\circ$, $\Delta = 43$ nm. This leads to the shown proposed internal two phase FP/LFP morphology.

The position of the streaks on the (200) diffraction ring (characterized by the azimuth angle η indicated in Figure 4.2) in combination with the streak orientation allows us to determine the crystallographic orientation of the platelet shaped domains in the LiFePO_4 grains (see Analytical method). At C/5 the distribution in η for all observed streaks (Figure 4.6) exhibits broad maxima from $\eta \approx 60^\circ$ to $\eta \approx 135^\circ$ and $\eta \approx 240^\circ$ to $\eta \approx 300^\circ$, indicating a range of preferred orientations of the platelet domains having their normal under an angle in the range of 0° - 60° relative to the crystallographic a -axis.

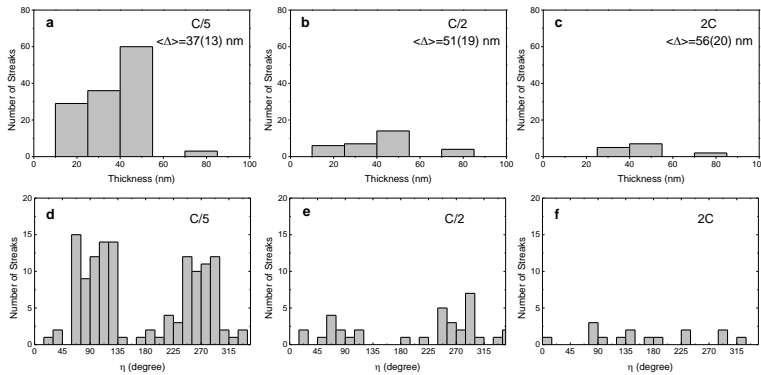


Figure 4.6. (a-c) Distribution of the platelet thickness deduced from observed streak length for different electrochemical (dis)charge rates, where $\langle \Delta \rangle$ represents the average platelet thickness. (d-f) Distribution of the azimuth angle η of the streaks on the diffraction rings for different electrochemical (dis)charge rates.

Although the present results only provide the relative crystallographic orientation of the plane normal with respect to the a -axis, the emerging phase morphology, as sketched in Figure 4.5(d-f), is consistent with a mixture of the two morphologies predicted by Cogswell et al.¹² by the minimization of the coherency strain between the coexisting phases, (1) the striped morphology with interfaces in the (101) direction (consistent with $\eta \approx 60^\circ$, 120° , 240° and 300°) obtained for coherent FP/LFP interfaces by and (2) the striped morphology with interfaces in the (100) direction (consistent with $\eta \approx 90^\circ$ and 270°) due to the loss of coherence in the (001) direction. This indicates that in these 140 nm particles a distribution exists of FP/LFP interfaces ranging from coherent to partially coherent, to complete loss of coherence in the (001) direction. Also the length scale for the platelet domain separation, or average platelet domain thickness, 37 nm at C/5 (see Figure 4.6) is in good agreement with phase field modelling¹² and TEM observations^{29,41}. The complete loss of coherence potentially leads to cracks in the (100) direction which is consistent with observations in micron sized LiFePO_4 grains²⁹, indicating that this microscopic domain behaviour plays a role even in these relatively small particle sizes most likely decreasing their cycle life.

Coexisting phase morphologies are predicted for single grains¹² and are suppressed by taking into account the coherency strain in multiple grain phase-field models that allow inter-particle charge transport²⁵. It should be noted that phase field modelling does predict mosaic instabilities, causing a phase coexistence to occur locally⁴². However throughout the electrodes coexisting phases are penalised by the coherent strain energy and this leads to the overall prediction of a mosaic phase transformation²⁵.

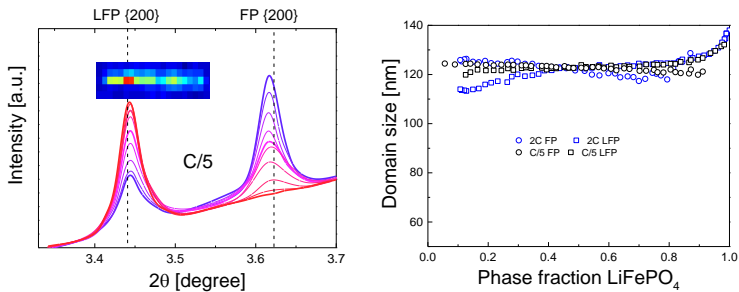


Figure 4.7. Left: In-situ powder X-ray diffraction during C/5 charging subsequent after the micro beam diffraction experiment (same cell, same geometry, larger beam size, see ref. [1] for details). The streaks that appear during C/5 charging lead to an anisotropic broadening that is generally not observable, as it disappears in the background. Right: The evolution of C/5 and 2C broadening [1].

However, the streaked reflections unambiguously represent particles having an internal structure with coexisting FP and LFP phases during C/5 (dis)charge. In combination with the slow transformation rate of individual particles the internal phase structure observed at present this exposes a very different picture from the particle-by-particle, or mosaic, phase transformation mechanism, which is generally assumed to occur in these relatively small LiFePO₄ grains at low (dis)charge rates^{14,17-20}.

At first glance, it appears surprising that the internal phase structure sketched in Figure 4.5(d-f), resulting from the appearance of streaks, is not observed by previous studies. However, only few of these studies operate under realistic in-situ conditions and powder diffraction is much less sensitive to the 1-D character of the domains. This is illustrated by the powder X-ray data obtained from the same electrodes that exhibit streaks under micro-beam conditions, which does

not show obvious broadening under powder diffraction conditions (using a larger beam)⁹, as shown in Figure 4.7. This is consistent with the absence of a significant peak broadening in earlier XRD studies that initiated the particle-by-particle transformation picture in LiFePO_4 .¹⁷ The limited length scale and the anisotropic nature of the domains occurring in only a fraction of the grains (less at lower (dis)charge rates) also appears to mask the observation of the internal domain structure for the recently reported X-ray microscopy^{14,20} and TEM studies^{18,19}. The present observations of the internal platelet domain structure in individual LiFePO_4 particles has been made possible by micro-focus hard X-ray diffraction because a statistical ensemble of crystallites could be monitored under in-situ conditions.

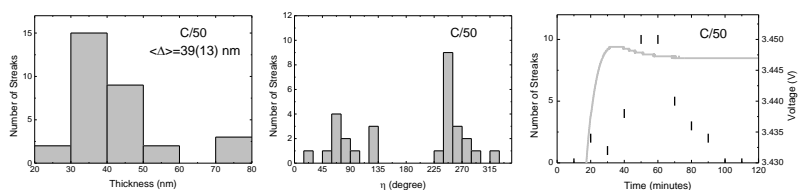


Figure 4.8. Left: Distribution of thickness of the platelets during the partial C/50 charge. Middle: Distribution in the azimuth angle η during the partial C/50 charge. Right: Number of streaks versus time including the voltage evolution during the partial C/50 charge.

In order to check the stability of the internal domain structure at even lower rates, a partial C/50 charge was conducted, also resulting in the appearance of streaked reflections as shown in Figure 4.8. At C/50 both the average platelet thickness and the distribution in the azimuth angle η are comparable to C/5 (dis)charge rate, demonstrating a comparable internal platelet domain structure, see Figure 4.6 and 4.8. The appearance of streaks during C/50 charging indicates that, even at these low rates, the internal domain structure does not transform to what should be expected to be the lower energy configuration for a multi particle ensemble where each particle has a single phase^{12,21,25,43}, avoiding the coherency strains associated with the internal interfaces^{12,21,25,37}. Possibly, this is related to the poor kinetics of the interfaces related to the associated elastic energy³¹.

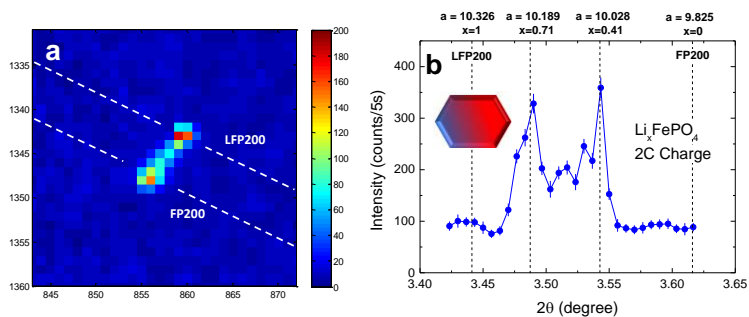


Figure 4.9. (a) (200) reflection at 2C charging rate showing coexistence of the LFP and FP phases within a single grain. The dashed lines indicate the powder rings for the (200) reflections of the LFP and FP phases, indicated as LFP200 and FP200, respectively. (b) The corresponding line scan is shown as function of the scattering angle 2θ . The maximum intensity is observed at scattering angles corresponding to $a = 10.180 \text{ \AA}$ ($x = 0.71$) for the LFP phase and $a = 10.028 \text{ \AA}$ ($x = 0.42$) for the FP phase. For both phases the a -axis is closely aligned indicating a diffuse coherent interface.

Drastic changes set in when the cycling rate is increased from C/50 and C/5 to C/2 and 2C causing a decrease in the relative number of streaked reflections and a gradual narrowing of the streaks. This translates into a decrease in number of platelet domains, as illustrated by the platelet domain statistics in Figures 4.3d-f, and an average increase in platelet domain thickness (see Figure 4.6) upon increasing the current. Figure 4.9 shows the striking appearance of a double peaked reflection at 2C charging rate. It provides direct evidence of a diffuse interface, and phase compositions far from their equilibrium values, within a single grain. The LFP (200) and FP (200) reflections can still be distinguished in Figure 4.9, resulting in strongly deviating a -axis lattice parameters (compared to the end-member values), which implies Li-compositions far away from the equilibrium compositions. The appreciable intensity between the two reflections indicates a continuous distribution of intermediate compositions, reflecting a diffuse interface over the full length scale of the 140 nm grain. This provides unique insight in the internal phase structure in a single grain at fast cycling,

indicating that the recently observed unstable intermediate compositions^{9,10} can occur within a single grain, as proposed by Zhang et al.⁹, Liu et al.¹⁰ and Oriasa et al.⁴⁴, and as predicted by phase field modelling¹².

The disappearance of the well-defined anisotropic internal domain structure when the rate increases from C/5 up to 2C in (Figure 4.6 d-f) goes along with a decrease in the average transformation time (Figure 4.4). This indicates that the platelet-shaped domain structure, with well-defined phase boundaries, may be the origin of the relatively long transformation times. In contrast, the more diffuse interfaces, first experimentally suggested by powder diffraction¹⁰ and at present observed directly, driven by higher overpotentials as predicted by phase field modelling¹¹, allow for a much faster transformation and therefore higher current densities, explaining the high rate performance of LiFePO_4 .

4.5 Conclusions

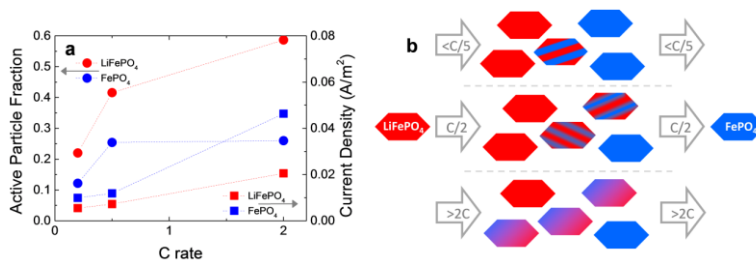


Figure 4.10. (a) Active fraction and current density of the particles resulting from the average transformation times. (b): Sketch of the rate-dependent transformation upon charge as follows from the micro-beam diffraction experiments (similar upon discharge only with a smaller active particle fraction, see (a)).

The present micro-beam X-ray diffraction results reveal for the first time the phase transformation in a large number (≈ 150) of individual electrode particles under realistic operando conditions, bringing forward a new fundamental insight in the rate-dependent phase transformations taking place in LiFePO₄ electrodes. As schematically shown in Figure 4.10b, at low (dis)charge rates the streaked reflections reveal that the transformation occurs concurrently in a large fraction of the grains and that it proceeds via the phase coexistence of thin platelet FP and LFP domains in individual grains. The distribution in relative orientations of the interface with respect to the a -axis, between the (101) and (100) planes, indicates the presence of coherent interfaces, as well interfaces with partial or complete loss in coherency in the (001) direction. In combination with the slow transformation rate of individual grains, reported for the first time, gives a very different mechanistic picture compared to the particle-by-particle, or mosaic, transformation that is commonly assumed to occur at relatively low (dis)charge rates^{14,17-20}.

The results indicate that the reaction kinetics observed here at low rates, is much slower than previously assumed¹⁷ and predicted²⁵. Even at C/50 rates the internal

platelet domain structure remains. The well-defined internal domain structure may be responsible for the observed slow transformation rates for individual grains at low (dis)charge rates, possibly due to pinning of the domain walls on defects created by the loss in coherency. Another explanation for the slow transformation kinetics may be a very slow charge transfer reaction. Bazant and co-workers⁴⁵ reported an exchange current density of about 10^{-4} A/m², smaller, but not very different from the order of magnitude reported at C/5 in Figure 4.10a. Such slow charge transfer kinetics would effectively freeze the internal domain structure. The presence of (100) interfaces indicates the loss in interface coherency, potentially leading to mechanical failure that reduces the cycle life, even for these relatively small 140 nm LiFePO₄ grains. Increasing the (dis)charge rate suppresses the formation of sharp interfaces, as demonstrated by the vanishing streaked reflections, which represent the platelet-shaped domains. The broad diffuse interface with intermediate compositions, at present observed in single particles, is expected to reflect a larger domain wall mobility due to less concentrated coherency strains making pinning on defects less likely, providing a possible explanation for the faster transformation times observed at present and the high intrinsic rate performance of LiFePO₄. This would imply that the observed transformation rates of individual grains depends on the presence of defects, the creation of which should be avoided by fast cycling and or by tailoring the particle size and shape to minimize coherency strain effects, thereby preventing the formation of defects. On the other hand if the charge transfer kinetics is rate limiting, this may potentially be improved by surface coatings that allow faster charge transfer.

Measuring the transformation process of individual LiFePO₄ particles allows for the first time quantification of local current densities in Li-ion battery electrodes under realistic (dis)charge conditions, as shown in Figure 4.10a. The present values are significantly larger compared to what is typically obtained when assuming that all electrode active material participates⁴⁶ and significantly smaller when assuming a particle-by-particle dominated mechanism¹⁴. The (dis)charge rate dependence of the local current density (shown in Figure 4.10a) which was derived from the average transformation times of individual grains is a crucial

parameter for electrode design that can help to prevent the occurrence of hotspots and fractures in electrodes^{15,16}. The increase in the local current density is a direct consequence of the faster transformation of individual particles upon increasing the (dis)charge rate. In combination with the increasing fraction of actively transforming particles, in qualitative agreement with recent findings¹⁴, the faster transformation mechanism is responsible for supplying the larger currents when increasing the (dis)charge rates.

The dynamically induced diffuse interfaces at high (dis)charge rates means that the build-up of local of the coherent lattice strain at the sharp phase boundaries is avoided. This is expected to prevent the formation of cracks at high (dis)charge rates, counter intuitively predicting that the LiFePO_4 material should show a longer cycle life time when cycled at higher rates. Possibly, for LiFePO_4 particles, a reduced size of the order of the observed platelet domains, will not permit the existence of well-defined phase boundaries, thereby preventing potential crack forming and extending the cycle life also at low (dis)charge rates.

Given the general nature of the phase transition behaviour observed here, an interesting future question is how these findings will translate towards other phase separating insertion materials, a group of materials that are highly relevant for energy storage. The results illustrate the unique abilities of micro-beam diffraction revealing the fundamental phase transition processes in electrodes under realistic operando conditions and providing guidance for future battery design.

References

- (1) Padhi, A. K.; Nanjundaswamy, K. S.; Goodenough, J. B. *J. Electrochem. Soc.* **1997**, *144*, 1188.
- (2) Malik, R.; Abdellahi, A.; Ceder, G. *Journal of the Electrochemical Society* **2013**, *160*, A3179.
- (3) Ravet, N. e. a. In *Electrochemical Society Fall Meeting, Honolulu, Hawaii (Electrochemical Society, Pennington, New Jersey, 1999)* 1999, p 127.
- (4) Huang, H.; Yin, S. C.; Nazar, L. F. *Electrochemical and Solid State Letters* **2001**, *4*, A170.
- (5) Herle, P. S.; Ellis, B.; Coombs, N.; Nazar, L. F. *Nat. Mater.* **2004**, *3*, 147.
- (6) Gaberscek, M.; Dominko, R.; Jamnik, J. *Electrochemistry Communications* **2007**, *9*, 2778.
- (7) Wang, Y.; Wang, Y.; Hosono, E.; Wang, K.; Zhou, H. *Angewandte Chemie-International Edition* **2008**, *47*, 7461.
- (8) Yamada, A.; Koizumi, H.; Nishimura, S. I.; Sonoyama, N.; Kanno, R.; Yonemura, M.; Nakamura, T.; Kobayashi, Y. *Nat. Mater.* **2006**, *5*, 357.
- (9) Zhang, X.; van Hulzen, M.; Singh, D. P.; Brownrigg, A.; Wright, J. P.; van Dijk, N. H.; Wagemaker, M. *Nano Letters* **2014**, *14*, 2279.
- (10) Liu, H.; Strobridge, F. C.; Borkiewicz, O. J.; Wiaderek, K. M.; Chapman, K. W.; Chupas, P. J.; Grey, C. P. *Science* **2014**, *344*.
- (11) Bai, P.; Cogswell, D. A.; Bazant, M. Z. *Nano Letters* **2011**, *11*, 4890.
- (12) Cogswell, D. A.; Bazant, M. Z. *ACS Nano* **2012**, *6*, 2215.
- (13) Bazant, M. Z. *Accounts of Chemical Research* **2013**, *46*, 1144.
- (14) Li, Y.; El Gabaly, F.; Ferguson, T. R.; Smith, R. B.; Bartelt, N. C.; Sugar, J. D.; Fenton, K. R.; Cogswell, D. A.; Kilcoyne, A. L. D.; Tyliszczak, T.; Bazant, M. Z.; Chueh, W. C. *Nature materials* **2014**, *13*, 1149.
- (15) Woodford, W. H.; Chiang, Y.-M.; Carter, W. C. *Journal of the Electrochemical Society* **2010**, *157*, A1052.
- (16) Christensen, J.; Newman, J. *Journal of Solid State Electrochemistry* **2006**, *10*, 293

- (17) Delmas, C.; Maccario, M.; Croguennec, L.; Le Cras, F.; Weill, F. *Nature Materials* **2008**, *7*, 665.
- (18) Brunetti, G.; Robert, D.; Bayle-Guillemaud, P.; Rouviere, J. L.; Rauch, E. F.; Martin, J. F.; Colin, J. F.; Bertin, F.; Cayron, C. *Chemistry of Materials* **2011**, *23*, 4515.
- (19) Sugar, J. D.; El Gabaly, F.; Chueh, W. C.; Fenton, K. R.; Tyliczszak, T.; Kotula, P. G.; Bartelt, N. C. *Journal of Power Sources* **2014**, *246*, 512.
- (20) Chueh, W. C.; El Gabaly, F.; Sugar, J. D.; Bartelt, N. C.; McDaniel, A. H.; Fenton, K. R.; Zavadil, K. R.; Tyliczszak, T.; Lai, W.; McCarty, K. F. *Nano Letters* **2013**, *13*, 866.
- (21) Dreyer, W.; Jamnik, J.; Guhlke, C.; Huth, R.; Moskon, J.; Gaberscek, M. *Nature Materials* **2010**, *9*, 448.
- (22) Sasaki, T.; Ukyo, Y.; Novak, P. *Nature Materials* **2013**, *12*, 569.
- (23) Dreyer, W.; Guhlke, C.; Herrmann, M. *Continuum Mechanics and Thermodynamics*, *23*, 211.
- (24) Ferguson, T. R.; Bazant, M. Z. *Electrochimica Acta* **2014**, *146*, 89.
- (25) Ferguson, T. R.; Bazant, M. Z. *Journal of the Electrochemical Society* **2012**, *159*, A1967.
- (26) Sharma, N.; Guo, X.; Du, G.; Guo, Z.; Wang, J.; Wang, Z.; Peterson, V. K. *Journal of the American Chemical Society* **2012**, *134*, 7867.
- (27) Laffont, L.; Delacourt, C.; Gibot, P.; Wu, M. Y.; Kooyman, P.; Masquelier, C.; Tarascon, J. M. *Chemistry of Materials* **2006**, *18*, 5520.
- (28) Gu, L.; Zhu, C. B.; Li, H.; Yu, Y.; Li, C. L.; Tsukimoto, S.; Maier, J.; Ikuhara, Y. *Journal of the American Chemical Society*, *133*, 4661.
- (29) Chen, G. Y.; Song, X. Y.; Richardson, T. J. *Electrochemical and Solid State Letters* **2006**, *9*, A295.
- (30) Holtz, M. E.; Yu, Y.; Gunceler, D.; Gao, J.; Sundararaman, R.; Schwarz, K. A.; Arias, T. A.; Abruna, H. D.; Muller, D. A. *Nano Letters* **2014**, *14*, 1453.
- (31) Ohmer, N.; Fenk, B.; Samuelis, D.; Chen, C.-C.; Maier, J.; Weigand, M.; Goering, E.; Schuetz, G. *Nature Communications* **2015**, *6*.

- (32) Lucas, I. T.; McLeod, A. S.; Syzdek, J. S.; Middlemiss, D. S.; Grey, C. P.; Basov, D. N.; Kostecki, R. *Nano Letters* **2015**, *15*, 1.
- (33) Sivia, D. S. *Elementary scattering theory for X-ray and neutron user*; Oxford University Press Oxford, 2011.
- (34) Feigin, L. A.; Svergun, D. I. *Structure analysis by small-angle X-ray and neutron scattering*; Plenum Press New York, 1987.
- (35) Takano, Y.; Liou, K. N.; Yang, P. J. *Quantitative Spectroscopy Radiative Transfer* **2012**, *113*, 1836.
- (36) Als-Nielsen, J.; McMorrow, D. *Elements of Modern X-ray Physics*; Wiley: West Sussex, 2001.
- (37) Warren, B. E.; Dover Publications: New York, 1990.
- (38) Shin, H. C.; Chung, K. Y.; Min, W. S.; Byun, D. J.; Jang, H.; Cho, B. W. *Electrochemistry Communications* **2008**, *10*, 536.
- (39) Munakata, H.; Takemura, B.; Saito, T.; Kanamura, K. *Journal of Power Sources* **2012**, *217*, 444.
- (40) De Geuser, F.; Bley, F.; Deschamps, A. *Journal of Applied Crystallography* **2012**, *45*, 1208.
- (41) Ramana, C. V.; Mauger, A.; Gendron, F.; Julien, C. M.; Zaghbi, K. *Journal of Power Sources* **2009**, *187*, 555.
- (42) Orvananos, B.; Ferguson, T. R.; Yu, H. C.; Bazant, M. Z.; Thornton, K. J. *Electrochem. Soc.* **2014**, *161*, A535.
- (43) Wagemaker, M.; Borghols, W. J. H.; Mulder, F. M. *J. Am. Chem. Soc.* **2007**, *129*, 4323.
- (44) Oriksa, Y.; al., e. *Chem. Mater.* **2013**, *25*, 1032.
- (45) Bai, P.; Bazant, M. Z. *Nature Communications* **2014**, *5*.
- (46) Srinivasan, V.; Newman, J. *Journal of the Electrochemical Society* **2004**, *151*, A1517.

Chapter 5

Direct Observation of Li-ion transport in electrode under non-equilibrium condition using Neutron Depth Profiling

Based on the paper : '*Direct Observation of Li-ion transport in electrodes under non-equilibrium conditions using Neutron Depth Profiling*'

Xiaoyu Zhang, Tomas W. Verhallen, Freek Labohm and Marnix Wagemaker*, **Adv. Energy Mater.**, 5, 1500498-1500505 (2015)

Abstract

One of the key challenges of Li-ion electrodes is enhancement of (dis)charge rates. This is severely hindered by the absence of a technique that allows direct and non-destructive observation of lithium ions in operating batteries. Direct observation of the Li-ion concentration profiles using operando Neutron Depth Profiling reveals that the rate limiting step is not only dependent on the electrode morphology but also on the cycling rate itself. In the LiFePO₄ electrodes phase nucleation limits the charge transport at the lowest cycling rates, whereas electronic conductivity is rate limiting at intermediate rates, and only at the highest rates ionic transport through the electrodes is rate limiting. These novel insights in electrode kinetics are imperative for the improvement of Li-ion batteries and shows the large value of in-situ NDP in Li-ion battery research and development.

5.1 Introduction

Development of high energy density Li-ion batteries is essential for the realization of electric and plug-in hybrid vehicles. Aiming at performance improvement, considerable efforts are made to understand the fundamental mechanisms that limit the (dis)charge rates of Li-ion battery materials^{1,2}. During charge Li-ions are driven from the positive electrode to the anode by an externally applied potential. The larger lithium chemical potential in the negative electrode is the driving force for the exothermic discharge reaction due to which the Li-ions migrate back to the positive electrode. The internal resistance of the battery results in a voltage polarization, or overpotential, that scales with the (dis)charge current, leading to higher external potentials during charge and lower during discharge, reducing the energy efficiency of the battery. Because the internal resistance of the battery is dominated by the resistance of the rate limiting step, higher power densities, and hence shorter (dis)charge times, require improvement of the rate limiting charge transport step. Therefore, knowledge of what charge transport phenomenon is rate limiting under what conditions is paramount for the design of future Li-ion batteries.

Possible contributions to the internal resistance include (1) the electronic wiring, (the contact between the active electrode material and current collector), (2) the ionic network formed by the liquid electrolyte in the pores of the composite electrodes connecting the active electrode material and the electrolyte, (3) the charge transfer reaction between the liquid electrolyte and the active electrode material and (4) the solid state transport and phase nucleation/transformation kinetics within the active electrode material.

Many processes have been reported to improve Li-ion battery (dis)charge kinetics, each improving one or more of the described aspects 1-4, illustrating the complexity and the lack of agreement concerning the rate limiting step. This is best illustrated by LiFePO_4 , an important electrode material proposed by Padhi et al.³ in 1997, and an intensively studied, well established model system up to date. (a) For LiFePO_4 the initial hurdle of poor intrinsic electronic and solid state ionic

conduction were overcome by reducing the particle size in combination with carbon or metallic conducting coatings⁴⁻⁶. In addition to the trivial decrease in the solid state diffusion distance, particle size reduction towards the nano range has also shown to impact the kinetic and thermodynamic properties of electrode materials⁷⁻¹⁰. For instance, the nucleation barrier for the first order phase transition in LiFePO_4 is predicted to be smaller for smaller particles¹¹. Also the equilibrium potential depends on the particle size, which is predicted to be the consequence of the surface energy which has more impact in smaller particles^{7,12-14}. In LiFePO_4 this results in a larger equilibrium voltage in smaller LiFePO_4 particles^{12,15} which explains the spontaneous, without an externally applied potential, Li-ion transport from small to large LiFePO_4 particles¹⁶. (b) First order phase transitions are generally thought to result in poor kinetics as compared to solid solution reactions. The observation that the first order phase transition can be bypassed in LiFePO_4 at high (dis)charge rates^{17,18} driven by the overpotential¹⁹⁻²¹, is also considered to be responsible for the high (dis)charge rates that can be achieved.¹⁷⁻²¹ (c) surface diffusion on the LiFePO_4 particles appears to play a role as very fast (dis)charge rates were achieved by the addition of an ionic conducting phase at the LiFePO_4 surface²². (d) In many studies it has been recognized that for higher rates the ionic transport through the porous electrode structure is rate limiting²³⁻²⁹. This is consistent with the direct observation that the electrode capacity decreases with increasing thickness at the same rate and loading density^{23,30}. Over the years various modelling approaches have been describing the complex phenomena that play a role, starting with the ion and electron transport and charge transfer through the porous electrode matrix^{1,31}, solid solutions and distributed ohmic drop in the LiFePO_4 material³² and the complex phase behavior in the solid state LiFePO_4 ^{11,33,34} material. The diverse results, caused by the large amount of parameters involved, have to date made it impossible to unambiguously determine the rate limiting charge transport mechanism under various conditions, which is crucial for improving battery performance.

Depending on which charge transport mechanism is rate limiting distinctly different Li-ion distributions are expected throughout the electrodes

perpendicular to the current collector. Therefore, direct observation of the Li-ion distribution depending on the electrochemical conditions and depending on the structure and morphology of the electrodes would give direct mechanistic insight into kinetic and thermodynamic processes in batteries, currently only partially available. For this reason experimental methods are required that probe the distribution of Li-ions directly under nondestructive in operando conditions. This has driven the development of in-situ techniques such as TEM³⁵, in-situ NMR^{36,37}, neutron imaging³⁸⁻⁴⁰ and Neutron Depth Profiling (NDP)⁴¹⁻⁴⁶.

Neutron Depth Profiling (NDP) offers the possibility to directly see lithium nuclei through the capture reaction of neutrons with the ⁶Li isotope to form an α -particle (⁴He) and a triton ion (³H) according to



The energy that is generated by the reaction is distributed between the two particles according to conservation of energy and momentum. The ⁴He and ³H particle travel through the surrounding material during which they lose energy. By measuring this energy loss the depth at which the ⁶Li atom was located can be determined. This allows to reconstruct a Li-atom density profile as a function of depth, shown in Figure 5.5, without significantly influencing the Li concentration due to the low neutron flux making this a non-destructive technique.

The history of the using of Neutron capture reactions can be traced back to 1972, Ziegler et al. first used this reaction to determine the concentration of Boron impurities in silicon wafers⁴⁷. After that, Downing et al.⁴⁸ and Biersack et al.⁴⁹ used this method to measure other isotopes, including ⁶Li. This initiated Whitney et al.⁵⁰ and Nagoure et al.⁵¹⁻⁵³ to use NDP to measure post mortem Lithium concentration profiles in the near surface area of commercial Li-ion batteries resulting in more insight in battery degradation after many charge/discharge cycles. Oudenhoven et al.⁵⁴ performed the first in-situ NDP study on thin film solid state micro-batteries, demonstrating the direct observation of the evolution of the lithium concentration profile over time under different electrochemical conditions. The challenge of applying in-situ NDP to conventional Li-ion batteries is the limited travel length of the charged capture reaction products through the electrode and current collector, limiting the maximum depth in the battery that

can be probed. An additional complication is that NDP experiments are typically performed under vacuum conditions, preventing parasitic energy absorption of the capture reaction products in air. As a consequence of the low outside pressure the electrolyte tends to become gaseous, compromising the contact between the electrodes and the separator. Recently, Wang et al.⁴¹ and Liu et al.⁴⁶ reported on the development of in-situ NDP elegantly demonstrating the onset of lithiation in Sn electrodes and giving mechanistic insight in the process. Employing half-cells, with Kapton film windows to protect the lithiated surface of the Sn sample, Wang et al. were able to determine the Li-distribution inside the Sn quantitatively down to several micrometers and thereby enabled to study these liquid electrolyte systems with in-situ NDP. The further developed cell design by Liu et al. allowed clear observation of the Li distribution during charge and discharge of a Lithium-Tin cell, proving operando NDP as an invaluable technique for the characterization of Li-ion battery electrode materials. Recently, we reported on extending the application of in-situ NDP towards conventional Li-ion battery systems, using the Al current collector as window, allowing to probe relatively thick electrodes with liquid electrolytes⁴³⁻⁴⁵. This is another significant step forward because the developed cell allows any type of electrode coating to be analyzed with in-situ NDP.

The present communication aims at direct insight in the processes that limit the charge transport in Li-ion batteries by measuring the lithium distribution in porous LiFePO₄ electrodes, in combination with liquid electrolytes, using operando NDP under dynamic charge/discharge conditions. By varying the electrode morphology, including the electronic wiring and particle size, it is shown what process is rate limiting under what conditions, providing fundamental understanding and guidance to the development of high performance Li-ion battery electrodes.

5.2 Experimental and Analytical Method

5.2.1 Sample Preparation And Experiment Method

The cathode material was carbon coated LiFePO_4 from Phostech with an average particle size of 140 nm. LiFePO_4 cathodes were prepared through mixing a slurry of LiFePO_4 , Carbon Black (Super P), PVDF, (polyvinylidene fluoride, Solvay), with a mass ratio of 80:10:10 respectively, in NMP (N-methylpyrrolidone). The carbon rich sample was made with a mass ratio of the active material, carbon black (SuperP) and binder (PVDF) of 50:40:10. The slurries were spin coated on approximately 11.5 μm aluminum foil substrates. The bi-layered electrodes of 140 nm LiFePO_4 particles and 70 nm LiFePO_4 particles were prepared using electrospraying. In this technique a liquid electrode slurry flows from a capillary nozzle is dispersed into fine droplets by means of a high electric potential.^{61,62} By controlling the voltage the rate of deposition can be manipulated and thus the thickness of the coating. Further details can be found below in the 5.2.5. Glass fiber disks (Whatman) were used as separators and the electrolyte used was 1.0 molar LiPF_6 in EC/DMC (ethylene carbonate and dimethyl carbonate in a 1:1 ratio, Novolyte, battery grade). All the electrode were pressed before use to ensure a good contact between active material and current collector. The battery components were assembled under argon atmosphere (<0.1 ppm $\text{O}_2/\text{H}_2\text{O}$) in a specially designed air-tight cell where the back of the current collector is facing outside. All electrochemical tests were performed galvanostatically within a voltage window of 4.3 and 2.5 V vs Li/Li^+ using a Maccor 4000 or 4400 cycling system.

Neutron depth profiling was performed on one of the thermal neutron beam lines at the Reactor Institute Delft. The NDP cell is positioned inside the vacuum chamber at an angle of 30 degrees towards the incident neutron beam and parallel to the detector. For the used current collector (10.5 μm Al) the stopping power is too large for the ^4He particles to leave the battery. As such only the energy loss of the ^3H particles is

measured with the charged particle implanted Si detector. The energy spectrum is then collected by a Multi-Channel Analyzer (MCA). Figure 5.5 shows the schematic of the in-situ NDP measurement set up. The depth calibration, relating the measured ^3H energy to the Li-ion depth position was performed using SRIM.⁶⁰

5.2.2 Depth Calibration

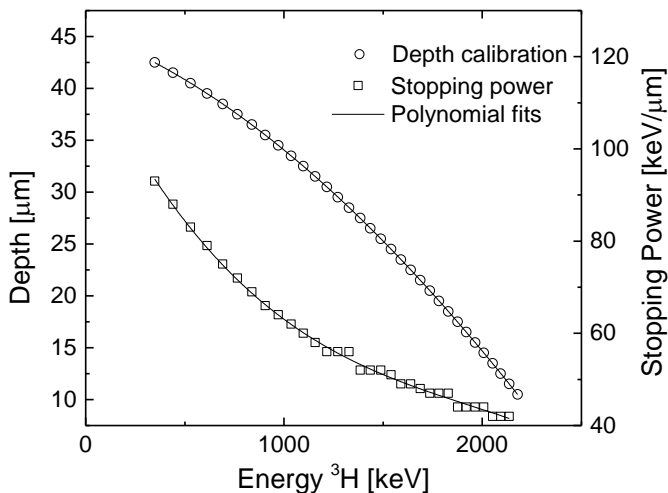


Figure 5.1. Depth and stopping power calibration curves (polynomial fits) fitted on the SRIM calculated energy loss and energy loss per μm electrode.

SRIM⁶⁰ was used to calculate the energy loss of the ^3H particles originating at different depths in the electrode. A third order polynomial was fitted on these results to yield a calibration relation between the energy of the triton ions and the depth of the capture reaction in the electrode resulting in

$$d(E) = 45.94 - 0.00828 \times E - 3.608 \cdot 10^{-6} \times E^2 - 3.276 \cdot 10^{-11} \times E^3 \quad (5-1)$$

see Figure 5.1.

5.2.3 Intensity Calibration

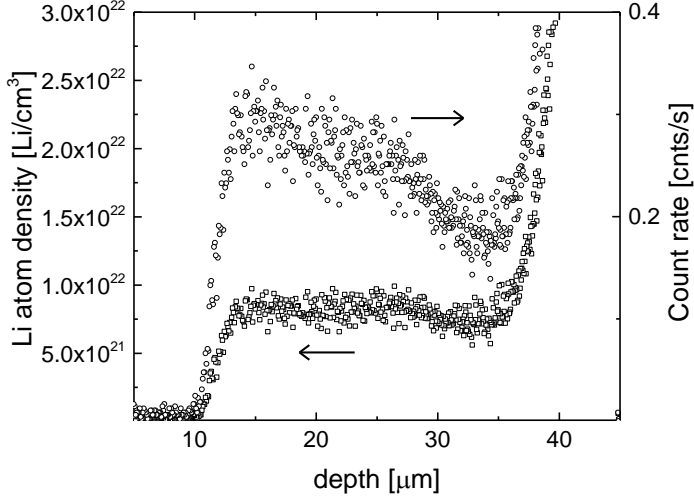


Figure 5.2. Intensity calibration of a pristine electrode (19 μm LiFePO_4 electrode on 10.5 μm Al current collector).

Normalizing the count rate on the monitor count rate corrects for any fluctuations in the incoming neutron flux. A ^{10}B containing sample with a known concentration ($c_{^{10}\text{B}} = 9.543 \times 10^{15} \text{ }^{10}\text{B}/\text{cm}^2$) was measured in the exact same geometrical settings in the in-situ electrochemical cell. This allows to determine n_{Li} [Li/cm^2] in the electrodes given the cross sections for the capture reactions of ^{10}B ($\sigma_{^{10}\text{B}} = 3837$ barn) and ^6Li ($\sigma_{^6\text{Li}} = 940$ barn) and the natural abundance of ^6Li ($A_{^6\text{Li}} = 0.075$):

$$n_{\text{Li}}[\text{Li}/\text{cm}^2] = \frac{n_{^{10}\text{B}}[\text{atoms}/\text{cm}^2] \times \sigma_{^{10}\text{B}}[\text{barn}]}{A_{^6\text{Li}} \times c_{^{10}\text{B}}[\text{cnts}/\text{s}] \times \sigma_{^6\text{Li}}[\text{barn}]} \times c_{^6\text{Li}}[\text{cnts}/\text{s}] \quad (5-2)$$

To convert towards the Li-ion density [Li/cm^3] it is necessary to correct for the energy dependent stopping power, which in combination with the constant

energy resolution of the detector (3.3 keV) results in a depth dependent depth resolution:

$$t(E)[\mu\text{m}] = \frac{3.3[\text{keV}]}{S(E)[\text{keV} / \mu\text{m}]} \quad (5-3)$$

From the depth dependent energy loss of the triton ions that was determined with SRIM the energy dependent stopping power of the electrode system (LiFePO₄ coated on 10.5 μm Al) was determined by fitting a third order polynomial on the with SRIM calculated values resulting in, see Figure 5.2.

$$S(E) = 119.94 - 0.0886 \times E + 3.824 \cdot 10^{-5} \times E^2 - 6.531 \cdot 10^{-9} \times E^3 \quad (5-4)$$

Therefore, the measured count rate, $c^6\text{Li}$ [cnts/s] can be converted directly to Li atom concentration by

$$n_{\text{Li}}[\text{Li} / \text{cm}^3] = \frac{n_{10\text{B}}[\text{atoms} / \text{cm}^2] \times \sigma_{10\text{B}}[\text{barn}] \times S(E)[\text{keV} / \text{cm}]}{A \times c_{10\text{B}}[\text{cnts} / \text{s}] \times \sigma_{6\text{Li}}[\text{barn}] \times 3.3[\text{keV}]} \times c_{6\text{Li}}[\text{cnts} / \text{s}] \quad (5-5)$$

An example of the correction is shown in Figure 5.2. The correction results in a constant Li atom density, as expected for the electrode coatings and to a Li atom density close what should be expected for the approximately 2g/cm³ coated LiFePO₄ coatings (2g/cm³ LiFePO₄ corresponds to 9.08×10²¹ Li atoms/cm³). Note that both the binder (10 wt%) and Carbon Black (10 wt%) were not considered in the depth and intensity calibration based on their relatively small stopping power and weight percentage. The decrease in Li atom density after approximately 30 μm depth corresponds to the start of the electrolyte/separator. The 1 molair LiPF₆ electrolyte corresponds to 6.022×10²⁰ Li atoms/cm³, however the large background due to gamma radiation results in a much higher count rate, increasing further at larger depth.

The ³H spectra reported in the manuscript are converted using the fully charged and fully discharged states as background and reference states. By subtracting the

fully (C/50) charged state spectrum ($\text{Li}_{x=0}\text{FePO}_4$) from all the spectra the background is eliminated and by normalizing on the fully discharged state ($\text{Li}_{x=1}\text{FePO}_4$) the average Li composition is obtained.

5.2.4 Ex-situ measurements

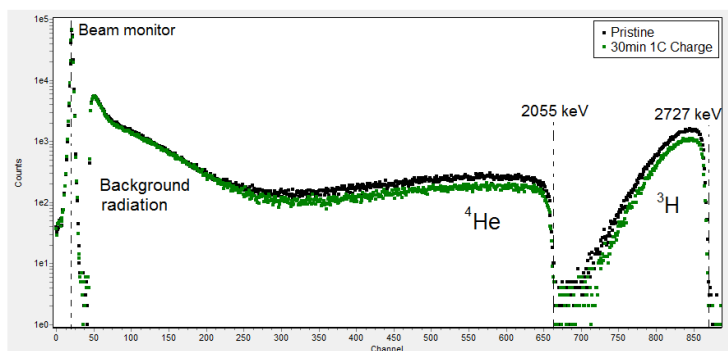


Figure 5.3. Typical ex-situ measurement, the pristine electrode is indicated by the black line, the green indicates the measurement after 30 minutes of 1C charge. All counts have been normalized to the beam monitor. The background intensity decreases with increasing energy, indicated by the channel numbers.

Figure 5.3 shows a typical ex-situ measurements. During these measurements the samples are placed with the electrode facing the detector, in contrast to the in-situ experiments, and consequently both the ^4He and ^3H particles are measured, as shown in Figure 5.3. The escape depth of the ^4He particles is limited to approximately 8 microns, it is thus not possible to determine the lithium concentration in the whole electrode based on the ^4He counts.

Depth calibration, performed as explained above, has shown that the ^3H loose approximately 700 keV in 15 microns of electrode material, and for this reason less thick electrodes were prepared to prevent the necessity to separate the ^3H and ^4He signals.

5.2.5 Electro spray electrode preparation

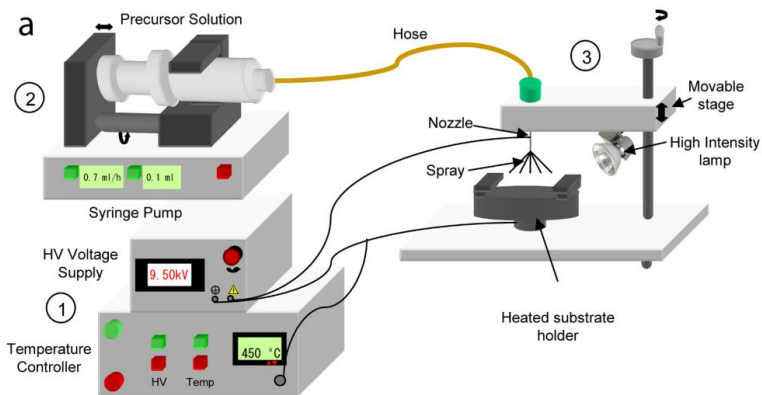


Figure 5.4. Schematic drawing of the electro spray deposition setup used for the double-layers coating⁶¹

The bi-layered electrodes of 140 nm and 70 nm LiFePO_4 particles were prepared using electro spraying the setup of which is schematically show in Figure 5.4. In this technique a liquid electrode slurry flows from a capillary nozzle is dispersed into fine droplets by means of a high electric potential^{59,61}. By controlling the voltage the rate of deposition can be manipulated and thus the thickness of the coating. Two electrodes were prepared. Geometry 1: $\approx 5 \mu\text{m}$ electrode of 70 nm LiFePO_4 particles on the current collector side followed by a $\approx 5 \mu\text{m}$ electrode of 140 nm LiFePO_4 particles at the electrolyte side and Geometry 2 vice versa.

5.3 Results and Discussion

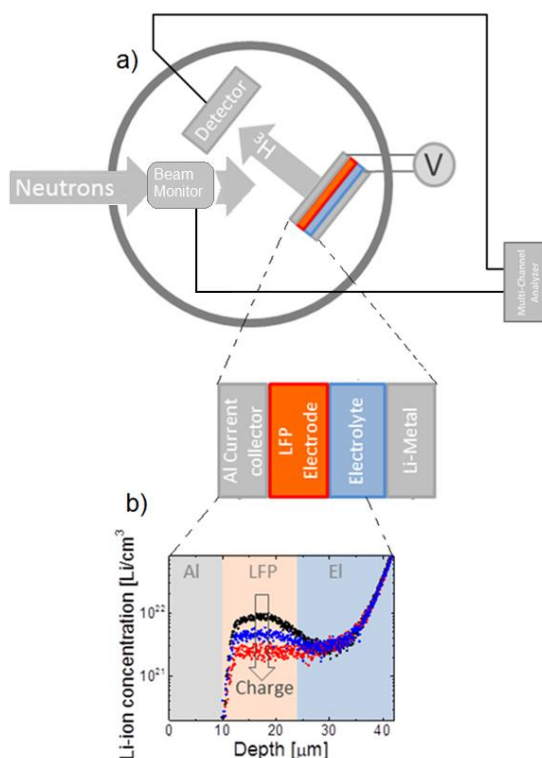


Figure 5.5. (a) The Schematic NDP setup at the Reactor Institute Delft. (b) Depth calibrated lithium intensity plot indicating the layered battery geometry

Figure 5.5 shows the schematic setup of the operando NDP experiments. The designed NDP cell is exposed to the thermal neutron beam at the LiFePO_4 electrode side inside the vacuum chamber. The capture reaction of the incoming thermal neutrons with the ${}^6\text{Li}$ -ions forms an α -particle (${}^4\text{He}$) and a triton ion (${}^3\text{H}$) with 2055 keV and 2727 keV respectively. Because of the larger ${}^4\text{He}$ stopping power in the electrode and current collector and the lower initial kinetic energy, ${}^4\text{He}$ particles are not able to penetrate through the current collector, and are

consequently not detected. As a consequence the results in this communication are based on ^3H spectra. The depth calibrated spectra in Figure 5.5b demonstrate that the thickness of the aluminum current collector is approximately $10\ \mu\text{m}$ and that this specific LiFePO_4 electrode is approximately $12\ \mu\text{m}$ thick. This is relatively thin for Li-ion electrodes but it has the advantage for the NDP experiments that complete electrode is probed. The kinetic energy of the ^3H particles limits the escape depth through the layered battery geometry to roughly $40\ \mu\text{m}$. Consequently, ^3H originating from the Li-metal negative electrode and large part of the electrolyte/separator are not able to reach the detector. The calibrated Li-density measured with NDP indicates that these electrodes are relatively homogeneous in density, and is consistent with the electrode density ($2\ \text{g}/\text{cm}^3$) measured via the electrode loading and thickness (see experimental and analytical method part). The lithium concentration in the LiFePO_4 active material ($13.8 \times 10^{21}\ \text{Li}/\text{cm}^3$ or 22.8 molar) is much larger compared to that in the electrolyte ($0.6 \times 10^{21}\ \text{Li}/\text{cm}^3$ or 1.0 molar) in the pores of the positive electrode. For the present electrode coating density, $2.0\ \text{g}/\text{cm}^3$ (34% porous), almost 98% of the signal is due to lithium in the active LiFePO_4 material. Therefore, the Li-ion depth profiles in this work are only due to the Li-ions in the active material, and hence the measured Li-concentration can be expressed in the average local Li-composition in the active material. Note that all Li-ion depth profiles will be consistently plotted with the interface between the aluminum current collector and the LiFePO_4 electrode at the left side (zero depth) and the interface between the LiFePO_4 electrode and the electrolyte at the right side.

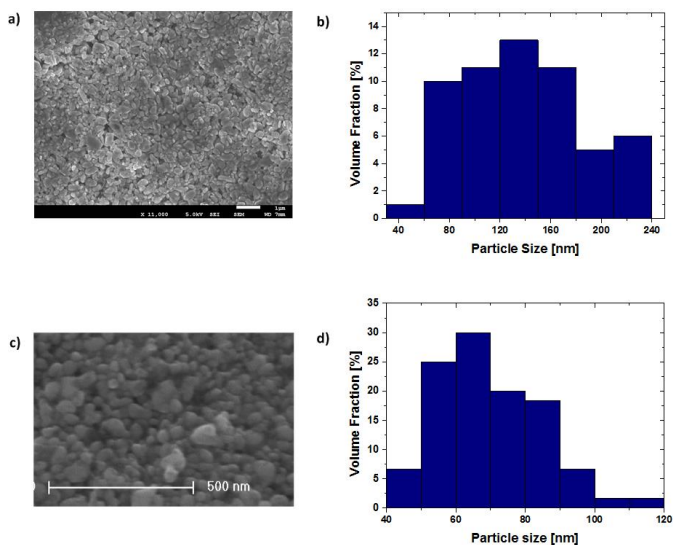


Figure 5.6. SEM figures and size distribution of LiFePO₄ for (a-b) 140 nm and (c-d) 70 nm powders. A standard deviation of 56 nm and respectively 11 nm was found from analysis of the SEM figures.

The in-situ evolution of the Li-ion concentration as a function of depth and time in the LiFePO₄ electrode (140 ± 56 nm particle size, see Figure 5.6) during a full C/50 charge-discharge cycle is shown in Figure 5.7.b. The ³H counts were converted to Li-ion concentration by subtracting the fully (C/50) charged state spectrum (Li_{x=0}FePO₄) from all the spectra to eliminate the background and by normalizing on the fully discharged state (Li_{x=1}FePO₄). This facilitates comparing concentrations at different depth as is illustrated in Figure 5.7.a. As a cross check the count rate was also corrected for the experimental geometry using a calibration sample and the stopping power of the current collector and electrode resulting in the same maximum average Li-occupancy taking into account the electrode density, see experimental and analytical method part.

The in-situ evolution of the Li-ion distribution in the LiFePO₄ electrode during a C/50 charge-discharge cycle is shown in Figure 5.7.b. As expected during charging the Li-ion concentration decreases throughout the electrode and during discharge the Li-ion concentration increases again, illustrating the reversible reaction of all

the Li-ions in LiFePO_4 . Figure 5.7.a displays no significant difference between charge and discharge Li-ion concentration profiles proving the Li-ion depletion and insertion to be homogeneous both during slow charge and discharge. Using phase field modeling in combination with porous diffusion theory Ferguson et al.³⁴ predicted a sharp gradient in the Li-ion distribution in the electrode material at low rates ($C/30$) assuming no particle size distribution, whereas a homogeneous distribution in the Li-ion concentration was predicted when a distribution of particle sizes was introduced⁵⁵, in agreement with the slow cycling result in Figure 5.6 for 140 ± 56 nm particles.

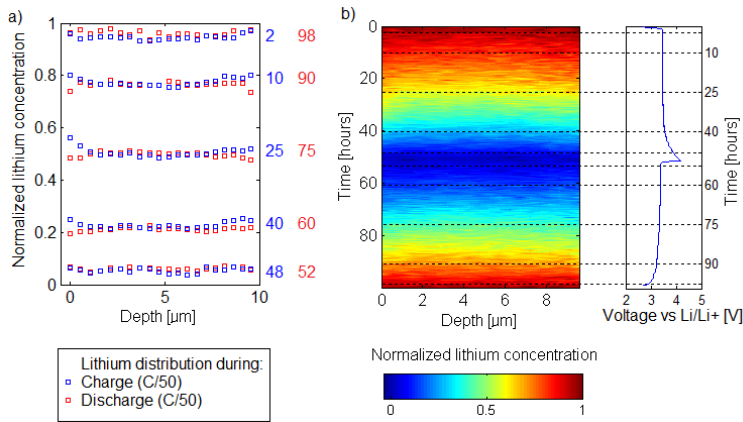


Figure 5.7. (a) Comparing the charged and discharged state at several stages during a complete $C/50$ charge discharge cycle. (b) Evolution of the lithium concentration during charge and discharge at $C/50$. The dotted lines indicate the states compared in (a). The current collector is located at the left and the electrolyte at the right.

To study the impact of particle size on the distribution of Li-ions in electrodes in detail, two double layered electrode geometries have been prepared, geometry 1 consisting of an approximately $5 \mu\text{m}$ thick layer of 70 ± 11 nm LiFePO_4 particles (see Figure.5.6) at the current collector side and an approximately $5 \mu\text{m}$ thick layer of 140 ± 56 nm particles at the electrolyte side and geometry 2 vice versa. Particle

size is known to influence the equilibrium potential^{12,56} being larger in smaller LiFePO₄ crystallites^{12,15,16} and in addition it has been predicted to influence the nucleation barrier being lower in smaller LiFePO₄ crystallites due to surface wetting¹¹. As a consequence two different situations may occur depending on the timescale of the (dis)charge experiment. (1) Given enough time the Li-ion extraction and insertion may be expected to follow the thermodynamic route in which case larger particles (140 nm) will be depleted from Li-ions first during charge (their lower equilibrium Li-ion storage potential will lead to preferential nucleation of the FePO₄ phase) and inserted first during discharge. (2) In contrast, if the nucleation kinetics are dominant in comparison to the other kinetic processes (charge transfer and ionic and electronic conduction) the FePO₄ phase will nucleate first in smaller particles (70 nm) based on their lower predicted nucleation energies¹¹.

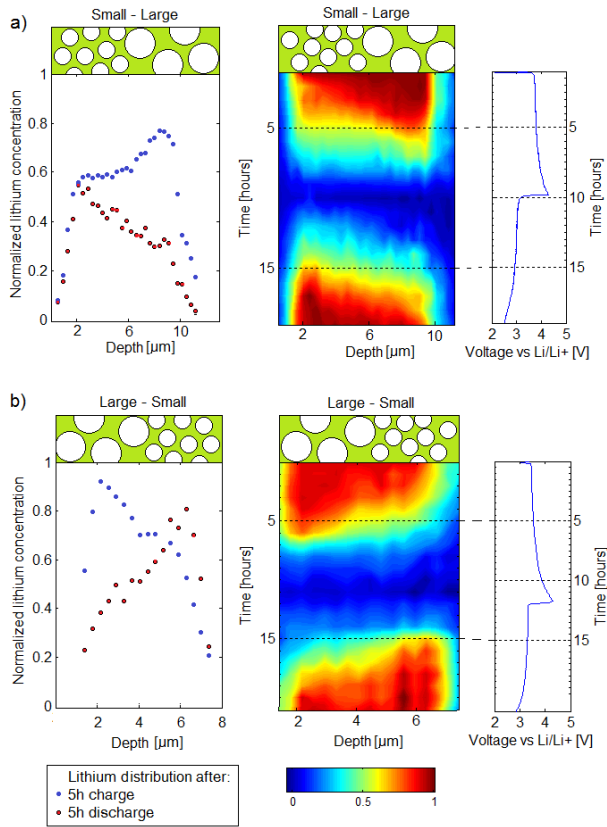


Figure 5.8. In-situ NDP spectra during C/10 cycling (a) Geometry 1; small (70 nm) particles at the current collector side and large (140 nm) particles at the electrolyte side. Left: Li-ion distribution after 5 hours of charge and discharge. Right: Evolution of the Li-ion distribution during a full charge discharge cycle. (b) Geometry 2; large (140 nm) particles at the current collector side and small (70 nm) particles at the electrolyte side. Left: Li-ion distribution after 5 hours of charge and discharge. Right: Evolution of the Li-ion distribution during a full charge discharge cycle. The current collector is located at the left and the electrolyte at the right.

The in-situ NDP during C/10 charging in Figure 5.8 shows that independent of the geometry the smaller (70 nm) particles delithiate first. Apparently, the non-equilibrium pathway is followed during charge indicating that the nucleation energy for the phase transition in the smaller LiFePO_4 particles is lower compared

to that in the larger particles, providing the first direct experimental evidence and confirming the prediction by Cogswell et al.¹¹ Figure 5.8 shows that also during discharge the smaller particles react first. In this case however, the thermodynamic route (based on the difference in Li-ion potential) and the kinetic route (based on the difference in nucleation energy) coincide, but given that on charge the lower nucleation energy of smaller particles appears to be dominant, it is likely this is also the case during discharge. The fact that particle size determines the Li-ion distribution in electrodes implies that both electronic and ionic conduction through the electrode do not play a dominant role (are not mainly responsible for the observed Li-ion gradient) up to $C/10$ in these electrode morphologies. Note that the preferential reaction of the smaller particles is the origin of the absence of a Li-ion gradient at low rates for homogeneous electrodes having a particle size distribution as shown in Figure 5.7 and predicted recently⁵².

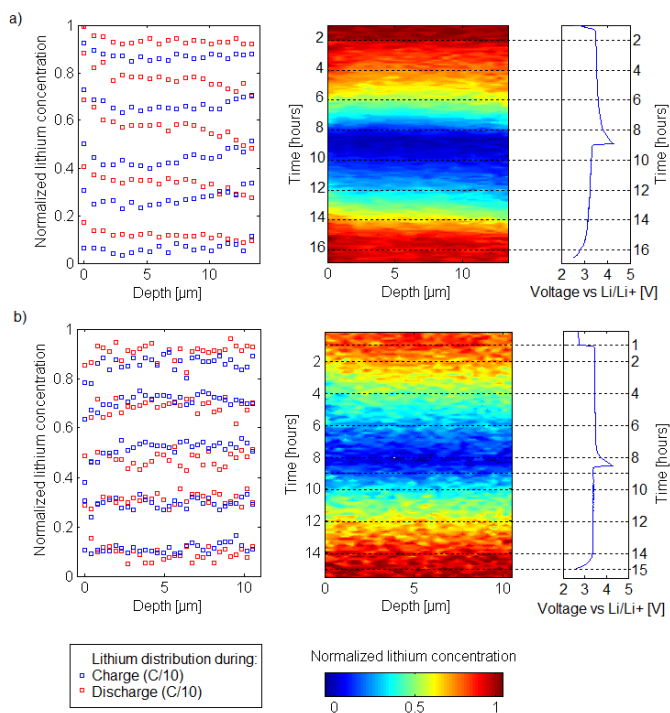


Figure 5.9. Lithium distribution in LiFePO_4 (140 nm) electrodes cycled at C/10. (a) with 10% carbon black as conductive additive and (b) with 50% carbon black as conductive additive. Left: Li-ion concentrations at various stages during charge and discharge, right: concentration evolution during a full cycle. The current collector is located at the left and the electrolyte at the right.

To investigate what charge transport mechanisms play a role at C/10 and beyond experiments were performed on homogeneous electrodes using an average LiFePO_4 particle size of 140 ± 56 nm. Contrary to what was observed at C/50 the concentration profiles at C/10 shown in Figure 5.9 reveal a small but well resolved Li-ion gradient. Comparing the charge and discharge states in Figure 5.9.a shows that part of the electrode located near the current collector appears to be more reactive. During charge Li-ions deplete first near the current collector side and during discharge Li-ions are first inserted near the current collector side. This Li-

ion gradient throughout the electrode provides insight in which charge transport process limits the (dis)charge rate in these electrodes. If charge transfer over the electrolyte-active material interface (located in the pores of the electrode) or the phase nucleation/transition kinetics in the active material would be rate limiting no Li-ion gradient should be expected over the depth of the electrode, as was observed at lower rates.

However, because part of the electrode near current collector is more reactive, the electronic conductivity throughout the electrode must be the origin of the observed Li-ion gradient at C/10. Apparently, the electronic wiring provided by the 10% carbon black in combination with the carbon coating of the LiFePO_4 particles dominates the internal resistance of the battery at this rate. To investigate this intriguing finding the same C/10 charge discharge experiment was repeated with a LiFePO_4 electrode having a much larger (50%) carbon black content with the intention to improve the electronic wiring throughout the electrode. The result is shown in Figure 5.9.b where the signal to noise ratio is compromised due to the decrease in active material reducing the amount of lithium present which decreases the detected ^3H intensity. The small difference between charge and discharge and the absence of a clear gradient indicate that the increase in carbon black content improved the electronic conductivity of the electrode lifting the Li-ion gradient observed in Figure 5.9.a. Generally, ion diffusion limitations through the electrode/electrolyte matrix are predicted to limit overall charge transport^{57,58,63,65} and electronic resistance is not considered. The present results show that even for carbon coated LiFePO_4 in combination with 10 wt% carbon black electronic conduction can dominate charge transport through porous electrodes, indicating this is an important factor to be considered in kinetic modeling of electrodes.

The time resolution of the in-situ NDP setup is limited by the neutron flux, which in the present setup is approximately 5 minutes, thus limiting operando NDP to approximately 1C cycling rates. Therefore, concentration gradients at higher rates were measured under ex-situ conditions. To minimize relaxation effects due to ionic and electronic exchange between the particles within the electrode,

batteries were disassembled and the electrode washed with DMC (dimethyl carbonate) within 2 minutes after charging to the desired state.

The normalized Li-ion concentration after a 30 minutes charge at 1C rate is shown in Figure 5.10 a. The preferential Li-ion depletion at the current collector side (left side of the Li-ion concentration profiles), result in approximately 30% difference in concentration compared to the electrolyte side, indicates that even at 1C the electronic conduction throughout the electrode matrix limits the overall charge transfer. However increasing the charge rate to 5C, shown in Figure 5.10.b, and 20C, shown in Figure 5.10.c, completely changes this picture. At 5C no Li-ion gradient is observed and at 20C the gradient inverses, indicating that Li-ion depletion predominantly takes place at the electrolyte side (right side of the Li-ion concentration profiles). This indicates that at high rate (20C) conditions next to the electronic limitations a second limitation comes into play. Also the finite Li ion transport becomes apparent in the side against the current collector: there the Li cannot be inserted in the electrolyte yet because first the Li in the electrolyte near the separator needs to have been depleted. So one may state that both the electronic limitations and the ionic limitations in part of the electrode determine the observed gradient now. We anticipate that in this case the ionic wiring, the Li-ion transport through the electrolyte in the pores of the electrode, dominates the internal resistance of the battery. Although direct observation of Li-ion gradients has been unavailable up to date, it has been long recognized that in many cases the ionic transport through the electrolyte and through the porous electrode structure is rate limiting and not the electrode material itself^{23-30,58}. This is also supported by the decreasing capacity at the same (dis)charge rate while increasing the electrode thickness^{23,59}. Interestingly, at 5C electronic conduction and ionic conduction appear to become comparable, which cancels out the gradient. Thereby, Figure 5.10 demonstrates the transition in rate limiting charge transport process from electronic conduction up to 1C, which is canceled out at 5C by ionic transport limitations, the latter dominating above 5C.

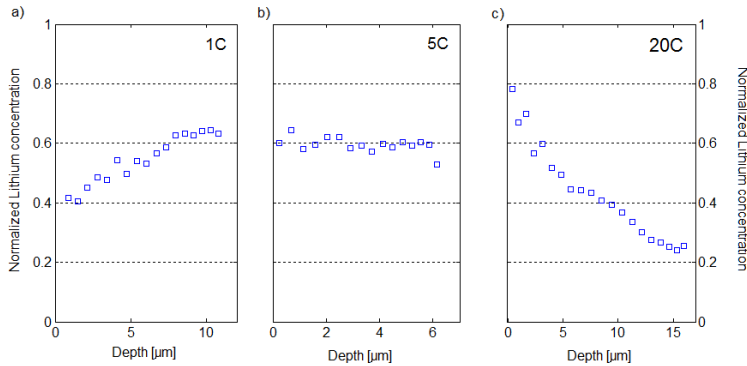


Figure 5.10. Normalized Li-ion concentrations measured ex-situ, a) after 30 minute charge at 1C, b) after 6 minutes charge at 5C and c) after 2 minutes charge at 20C. The current collector is located at the left and the electrolyte at the right.

It should be realized that the rates at which the transition between the different rate limiting charge transport mechanisms takes place strongly depends on the electrode morphology (i.e. thickness, porosity and tortuosity) formulation (i.e. weight percentage active material, conductive additive etc.) electrolyte and molarity, and the electrode material itself. Typically the ionic and electronic conductivity strongly depend on the porosity of the electrode matrix having an optimum around 35% porosity²⁵ which is aimed for in electrode preparation. Given the current results it is interesting to find how nucleation, electronic and ionic conduction play a role at variable cycling rates in other two phase materials. Another challenge is to find out how the observed asymmetry between charge and discharge⁵⁷ influences the Li-ion gradients and rate limiting transport mechanisms, which is subject of our future studies.

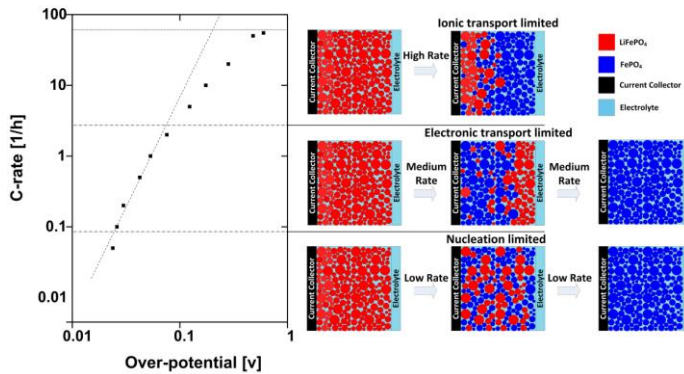


Figure 5.11. C-rate versus overpotential including a schematic representation of the observed Li-ion concentration profiles that allow to distinguish the different rate-limiting rate processes in the different rate regimes.

Figure 5.11 shows a double logarithmic plot of the overpotential versus the charge rate during galvanostatic experiments where the overpotential was selected at the onset of the voltage plateau. Three different charge rate regions can be distinguished that can be correlated to the different rate limiting charge transport mechanisms observed directly in the Li-ion concentration profiles using NDP. At low rates, C/50 to C/10, the particle size dependent two-phase nucleation dominates the charge transport, demonstrated in Figure 5.8 where the smaller LiFePO₄ particles show lower nucleation barriers as compared to larger particles. This reveals that nucleation barriers dominate the resistance against (dis)charging, consistent with extrapolation to a non-zero value of the overpotential at zero current density. At intermediate rates the relation between the current and overpotential is approximately linear, consistent with an Ohmic relation (for a linear plot see Figure 5.12). This is in line with the observed depletion near the current collector upon charge, see Figures 5.9.a and 5.10.a, suggesting electronic conduction limitations at cycling rates between C/10 and 1C. Finally, increasing the charge rate above 5C leads to a larger increase in overpotential reflecting diffusion limited conditions consistent with the observed Li-ion depletion at the electrolyte side of the electrode upon charge shown in Figure 5.10.c.

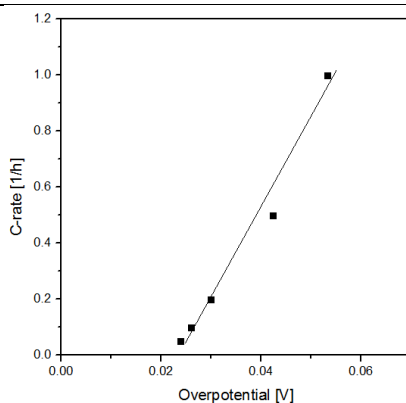


Figure 5.12. A plot of the first 5 data points of figure 5.11 of the manuscript on double linear axis indicating the linear ohmic behaviour of the overpotential with current. Note that the line does not cross the origin as would be the case in an ideal resistor since at zero overpotential the nucleation barrier inhibits the current.

The present results demonstrate that the rate limiting charge transport phenomena not only depends on the electrode morphology and formulation, as should be expected, but also on the (dis)charge rate. This has important consequences for battery design, as depending on the applied battery cycling rate a different electrode design should be applied to minimize the internal resistance and thereby reducing the overpotential, maximizing the energy efficiency and extending the cycle life.

5.4 Conclusions

Summarizing, in-situ NDP was performed for the first time on conventional Li-ion batteries providing direct observation of the evolution of Li-ion concentration gradient in LiFePO_4 electrodes at different electrochemical conditions for different types of electrodes. The results give unique direct insight unavailable up to date revealing what charge transport mechanism dominates at what conditions. It is demonstrated that the rate limiting charge transport mechanism, determining the internal resistance and overpotential of Li-ion batteries, depends both on the electrode composition and, more surprisingly, on the actual (dis)charge rate. The results provide both fundamental insights, challenging electrode modeling, as well as having practical implications for electrode design aiming at improved battery performance. At low (dis)charge rates LiFePO_4 nucleation barriers appear rate limiting, proving lower nucleation barriers for smaller particles. At intermediate rates depletion at the current collector side of the electrode indicate that the ohmic electronic resistance in the electrode is rate limiting, an unexpected result with important implications. In contrast, at high (dis)charge rates the observed Li-ion concentration gradients indicate that ionic diffusion through the porous electrode matrix is rate limiting. These results indicate that depending on the applied (dis)charge a different route should be chosen to lower the internal resistance, and hence improve rate capacities and overall efficiency. Thereby in-situ Neutron Depth Profiling provides unique insight in the charge transport mechanism of Li-ion battery electrodes under realistic in operando conditions, a prerequisite for the improvement of Li-ion battery performance.

References

- (1) Newman, J.; Tiedemann, W. *Aiche Journal* 1975, 21, 25.
- (2) Bazant, M. Z. *Accounts of Chemical Research* 2013, 46, 1144.
- (3) Padhi, A. K.; Nanjundaswamy, K. S.; Goodenough, J. B. J. *Electrochem. Soc.* 1997, 144, 1188.
- (4) Ravet, N. e. a. In *Electrochemical Society Fall Meeting, Honolulu, Hawaii (Electrochemical Society, Pennington, New Jersey, 1999)* 1999.
- (5) Huang, H.; Yin, S. C.; Nazar, L. F. *Electrochemical and Solid State Letters* 2001, 4, A170.
- (6) Herle, P. S.; Ellis, B.; Coombs, N.; Nazar, L. F. *Nature Materials* 2004, 3, 147.
- (7) Maier, J. *Nat. Mater.* 2005, 4, 805.
- (8) Bruce, P. G.; Scrosati, B.; Tarascon, J. M. *Angewandte Chemie-International Edition* 2008, 47, 2930.
- (9) Arico, A. S.; Bruce, P.; Scrosati, B.; Tarascon, J. M.; Van Schalkwijk, W. *Nat. Mater.* 2005, 4, 366.
- (10) Wagemaker, M.; Mulder, F. M. *Accounts of Chemical Research* 2013, 46, 1206.
- (11) Cogswell, D. A.; Bazant, M. Z. *Nano Letters* 2013, 13, 3036.
- (12) Van der Ven, A.; Wagemaker, M. *Electrochemistry Communications* 2009, 11, 881.
- (13) Maier, J. *Angewandte Chemie-International Edition* 2013, 52, 4998.
- (14) Ganapathy, S.; Wagemaker, M. *Acs Nano* 2012, 6, 8702.
- (15) Meethong, N.; Huang, H. Y. S.; Carter, W. C.; Chiang, Y. M. *Electrochemical and Solid State Letters* 2007, 10, A134.
- (16) Lee, K. T.; Kan, W. H.; Nazar, L. F. *Journal of the American Chemical Society* 2009, 131, 6044.
- (17) Zhang, X.; van Hulzen, M.; Singh, D. P.; Brownrigg, A.; Wright, J. P.; van Dijk, N. H.; Wagemaker, M. *Nano Letters* 2014, 14, 2279.

- (18) Liu, H.; Strobridge, F. C.; Borkiewicz, O. J.; Wiaderek, K. M.; Chapman, K. W.; Chupas, P. J.; Grey, C. P. *Science* 2014, 344.
- (19) Bai, P.; Cogswell, D. A.; Bazant, M. Z. *Nano Letters* 2011, 11, 4890.
- (20) Cogswell, D. A.; Bazant, M. Z. *ACS Nano* 2012, 6, 2215.
- (21) Malik, R.; Zhou, F.; Ceder, G. *Nature Materials* 2012, 10, 587.
- (22) Kang, B.; Ceder, G. *Nature* 2009, 458, 190.
- (23) Yu, D. Y. W.; Donoue, K.; Inoue, T.; Fujimoto, M.; Fujitani, S. *Journal of the Electrochemical Society* 2006, 153, A835.
- (24) Jamnik, J.; Dominko, R.; Erjavec, B.; Remskar, M.; Pintar, A.; Gaberscek, M. *Advanced Materials* 2009, 21, 2715.
- (25) Fongy, C.; Jouanneau, S.; Guyomard, D.; Badot, J. C.; Lestriez, B. *Journal of the Electrochemical Society* 2010, 157, A1347.
- (26) Fongy, C.; Gaillet, A. C.; Jouanneau, S.; Guyomard, D.; Lestriez, B. *Journal of the Electrochemical Society* 2010, 157, A885.
- (27) Johns, P. A.; Roberts, M. R.; Wakizaka, Y.; Sanders, J. H.; Owen, J. R. *Electrochemistry Communications* 2009, 11, 2089.
- (28) Zhou, J.; Danilov, D.; Notten, P. H. L. *Chemistry-a European Journal* 2006, 12, 7125.
- (29) Gaberscek, M.; Jamnik, J. *Solid State Ionics* 2006, 177, 2647.
- (30) Singh, D. P.; Mulder, F. M.; Abdelkader, A. M.; Wagemaker, M. *Advanced Energy Materials* 2013, 3, 572.
- (31) Srinivasan, V.; Newman, J. *Journal of the Electrochemical Society* 2004, 151, A1517.
- (32) Safari, M.; Delacourt, C. *Journal of the Electrochemical Society* 2011, 158, A63.
- (33) Singh, G. K.; Ceder, G.; Bazant, M. Z. *Electrochimica Acta* 2008, 53, 7599.
- (34) Ferguson, T. R.; Bazant, M. Z. *Journal of the Electrochemical Society* 2012, 159, A1967.
- (35) Holtz, M. E.; Yu, Y.; Gunceler, D.; Gao, J.; Sundararaman, R.; Schwarz, K. A.; Arias, T. A.; Abruña, H. D.; Muller, D. A. *Nano Letters* 2014, 14, 1453.

- (36) See, K. A.; Leskes, M.; Griffin, J. M.; Britto, S.; Matthews, P. D.; Emly, A.; Van der Ven, A.; Wright, D. S.; Morris, A. J.; Grey, C. P.; Seshadri, R. *Journal of the American Chemical Society* 2014, 136, 16368.
- (37) Ogata, K.; Salager, E.; Kerr, C. J.; Fraser, A. E.; Ducati, C.; Morris, A. J.; Hofmann, S.; Grey, C. P. *Nature Communications* 2014, 5.
- (38) Siegel, J. B.; Lin, X.; Stefanopoulou, A. G.; Hussey, D. S.; Jacobson, D. L.; Gorsich, D. J. *Electrochem. Soc.* 2011, 158, A523.
- (39) Butler, L. G.; Schillinger, B.; Ham, K.; Dobbins, T. A.; Liu, P.; Vajo, J. J. *Nucl. Instr. Meth. Phys. Res. A* 2011, 651, 320.
- (40) Riley, G. V.; Hussey, D. S.; Jacobson, D. L. *ECS Transactions* 2010, 25, 75.
- (41) Wang, J.; Liu, D. X.; Canova, M.; Downing, R. G.; Cao, L. R.; Co, A. C. *Journal of Radioanalytical and Nuclear Chemistry* 2014, 301, 277.
- (42) Oudenhoven, J. F. M.; Labohm, F.; Mulder, M.; Niessen, R. A. H.; Mulder, F. M.; Notten, P. H. L. *Advanced Materials* 2012, 23, 4103.
- (43) Zhang, X.; Wagemaker, M. IMLB 2014 poster abstract <https://ecs.confex.com/ecs/imlb2014/webprogram/Paper35552.html>.
- (44) Wagemaker, M. 2013. Abstract Mon-A1-07 Solid State Ionics 19 Kyoto. (2013).
- (45) Wagemaker, M. 2013. Abstract SSE 2013 http://sse2013.uni-hd.de/Abstracts/abstract_Wagemaker_SSE2013.pdf. (2013).
- (46) Liu, D. X.; Wang, J.; Pan, K.; Qiu, J.; Canova, M.; Cao, L. R.; Co, A. C. *Angewandte Chemie-International Edition* 2014, 53, 9498.
- (47) Ziegler, J. F.; Cole, G. W.; Baglin, J. E. E. *J. Appl. Phys.* 1972, 43, 3809.
- (48) Downing, R. G.; Fleming, R. F.; Langland, J. K.; Vincent, D. H. *Nucl. Instrum. Methods* 1983, 218, 47.
- (49) Biersack, J. P.; Fink, D.; Henkelmann, R.; Muller, K. *Nucl. Instrum. Methods* 1978, 149, 93.
- (50) S. Whitney, S. R. B., Y. H. Huang, J. B. Goodenough *J. Electrochem. Soc.* 2009, 156, A886.
- (51) S.C. Nagpure, P. M., M. Canova, L. R. Cao *J. Powder. Sources* 2014, 248, 489.

- (52) S. C. Nagpure, R. G. D., B. Bhushan, S. S. Babu, L. Cao *Electrochim. Acta* 2011, 56, 4735.
- (53) S.C. Nagpure, R. G. D., B. Bhushan *Scripta Mater.* 2012, 67, 669.
- (54) J. F. M. Oudenhoven, F. L., M. Mulder, R. A. H. Niessen, F. M. Mulder and P. H. L. Notten *Adv. Mater.* 2011, 23, 4103.
- (55) Ferguson, T. R.; Bazant, M. Z. *Electrochimica Acta* 2014, 146, 89.
- (56) Maier, J. *Solid State Ionics* 2002, 154, 291.
- (57) West, K.; Jacobsen, T.; Atlung, S. *Journal of the Electrochemical Society* 1982, 129, 1480.
- (58) Doyle, M.; Newman, J. *Journal of Applied Electrochemistry* 1997, 27, 846.
- (59) Thunman, M.; Marquardt, K.; Hahn, R.; Kober, D.; Goerke, O.; Schubert, H. *ECS Transactions* 2012, 41, 147.
- (60) Srinivasan, V.; Newman, J. *Electrochemical and Solid State Letters* 2006, 9, A110.
- (61) Esteban, G.-T., Delft University of Technology 2014.
- (62) Grace, J.; Marijnissen, J. J. *Aerosol Sci.* 1994, 25, 1005.
- (63) Ziegler, J. F.; Ziegler, M. D.; Biersack, J. P. *Nucl. Instrum. Methods B* 2010, 268, 1818.

Chapter 6

Magnéli-phase Ti_4O_7 as negative electrode for Li-ion batteries

Abstract

A combined theoretical and experimental study is performed on the Magnéli-phase Ti_4O_7 system, aiming at finding a negative electrode material within the stability window of typical Li-ion battery electrolytes. Based on first principle calculations using the DFT generalized gradient approximation (GGA) the structure of the endmember phases Ti_4O_7 and $\text{Li}_2\text{Ti}_4\text{O}_7$ was investigated. The calculations resulted in an average voltage of 0.92 V which is at the edge of the lower stability limit of commonly used electrolytes (such as LiPF_6 EC/DMC). This suggests a higher stability, and thereby, longer cycle life compared to negative electrodes working at lower potentials. Galvanostatic charging and discharging results in an average voltage of around 1.0 V. For the pristine material a small reversible capacity of 40 mAh/g is observed. However, carbon coating improves this towards 140 mAh/g, which is maintained up to 50 cycles.

6.1 Introduction

The high energy density of lithium-ion batteries has facilitated the development of mobile electronic equipment and is the key towards electrification of mobility by means of hybrid and electrical vehicles¹⁻⁴. It is a challenge to identify novel materials that may be suitable for the future rechargeable Li-ion batteries with improved performance and safety. The thermodynamic stability of Li-ion batteries requires the electrochemical potentials of the two electrodes to fall within the stability window of the electrolyte⁵. An anode with a voltage above the lowest unoccupied molecular orbital (LUMO) will reduce the electrolyte unless a Solid Electrolyte Interface (SEI) develops that passivates further electron transfer from the negative electrode to the electrolyte LUMO. Similarly, when the cathode has a voltage higher than the highest occupied molecular orbital (HOMO) the electrolyte will be oxidized. In this way the irreversible formation of the SEI provides a kinetic stability, but which, on the long term, reduces the cycle life and the capacity. The reduction potential of the most commonly used carbonate electrolytes is just below 1.0 V, for instance 0.8 V vs Li/Li⁺ for LiPF₆ in EC/DMC (1:1)⁵. To replace graphite, operating around 0.2 V with a capacity of 372 mAh/g, would require a material working around 1.0 V, preferably with a higher capacity to compensate for the loss in energy density due to the lower operating voltage of the battery. The current options at least satisfying the demand on the potential are mainly offered by titanium oxides like, anatase⁶, rutile⁷, brookite⁸, spinel Li₄Ti₅O₁₂⁹ that operate between 1.5 V and 1.7 V vs Li/Li⁺ with capacities reaching 170 mAh/g¹⁰. This motivates the search for a material with a working potential around 1.0 V vs Li/Li⁺ to make better use of the stability window of the current electrolytes⁵.

Magnéli phase Ti_nO_{2n-1} (where n is between 4 and 10), commercially termed 'Ebonex', exhibits a high electronic conductivity, comparable to that of graphite, and is commonly used as an additive in lead-acid batteries¹¹. Ti₄O₇ has in particular been investigated for its electronic conductivity and optical properties. The first use of Magnéli phase Ti_nO_{2n-1} as Li-ion battery electrode material was reported by Han *et al.*^{12,13}, who prepared nanoscale Ti₄O₇ and Ti₉O₁₇ nanowires by

a heat-treatment of thick $\text{H}_2\text{Ti}_3\text{O}_7$ nanobelts under a hydrogen atmosphere at 1050 °C. The intercalation reaction of Ti_4O_7 can be written as $\text{Ti}_4\text{O}_7 + 2\text{Li} \rightarrow \text{Li}_2\text{Ti}_4\text{O}_7$, with a theoretical capacity of 175 mAh/g. Han *et al.*^{12,13} reported an average voltage for Ti_9O_{17} nanowires of about 0.9 V vs Li/Li^+ with a reversible capacity around 70 mAhg⁻¹, which was increased to 130 mAhg⁻¹ when a carbon coating was applied¹³. In the present work we combine DFT calculations and electrochemical analysis of Ti_4O_7 to further investigate the Li-ion electrode properties and its promise as negative electrode material.

6.2 Methods

6.2.1 Density Functional Theory

Density Functional Theory (DFT)¹⁴ calculations were performed incorporating exchange and correlation effects within the generalized gradient approximation (GGA)¹⁵ as implemented in the Vienna ab Initio Simulation Package (VASP)^{16,17}. The PW91 functional¹⁸ for GGA and a plane-wave basis set with the projector augmented wave method¹⁹ as implemented in VASP was used. The energy cut-off considered here is taken to be 400 eV and the convergence in energy and force was set to 1×10^{-5} eV and 0.01 eV/Å, respectively.

Leonov *et al.* used LDA+U calculations on the Ti_4O_7 low-temperature structure²⁰ and Liborio *et al.* performed spin polarized local-density approximation (LSDA) without considering the effect of local *d* electrons²¹. Generally, LDA+U is used to take into account the strong localization of the metal *d* orbital. To find out which method is most accurate for the pristine Ti_4O_7 and lithiated materials at room temperature, both GGA and GGA+U were applied and the results are compared to experimental data. For the GGA+U calculations the Coulomb interaction parameter was set to $U = 3.0$ eV and exchange coupling $J = 0.8$ eV following previously work²⁰. In addition the possible presence of magnetic moments was considered by applying spin-polarized calculations.

6.2.2 Sample preparation

As starting material fine Ti₄O₇ powder from Atraverda was used. Table sugar was used for carbon coating of the Ti₄O₇ surface. The active material (Ti₄O₇) was mixed with the sugar at a mass ratio of 4:1 resulting in around 10% carbon in the system. After that, the material was ball-milled with a low speed (150 rpm) with a ball to power ratio 10:1 for a better mixture followed by calcination in the furnace under a N₂ atmosphere for 12 h. Tungsten carbide balls and jar were used to avoid contamination of possible metal elements. For the electrochemical test, a slurry of the Ti₄O₇, Carbon Black (Super P), PVDF, (polyvinylidene fluoride, Solvay) was dissolved in NMP (N-methylpyrrolidone, Merck), which was casted on carbon coated aluminum current collectors. The mass ratio of the active material (Ti₄O₇), carbon black (SuperP) and binder (PVDF) is of 50:30:20. The coatings were dried overnight on the heater under air at 155 °C followed by drying under vacuum around 60 °C for more than 24 hours. The resulting coatings were pressed using a hand roller press to enhance the electronic conduction and assembled in a Swagelok type cell under argon atmosphere (<0.1 ppm O₂/H₂O). Glass fiber disks (Whatman) were used as separators and the electrolyte used was 1.0 molar LiPF₆ in EC/DMC (ethylene carbonate and dimethyl carbonate in a 1:1 ratio) (Novolyte, battery grade). All the electrochemical tests were performed using a Maccor 4300 battery cycler.

6.3 Results

6.3.1 DFT calculations

At room temperature, the crystal structure of Ti_4O_7 can be described as rutile-like slabs with a corundum-like atomic arrangement separated at a distance of 8.989 \AA , see Figure.6.1.a-b. Two types of Ti sites can be distinguished, Ti_1 - Ti_4 , located inside the rutile block, and Ti_5 - Ti_8 , which are located at the ends of the rutile block²³.

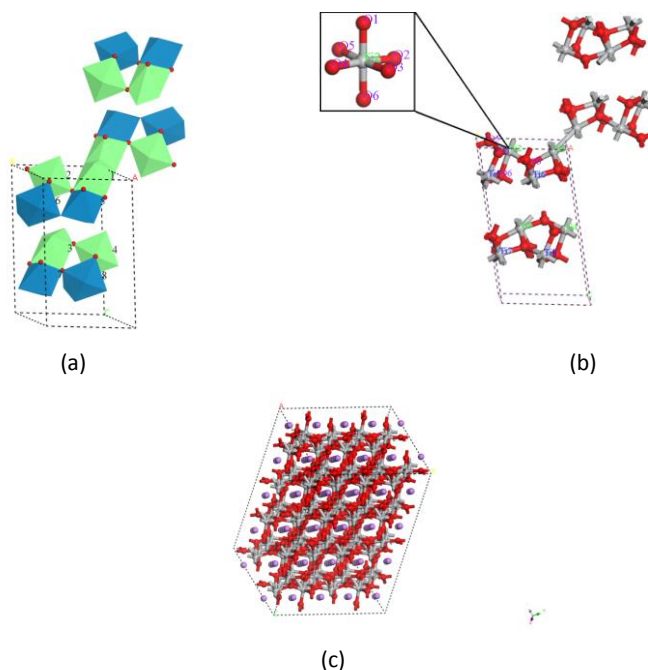


Figure 6.1. The room temperature crystal structure of Ti_4O_7 and the Li-ion inserted structure of $\text{Li}_2\text{Ti}_4\text{O}_7$. (a) An illustration of the two types of Ti positions. Green and blue atoms represent the inner and outside Ti atoms, respectively, with the different numbers. (b) Ball and stick view of Ti_4O_7 with atom labels and an enlarged rutile structure of Ti_2 surrounded by 6 oxygen atoms. (c) Intercalated structure $\text{Li}_2\text{Ti}_4\text{O}_7$ showing a $2 \times 2 \times 2$ supercell. The red, white and pink balls represent the Ti, O and Li atoms, respectively.

Previous experimental studies have shown that the crystal structure, as well as, the electronic structure depends strongly on temperature. At room temperature ($T \geq 298\text{K}$) Ti₄O₇ displays paramagnetic behavior²⁴ and high conductivity (around 1500 Scm^{-1})²⁵. The Ti₄O₇ starting structure for the calculations was constructed according to the experimental unit cell with the lattice parameters $a = 5.60 \text{ \AA}$, $b = 7.133 \text{ \AA}$, $c = 12.466 \text{ \AA}$, $\alpha = 95.05^\circ$, $\beta = 95.17^\circ$, $\gamma = 108.71^\circ$ and P-1 space group²³. Geometrical optimization was performed for the possible magnetic states applying the GGA and GGA+U approximations. The results shown in Table 6.1.

Table 6.1. Calculation result of Ti₄O₇ energy using different optimization method.

Setting Method	Paramagnetic	Ferromagnetic	Antiferromagnetic
GGA	-393.08 eV	-393.06 eV	-393.03 eV
GGA+U	-361.18 eV	-361.92 eV	-361.82 eV

It is observed that for the GGA method the paramagnetic state results in the lowest energy, which agrees with experimental observations²⁴. Although in some cases^{20,21} the strong electronic correlations in the Ti 3d shell need to be taken into account, our calculation, using the GGA+U method indicates that the ferromagnetic state has the lowest energy contradicting experimental findings. Upon lithiation titanium can be reduced from Ti^{3.5} up to Ti³⁺, indicating that the maximum lithiated composition is Li₂Ti₄O₇. For the lithiated Li₂Ti₄O₇ composition, Li atoms were added to all likely oxygen coordinated sites, after which the cells were geometrically optimized. This resulted in Li positions in the 1D channels with an octahedral oxygen coordination. The final atom positions of lithiated Ti₄O₇ from geometric optimization are listed in Table 6.2

Table 6.2 Calculated atom position of lithiated Ti_4O_7

Atom	x	y	z	Atom	x	y	z
O	0.1145	0.8657	0.0158	O	0.4135	0.7145	0.4430
O	0.5864	0.7854	0.0569	O	0.8856	0.6344	0.4841
O	0.8561	0.4974	0.0805	Ti	0.6860	0.4419	0.7014
O	0.3257	0.4385	0.1394	Ti	0.6810	0.9387	0.7020
O	0.5255	0.1444	0.1618	Ti	0.6860	0.9423	0.2013
O	0.0370	0.0738	0.1982	Ti	0.6811	0.4392	0.2019
O	0.2914	0.7902	0.2229	Ti	0.2203	0.1519	0.5673
O	0.2916	0.2900	0.7231	Ti	0.2138	0.6563	0.5640
O	0.0370	0.5733	0.6984	Ti	0.2137	0.1566	0.0639
O	0.5254	0.6438	0.6619	Ti	0.2203	0.6520	0.0673
O	0.3258	0.9382	0.6394	Ti	0.3139	0.5580	0.2985
O	0.8562	0.9974	0.5806	Ti	0.3189	0.0612	0.2979
O	0.5864	0.2854	0.5569	Ti	0.3139	0.0576	0.7986
O	0.1143	0.3655	0.5158	Ti	0.3188	0.5607	0.7980
O	0.8854	0.1342	0.9841	Ti	0.7796	0.8480	0.4326
O	0.4135	0.2145	0.9430	Ti	0.7861	0.3436	0.4359
O	0.1438	0.5025	0.9194	Ti	0.7862	0.8433	0.9360
O	0.6742	0.5614	0.8605	Ti	0.7796	0.3479	0.9326
O	0.4744	0.8555	0.8381	Li	0.5000	0.5000	0.0000
O	0.9629	0.9261	0.8017	Li	0.0000	0.2500	0.7500
O	0.7085	0.2097	0.7770	Li	0.0000	0.7500	0.7500
O	0.7083	0.7099	0.2768	Li	0.5000	0.5000	0.5000
O	0.9629	0.4266	0.3015	Li	0.5000	0.0000	0.5000
O	0.4745	0.3561	0.3380	Li	0.5000	0.0000	0.0000
O	0.6741	0.0617	0.3605	Li	0.0000	0.2500	0.2500
O	0.1437	0.0025	0.4193	Li	0.0000	0.7500	0.2500

To calculate the average potential of the Li-ion insertion in $Li_xTi_4O_7$ between $x_1 = 0$ and $x_2 = 1$ we assume the negative electrode to be lithium metal. The energy obtained by discharge between $Li_{x_1}M$ and $Li_{x_2}M$ ($x_2 > x_1$) is the integral of the voltage times the displaced charge:

$$E = \int_0^{q_{tot}} V(x) dq = - \int_0^{q_{tot}} \frac{\mu_{Li}^{IC}(x) - \mu_{Li}^0}{e} dq \quad (6-1)$$

where μ_{Li}^0 and μ_{Li}^{iC} represent the chemical potential of Li metal and Li (per atom) in the intercalation compound respectively²⁶. Considering that all the displaced charge is due to Li^+ , the average voltage can be expressed in terms of the Gibbs free energies:

$$\bar{V} = \frac{-\Delta G_r}{(x_2 - x_1)F} = -\frac{G_{Li_2M}^{cathode} - G_{Li_1M}^{cathode} - (x_2 - x_1)G_{Li}}{(x_2 - x_1)F} \quad (6-2)$$

Where F is the Faraday constant. $Li_{x_1}M$ and $Li_{x_2}M$ represent different compositions of the $Li_xTi_4O_7$ material, G is the Gibbs free energy of each compound²⁶. Given that $\Delta G_r \equiv \Delta E_r + P\Delta V_r - T\Delta S_r$, and $P\Delta V_r$ is of the order of 10^{-5} eV while $T\Delta S_r$ is of the order of the thermal energy, both are very small compared to the configurational energy ΔE_r , which is in the order of 3-4 eV per atom. As a consequence the calculated DFT-GGA energies can be used to estimate the average voltage between the endmember compositions, in our case resulting in 0.92 V.

6.3.2 Electrochemical Tests

Figure 6.2.a and b show the results of the galvanostatic (dis)charge at C/10 rate down to 0.5 V vs Li/Li^+ for the bare Ti_4O_7 and carbon coated Ti_4O_7 , respectively. Compared to the currently used titanium oxides compounds like anatase⁶, rutile⁷, brookite⁸, spinel $Li_4Ti_5O_{12}$ ⁹, no clear voltage plateau is observed, indicating the absence of a two-phase reaction. Figure 6.2.a shows that the reversible capacity of bare Ti_4O_7 is around 40 mAh/g, only about 23% of the theoretical capacity (175mAh/g). However, carbon coating significantly increases the reversible capacity, initially reaching about 160 mAh/g and stabilizing at 140 mAh/g after 10 cycles (see Figures 6.2.b and 6.2.c). Previous work also showed that carbon coating leads to a large improvement of the capacity of nanoscale Magnéli-phase materials¹³. It is expected that the high electrical conductivity facilitates the charge transport between the surface of the active material and current collector, which results in the improved cycling performance. The first discharge of both

bared Ti_4O_7 and carbon coated Ti_4O_7 leads to significantly larger capacities (122mAh/g and 196 mAh/g, respectively). A large part of which appears not reversible during the subsequent (dis)charge. The large capacity loss might be because of the irreversible reaction at the surface for a potential below 0.8 V such as the formation of an Solid Electrolyte Interface (SEI), which also exhibits in other titanium oxides compounds²⁷.

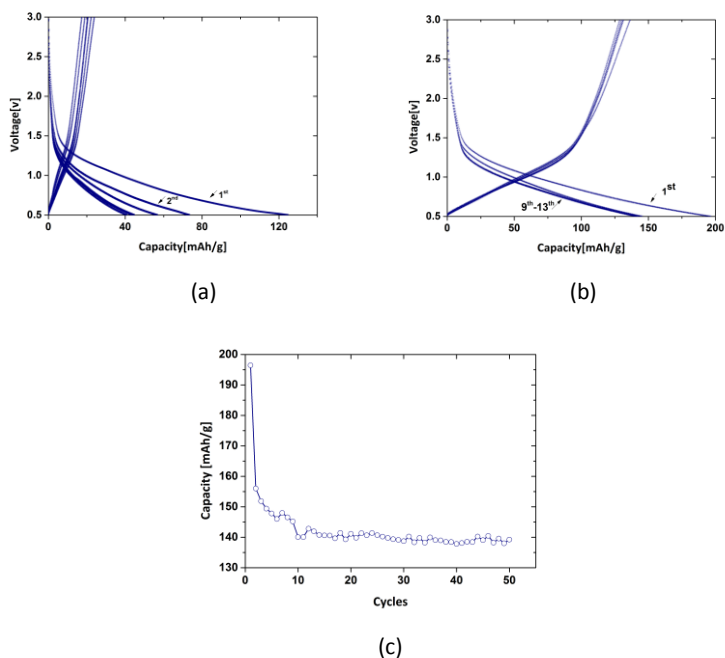


Figure.6.2. Electrochemical test of Ti_4O_7 between 0.5 and 3.0 V vs Li/Li^+ at C/10 rate based on the theoretical capacity. (a) bare Ti_4O_7 powders. (b) carboncoated Ti_4O_7 powders. (c) cycling performance of carbon-coated Ti_4O_7 up to 50 cycles.

6.4 Discussion

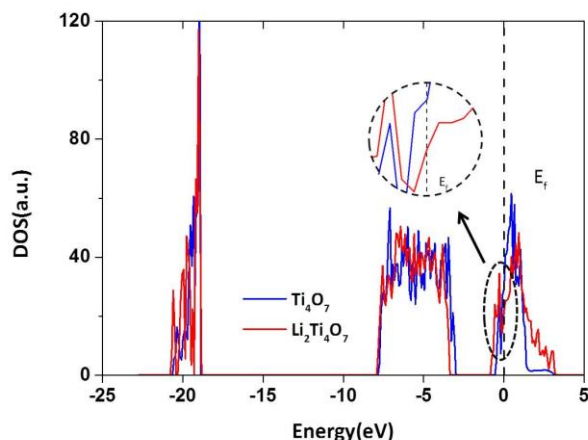


Figure 6.4 comparison between the calculated total density of state (DOS) of Ti₄O₇ (blue) and Li₂Ti₄O₇ (red). The insert shows an enlarged view of the DOS near the Fermi Energy

Without carbon coating the bare Ti₄O₇ only delivered 30% of its theoretical capacity upon electrochemical cycling. A similar behavior was found by Han et al.¹³ and ascribed to the poor conductivity of the surface of the bare Ti₄O₇. Using DFT calculations the electronic structure of Ti₄O₇ and Li₂Ti₄O₇ was predicted, giving another possible explanation.

Figure 6.4 shows the total DOS for the optimized Ti₄O₇ and Li₂Ti₄O₇ structures. For comparison, the energy in Figure 6.4 is normalized to the Fermi energy (4.38 eV and 5.20 eV for Ti₄O₇ and Li₂Ti₄O₇ respectively). The total DOS calculations of both compound show metallic properties as the Fermi energy is localized in the conduction band, indicating that the electrons can be excited to non-localized conduction states. The increase in the Fermi energy upon lithiation of Ti₄O₇ can be ascribed to the additional electrons entering the structures as a result of lithium insertion. At the Fermi level the DOS is larger for Ti₄O₇ compared to Li₂Ti₄O₇, as can be seen in the insert in Figure 6.4. This indicates that more electrons can be

exited to non-localized conduction states in Ti_4O_7 compared to $\text{Li}_2\text{Ti}_4\text{O}_7$, indicating that Ti_4O_7 may have better electronic conductivity. Although both end-members are metallic, this indicates that the conductivity of the lithiated Ti_4O_7 decreases as more lithium is inserted to the system. The use of carbon coated $\text{Li}_2\text{Ti}_4\text{O}_7$ can improve the conductivity of the whole system, explaining the better capacity retention. The average voltage of the electrochemical charge-discharge curves is approximately 0.9 V vs Li/Li^+ , which is in good agreement with the DFT calculations. In fact, Ti_4O_7 can be viewed as oxygen defective Ti_4O_8 . The oxygen defects are the origin of the lower voltage compared to stoichiometric titanium dioxide systems. Using crystal field theory we can understand this mechanism in more detail. Using rutile TiO_2 as a reference system, in the rutile structure the Ti atoms are octahedral coordinated to oxygen, resulting in an overlap of the Ti d_{z^2} , $d_{x^2-y^2}$ orbitals to with the p_x , p_y , p_z orbitals of the O atoms along the octahedral direction²⁶. The σ overlap causes the d - p hybrid orbitals to split into a bonding state e_g and an antibonding state e_g^* , the e_g band having a lower energy and the antibonding e_g^* band having a higher energy. The d_{xy} , d_{yz} , d_{zx} orbitals point away from the O atoms and have no net σ overlap with the p orbitals forming the t_{2g} bands between the e_g band and e_g^* bands, as shown in Figure 6.5.

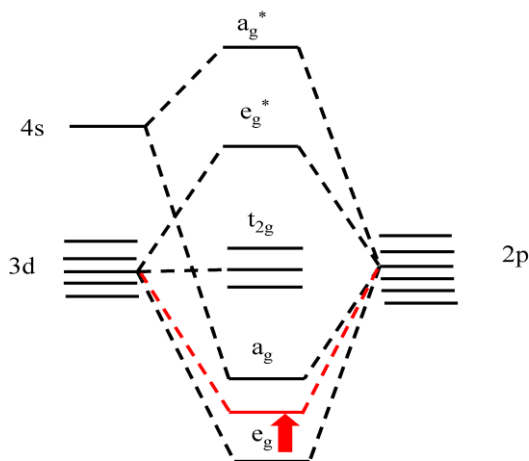


Figure 6.5. Schematic crystal field splitting for octahedral oxygen coordinated titanium atoms. The red line and arrow indicate the expected increase of the e_g band caused by the distorted octahedral in Ti_4O_7 .

Table 6.3-1

Bond	Length [Å]	Bond	Length [Å]
Ti ₂ -O ₁	1.9758	Ti ₂ -O ₄	1.9804
Ti ₂ -O ₂	2.0034	Ti ₂ -O ₅	1.9369
Ti ₂ -O ₃	2.0548	Ti ₂ -O ₆	2.0328

Table 6.3-2

	T ₁	T ₂	T ₅	T ₆	Overall Average
Length [Å]	2.0031	1.9974	2.0188	2.0082	2.0069

Table 6.3-1 Ti-O distance of Ti₂ with surrounding O atoms in the octahedral structure (see Figure 6.1.b insert enlarge part) and **6.3-2** average Ti-O distances for inequivalent titanium atoms where the index of the Ti refer to the Ti atoms depict in Figures 6.1. a-b.

However, Ti_4O_7 does not have a regular octahedral structure. The DFT calculations show that the average Ti-O bond length in optimized Ti_4O_7 is 2.007 \AA whereas in bulk rutile TiO_2 it is 1.964 \AA (see Table 6.3). The increase in the Ti-O bond length leading to a smaller σ overlap between the oxygen- p and Ti- d orbitals, thereby pushing the bonding bands up and the antibonding band down²⁶, which results in the increasing of the lowest band energy of the whole system. Moreover, calculations show that at room temperature the Ti valence in Ti_4O_7 is almost uniformly in the $\text{Ti}^{3.5+}$ state²⁸, which is smaller than that in TiO_2 system (Ti^{4+}). This indicates it will cost more energy to place a lithium atom in the Ti_4O_7 system compared to TiO_2 . This is the origin of the lower average potential vs Li/Li^+ of Ti_4O_7 as compared to titanium dioxide materials.

6.5 Conclusions

In summary, electrochemical tests and DFT calculations were performed on the Magnéli-phase rutile-like structure of Ti_4O_7 investigating its potential use as negative electrode material for Li-ion batteries. The galvanostatic (dis)charging experiments showed that carbon coating is one of the possible ways to improve the electrochemical performance of the Ti_4O_7 system, because it can enhance the electronic conduction on the surface and increase overall conduction in the system during insertion. Both the DFT calculations and experimental studies on Ti_4O_7 resulted in an average voltage of 0.92 V. This lower voltage, compared to the TiO_2 , can be ascribed to the oxygen defective structure that leads to an increase of the lowest electronic bonding band energy. Meanwhile, the average voltage is within the stability window of commonly used electrolyte, suggesting that a longer cycle life may be achieved, which makes this material of interest for Li-ion batteries.

References

- (1) Tarascon, J.-M.; Armand, M. *Nature* **2001**, *414*, 359.
- (2) Tarascon, J.-M.; Recham, N.; Armand, M.; Chotard, J.-N.; Barpanda, P.; Walker, W.; Dupont, L. *Chem. Mater* **2010**, *22*, 724.
- (3) Whittingham, M. S. *Dalton Trans* **2008**, *40*, 5424.
- (4) B.L. Ellis; Lee, K. T.; Nazar, L. F. *Chem. Mater* **2010**, *22*, 691.
- (5) Goodenough, J. B.; Kim, Y. *Chem. Mater* **2010**, *22*, 587.
- (6) Olson, C. L.; Nelson, J.; Islam, M. S. *J Phys. Chem. B* **2006**, *110*, 9995.
- (7) Ohzuku, T.; Takehara, Z.; Yoshizawa, S. *Electrochim. Acta* **1979**, *24*, 219.
- (8) Reddy, M. A.; Kishore, M. S.; V.Pralong; Varadaraju, U. V.; Raveau, B. *Electrochem. Solid-State Lett.* **2007**, *10*, A29.
- (9) Ferg, E.; Gummow, R. J.; Dekock, A.; Thackeray, M. M. *J. Electrochem. Sco.* **1994**, *141*, L147.
- (10) Wagemaker, M.; Mulder, F. *Acc. Chem. Res* **2013**, *46*, 1206.
- (11) Smith, J. R.; Walsh, F. C. *J. App. Electrochem* **1998**, *28*, 1021.
- (12) Han, W. Q.; Zhang, Y. *Appl. Phys. Lett.* **2008**, *92*, 203117.
- (13) Han, W. Q.; Wang, X. L. *Appl. Phys. Lett.* **2010**, *97*, 243104.
- (14) Kohn, W.; Sham, L. J. *Phys. Rev.* **1965**, *140*, A1133.
- (15) Perdew, J. P.; Burke, K.; Ernzerhof, M. *Phys. Rev. Lett.* **1996**, *77*, 3865.
- (16) Furthmuller, J.; Hafner, J.; Kresse, G. *Phys. Rev. B* **1994**, *49*, 14251.
- (17) Kresse, G.; Furthmuller, J. *Phys. Rev. B* **1996**, *54*, 11169.
- (18) Wang, Y.; Perdew, J. P. *Phys. Rev. B* **1991**, *44*, 13298.
- (19) Kresse, G.; Joubert, D. *Phys. Rev. B* **1999**, *59*, 1758.
- (20) Leonov, I.; Yaresko, A. N.; Antonov, V. N.; Schwingenschlögl, U.; Eyert, V.; Anisimov, V. I. *J. Phys.: Condens. Matter* **2006**, *18*, 10955.
- (21) Liorio, L.; Mallia, G. *Phys. Rev. B* **2009**, *79*, 245133.
- (22) Södergren, S.; Siegbahn, H.; Rensmo, H.; Lindström, H.; Hagfeldt, A.; Lindquist, S.-E. *J. Phys. Chem. B* **1997**, *101*, 3087.
- (23) Marezio, M.; Dernier, P. D. *J. Solid State Chem.* **1973**, *3*, 340.

-
- (24) Lakkis, S.; Schlenker, C.; Chakraverty, B. K.; Buder, R. *Phys. Rev. B* **1976**, *14*, 1429.
- (25) Goldschmidt, D.; Watanabe, M. *Mater. Res. Bull.* **1985**, *20*, 65.
- (26) Aydinol, M. K.; Kohan, A. F.; Ceder, G. *Phys. Rev. B* **1997**, *56*, 1354.
- (27) Shu, J. *Electrochem. Solid-State Lett.* **2008**, *11*(12), A238.
- (28) Weissmann, M.; Weht, R. *Phys. Rev. B* **2011**, *84*, 144419.

Summary

Chemical energy storage in Li-ion batteries is a key technology for the future renewable society. Their energy and power density is largely determined by electrode materials that are able to host lithium in their crystal structure. Aiming at faster and more efficient energy storage, one of the key objectives in Li-ion batteries is to improve the charge transport through the complex heterogeneous electrode morphology. The complex transport phenomena and phase behavior are timely topics and subject of many studies and intense debates. Remarkably, our current knowledge is mostly based on ex-situ techniques or techniques that do not have sufficient time and space resolution to reveal the actual phase nucleation and growth in individual grains. On the electrode length scale the absence of experimental probes that allow direct observation of Li-ion transport in electrodes under realistic in-operando conditions hinders fundamental understanding and the development of rational strategies towards improved electrodes. For LiFePO_4 , a state of the art cathode material for today's Li-ion batteries, such direct insights are of high fundamental and practical impact, potentially creating new perspectives in the working and improvements of electrode materials in general. This is the main object of this thesis, revealing the cycling rate dependent phase transition behavior and Li-ion transport throughout the electrodes in LiFePO_4 under realistic in-operando conditions.

In **Chapter3** a complete and consistent picture of the equilibrium and non-equilibrium phase transformation in LiFePO_4 is presented based on cycling rate dependent synchrotron X-ray powder diffraction experiments, the results of which can be categorized in three phase transformation stages. (1) Near equilibrium, displaying the expected first-order phase transition between the FP and LFP end member phases. (2) Intermediate rates lead to the observation of the $\text{Li}_{-0.6}\text{FePO}_4$ metastable phase previously observed challenging the use of a regular solution model by theorists. (3) The most spectacular observation is at 10C up to 60C where the solubility limits in both phases increase dramatically with

increasing (dis)charge rate, causing a fraction of the electrode material to follow a single phase transformation path, bypassing the first-order phase transition. At low (dis)charge rates the absence of broadening is consistent with the previously suggested mosaic transformation, whereas at high (dis)charge the results demonstrate that the phase transformation path in the Li_xFePO_4 system depends on the (dis)charge rate (overpotential) providing a rationale for the remarkable fast kinetics of LiFePO_4 . Nucleation rates are consequently not limiting the transformation rate and thereby these new findings reveal that improvement of electrode performance should focus on optimization the ionic/electronic transport in LiFePO_4 electrodes.

The micro-beam X-ray diffraction presented in **Chapter4** reveal for the first time phase transformations in a large number (~150) of individual electrode particles under realistic in-operando conditions, bringing forward a new fundamental insight in the rate-dependent phase transformations taking place in LiFePO_4 electrodes. At low (dis)charge rates the streaked reflections reveal a phase coexistence of thin platelet domains with a preferred orientation with respect to the a -axis. In combination with the slow transformation rate of individual grains this invalidates the particle-by-particle or mosaic transformation that is commonly assumed to occur at relatively low (dis)charge rates. Even at $C/50$ rates the internal platelet domain structure remains present, indicating very low mobility of well-defined interfaces between the end member phases, challenging current theoretical models, and suggesting that the well-defined internal domains structure is actually responsible for the observed slow transformation rates of individual grains. Increasing the (dis)charge rate suppresses the formation of sharp interfaces, as demonstrated by the vanishing streaked reflections representing the platelet shaped domains. Most likely the increasing unstable intermediate compositions observed in single particles at present, and previously using powder X-ray diffraction, results in larger diffusion coefficients compared to that in the end member phases, and a larger interface mobility due to less concentrated coherency strains, responsible for the faster transformation times observed at present and the high intrinsic rate performance of LiFePO_4 . Measuring the transformation process of individual LiFePO_4 particles allows for the first time

quantification of local current densities in Li-ion battery electrodes under realistic (dis)charge conditions. The results suggest the (dis)charge rate is dependent on the local current density, which was derived from the average transformation times of individual grains.

Beside the direct view of phase transition behaviour of LiFePO_4 during different rates, in **Chapter 5** in-situ Neutron Depth Profiling (NDP) was performed for the first time on conventional Li-ion batteries, providing direct observations of the evolution of Li-ion concentration gradient in LiFePO_4 electrodes at different electrochemical conditions for different types of electrodes. The results give unique direct insights, unavailable up to date, revealing what charge transport mechanism dominates at what conditions. It is demonstrated that the rate limiting charge transport mechanism, determining the internal resistance and overpotential of Li-ion batteries, depends both on the electrode composition and, more surprisingly, on the actual (dis)charge rate. The results provide both fundamental insights that challenge current electrode charge transport models, as well as practical directions towards electrode design for improved battery performance. At low (dis)charge rates LiFePO_4 nucleation barriers appear rate limiting, proving lower nucleation barriers for smaller particles. At intermediate rates depletion at the current collector side of the electrode indicate that the ohmic electronic resistance in the electrode is rate limiting, an unexpected result with important implications. In contrast, at high (dis)charge rates the observed Li-ion concentration gradients indicate that ionic diffusion through the porous electrode matrix is rate limiting. These results indicate that depending on the applied (dis)charge a different route should be chosen to lower the internal resistance, and hence improve rate capacities and overall efficiency.

Aiming at the development of a cheap negative electrode material operating just within the stability limit of common liquid electrolytes, the electrochemical properties of the Magnéli-phase rutile-like structure Ti_4O_7 were studied in **Chapter 6** applying both electrochemical tests and DFT calculations. Our galvanostatic (dis)charging experiments show that carbon coating is one of the possible ways to improve the electrochemical performance of the Ti_4O_7 system, most likely because it enhances the electronic conduction on the surface and

increases the overall electronic conductivity of the electrodes. Both the DFT calculations and, experimental studies on the Ti_4O_7 material resulted in an average voltage of ~ 0.9 V. This is relatively low compared to other titanium oxides, which can be ascribed to the oxygen defective structure that leads to an increase of the lowest electronic bonding band energy. As a result the average potential is within the stability window of commonly used electrolytes, suggesting that a long cycle life may be achieved making this material of interest for Li-ion batteries.

In conclusion, the multi technical approach presented in this thesis has led to a consistent and coherent description of rate dependent behavior of individual LiFePO_4 grains and complete electrodes. For the first time in operando microbeam X-ray diffraction and Neutron Depth Profiling were performed. The results illustrate the unique abilities of these techniques in revealing transformation behaviour of individual particles and the charge transport mechanism in Li-ion battery electrodes under realistic in operando conditions, which will provide guidance for future battery and solid state material research and development.

Samenvatting

Chemische energieopslag in Li-ionenbatterijen is een sleuteltechnologie voor de toekomstige duurzame maatschappij. De energie en vermogensdichtheid wordt grotendeels bepaald door materialen voor elektroden, die in staat zijn host lithium op te nemen in hun kristalstructuur. Op weg naar snellere en efficiëntere energieopslag is een van de hoofdoelen in Li-ionen batterijen om het ladingstransport door de complexe heterogene elektrodemorfologie te verbeteren. De complexe transportverschijnselen en het fasegedrag zijn topics van deze tijd en onderwerp van vele studies en intens debat. Het is opmerkelijk, dat onze huidige kennis hoofdzakelijk gebaseerd is op ex-situ technieken of technieken, die onvoldoende oplossend vermogen in tijd en ruimte hebben om de actuele nucleatie en groei van fasen in individuele korrels te volgen. Op de lengteschaal van de elektrode verhindert de afwezigheid van experimentele probes, die directe waarneming van Li-ionentransport in elektrodes onder realistische in operando omstandigheden mogelijk maken, een fundamenteel begrip en de ontwikkeling van rationele strategieën tot verbeterde elektroden. Voor LiFePO_4 , a state of the art kathodemateriaal voor de Li-ionenbatterijen van vandaag, zijn zulke directe inzichten van groot fundamenteel en praktisch belang, potentieel nieuwe perspectieven openend in de werking en verbetering van elektrodematerialen in het algemeen. Het hoofdoel van dit proefschrift is het bestuderen van het cycling rate afhankelijke faseovergangsgedrag en Li-ionentransport door de hele elektrode heen in LiFePO_4 onder realistische in operando omstandigheden.

In **Hoofdstuk 3** wordt een volledig en consistent beeld gepresenteerd van de evenwichts- en niet-evenwichts-faseovergang in LiFePO_4 gebaseerd op cycling rate afhankelijke synchrotron Röntgenpoederdiffractie experimenten, de resultaten waarvan gecategoriseerd kunnen worden in drie faseformatie stadia. (1) Nagenoeg evenwicht, dat de verwachte eerste-orde faseovergang tussen de FP en LFP end member fasen laat zien. (2) Tussenliggende snelheden leiden tot de

observatie van de $\text{Li}_{-0.6}\text{FePO}_4$ metastabiele fase, die eerder werd waargenomen en het gebruik van een regulier oplossingsmodel door theoretici. (3) De spectaculairste waarneming vindt plaats tussen 10C en 60C waar de grenzen van oplosbaarheid in beide fasen dramatisch toenemen bij toenemende (ont)ladingssnelheid, waardoor een fractie van het elektrodemateriaal een enkel faseovergangspad volgt onder voorbijgaan van de eerste-orde faseovergang. Bij lage (ont)ladingssnelheden is de afwezigheid van verbreding consistent met de eerder gesuggereerde mozaïsche transformatie, terwijl bij snelle (ont)lading de resultaten laten zien dat het faseovergangspad in het Li_xFePO_4 systeem afhangt van de (ont)ladingssnelheid (overpotentiaal), wat de opmerkelijk snelle kinetiek van LiFePO_4 verklaart. Nucleatie snelheden begrenzen dus de transformatie snelheden niet en daardoor onthullen deze nieuwe bevindingen dat verbetering van elektrodeprestatie zich vooral moet richten op optimalisatie van het ionen/elektronentransport in LiFePO_4 elektroden.

De micro-beam Röntgendiffractie gepresenteerd in **Hoofdstuk 4** laat voor het eerst faseovergangen zien in een groot aantal (~150) individuele elektrodedeeltjes onder realistische in operando omstandigheden, wat een nieuw fundamenteel inzicht brengt in de snelheidsafhankelijke faseovergangen, die plaats vinden in LiFePO_4 elektroden. Bij lage (ont)ladingssnelheden laten de langgerekte reflecties een fase coëxistentie zien van dunne plaatvormige domeinen met een voorkeursoriëntatie ten opzichte van de a -as. In combinatie met de lage overgangssnelheid van individuele korrels laat dit de ongeldigheid zien van de deeltje-voor-deeltje of mozaïsche transformatie die algemeen wordt aangenomen bij relatief lage (ont)ladingssnelheden. Zelfs bij C/50 snelheden blijft de interne plaatvormige domeinstructuur aanwezig, wat een aanwijzing is voor een zeer lage mobiliteit van goed gedefinieerde interfaces tussen de end member fasen, in tegenspraak met huidige theoretische modellen, en een suggestie dat de goed gedefinieerde interne domeinstructuur inderdaad verantwoordelijk is voor de waargenomen trage overgangssnelheden van individuele korrels. Toename van de (ont)ladingssnelheid onderdrukt de vorming van scherpe interfaces, zoals aangetoond door het verdwijnen van langgerekte reflecties, die een weerspiegeling zijn van de plaatvormige domeinen. Hoogstwaarschijnlijk

resulteren de toenemend onstabiele intermediaire samenstellingen nu waargenomen in enkele deeltjes, en eerder met behulp van poeder Röntgen diffractie, in grotere diffusiecoëfficiënten in vergelijking met die in de end member fasen, en een hogere interface mobiliteit dankzij minder geconcentreerde coherentiespanningen, verantwoordelijk voor de snellere transformatietijden, die nu waargenomen zijn en de hoge intrinsieke snelheidsprestatie van LiFePO_4 . Meting van het transformatieproces van individuele LiFePO_4 deeltjes laat voor het eerst kwantificatie toe van lokale stroomdichtheden in Li-ion batterijelektroden onder realistische (ont)ladingsomstandigheden. De resultaten suggereren, dat de (ont)ladingsnelheid afhangt van de lokale stroomdichtheid, die was afgeleid uit de gemiddelde transformatietijden van individuele korrels.

Naast de directe beschouwing van faseovergangsgedrag van LiFePO_4 tijdens verschillende snelheden, werd in **Hoofdstuk 5** in-situ Neutron Diepte Profilering (NDP) uitgevoerd voor het eerst aan conventionele Li-ionenbatterijen, wat directe waarnemingen oplevert van de evolutie van het concentratiegradient van Li-ionen in LiFePO_4 elektroden bij verschillende elektrochemische omstandigheden voor verschillende typen elektroden. De resultaten verschaffen unieke directe inzichten, die tot nu toe niet beschikbaar waren en laten zien welk ladingstransportmechanisme domineert onder welke omstandigheden. Er wordt aangetoond dat het snelheid begrenzende ladingstransportmechanisme, dat de interne weerstand en overpotentiaal van Li-ionen batterijen bepaalt, zowel van de elektrodesamenstelling afhangt als, verrassenderwijs, van de actuele (ont)ladingsnelheid. De resultaten verschaffen zowel fundamentele inzichten die huidige elektrodeladingstransport modellen tarten, als praktische richtlijnen voor elektrodeontwerp voor verbeterde batterijprestatie. Bij lage (ont)ladingsnelheden blijken LiFePO_4 nucleatiebarrières begrenzend, lagere nucleatiebarrières aantonend voor kleinere deeltjes. Bij intermediaire snelheden toont depletie aan de collector zijde van de elektrode dat de ohm'se elektronische weerstand in de elektrode begrenzend is, een onverwacht resultaat met belangrijke implicaties. In tegenstelling daarmee, laten bij hoge (ont)ladingsnelheden de waargenomen Li-ionenconcentratiegradiënten zien dat

ionendiffusie door de poreuze elektrodematrix begrenzend is. Deze resultaten tonen dat afhankelijk van de aangebrachte (ont)lading een verschillende route gekozen moet worden om de interne weerstand te verlagen, en daarmee betere snelheidsprestaties en overall efficiency.

Met het oog op de ontwikkeling van een goedkoop materiaal voor de negatieve elektrode werkzaam juist binnen de stabiliteitslimiet van veelvoorkomende vloeibare elektrolyten, werden de elektrochemische eigenschappen van de Magnéli-fase rutiel-achtige structuur Ti_4O_7 bestudeerd in **Hoofdstuk 6** met toepassing van zowel elektrochemische tests en DFT berekeningen. Onze galvanostatische (ont)ladingsexperimenten tonen dat carbon coating is een van de mogelijke manieren om de elektrochemische prestatie van het Ti_4O_7 systeem te verbeteren, hoogstwaarschijnlijk omdat het de elektronische geleiding op het oppervlak verhoogt en de overall elektronische geleiding van de elektroden verhoogt. Zowel de DFT berekeningen en experimentele studies aan het Ti_4O_7 materiaal resulteerden in een gemiddeld voltage van ~ 0.9 V. Dit is betrekkelijk laag vergeleken met andere titanium oxiden, wat toegeschreven kan worden aan de structuur met zuurstofdefecten, die leidt tot een toename van de bandenergie van de laagste bindingselektronen. Als resultaat wordt de gemiddelde potentiaal gevonden binnen het stabiliteitswindow van veelgebruikte elektrolyten, suggererend dat een lange levensduur bereikt kan worden, waardoor dit materiaal van belang wordt voor Li-ionenbatterijen.

Samenvattend heeft de multitechnische benadering in dit proefschrift geleid tot een consistente en coherente beschrijving van snelheidsafhankelijk gedrag van individuele $LiFePO_4$ korrels en volledige elektroden. Voor het eerst werden in operando microbeam Röntgendiffractie en Neutron Diepte Profilering uitgevoerd. De resultaten illustreren de unieke mogelijkheden van deze technieken, doordat zij transformatiegedrag van individuele deeltjes en het ladingstransportmechanisme in Li-ionen batterij elektroden onder realistische in operando omstandigheden onthullen, die een richtlijn geven voor toekomstige research and development voor batterijen en vaste-stofmaterialen.

Acknowledgement

Finally, after five years' study and research, I begin to write this part of my thesis, which also means the coming end of my PhD life in the Netherlands. Since the first day I landed at Amsterdam Schiphol Airport I received many supports from a lot of friends who helped me, encouraged me and stood by me all the time. Without them I could hardly imagine how my life would be. Herewith, I would like to express my gratitude to all of you as follow.

First of all, I would like to thank my supervisor Dr. Ir. Marnix Wagemaker for his continuously support and remarkable guidance throughout my PhD research. I still remembered the first day we met through Skype interview and the day you told me I was enrolled as a PhD student at TU Delft. It was you, who opened the gate to me, gave me the opportunity to see the world and lead me here. I have to admit, before I came here I knew nothing about the battery and you turned me greatly from a layman to a qualified battery researcher. I always told my friends that you were the smartest guy I have met ever since. Whenever I came to you with problems, you always gave me a quick response directly to the point and told me how you got this solution as well. Besides, you always respected my opinion no matter how 'silly' it was. I have been inspired by your vision and attitude in scientific research all the time. The most precious things I learned here were not the knowledge and the skills, although they do very important, but the ability of thinking and the way of doing research. Those were treasures you gave to me. Thank you Marnix! Whenever you came to China, you were one of the most welcomed friends to me and I would very much like to open the 'Chinese gate' to you, which was also fantastic.

I also would like to express my gratitude to my promotor Prof. dr. Fokko M. Mulder for his stimulating discussion and helpful suggestion when we sat together. You also showed me the solid background of batteries with great idea and willing to help me solve the problem. Meanwhile, your concerned about my research

progress reminded me work hard and gave me encouragement as well. Your efficiency of correcting my thesis helped me a lot in the last few months.

A special thanks goes to Dr. Ir. Niels H. van Dijk. You were very friendly to everybody and were perfect people to work with as well as to talk with. I admired your solid knowledge of phase transition and radiation defective skills, which also helped me a lot in our synchrotron experiment and subsequent data analysis procedures. Besides the research discussion, I also enjoyed very much of talking with you on other aspects. You always enlighten me in various aspects and suggested me much in my life. When you come to China, let us continue our talk and I would very much like to show you around as I promised to you.

Besides my promotor and supervisor, I would like to thank other committee members who attend my thesis defense: Prof. dr. E. H. Brück, Prof. dr. ir. J. E. ten Elshof, Prof. dr. S. J. Picken, Prof. dr. C. Masquelier and Dr. ir. N. H. van Dijk. Thanks for your time and efforts spent on this thesis.

I am very grateful to people in our batter group: Dr Swapna Ganapathy, Dr. Deepak Singh, Dr. Kun Shen (申坤), Dr. Alexander Lyedovskykh, Frans Ooms, Michel Steenvoorden, Yaolin Xu (徐耀林), Zhaolong Li (李兆龙), Chuang Yu (余创), Bo Peng (彭勃), Tomas Verhallen, Martijn van Hulzen, Alexandros Vasileiadis, Peter-Paul Harks, Niek de Klerk, Frieda Davey, Remco van der Jagt. Thanks a lot for the help during the last five years and I enjoyed the work with you guys very much. Some members I would like to thank particularly. Swapna and Deepak were very friendly and supportive to me with their expert in batteries and materials. I really benefit a lot. Martijn and Tomas, thanks a lot for your help in Synchrotron and NDP data analyze. Without your contributes some of the work would not be possible as they were. I also enjoy the smoking time chat with you Tomas. Let's do it also in China. I would like to thank Yaolin Xu (徐耀林), Zhaolong Li (李兆龙), Chuang Yu (余创), Bo Peng (彭勃), not only for your help in the research but also the help of my thesis. Thanks Zhaolong(李兆龙) for the help on the thesis edit and the discussion which also enlighten me greatly. Thanks Bo Peng (彭勃) for your

wonderful help on the cover design of this thesis. It looks great. My special thanks goes to Kun Shen (申坤). You helped me a lot since I was in the group. You helped me to improve the battery knowledge and experiment skills start from scratch. You discussed the problem with fully support every time I came to you. I also enjoyed the talking with you in the afternoon when I felt tired and we did a lot of nitpick for so many events. That was a very good memory to me. You kept on helping me after you got your PhD and went back to China, like job hunting and so on. As now you were settled down in Beijing with your husband Dr. Hao Chen(陈浩), another good friend of mine, I wish you a better life and expect visiting to you soon.

I would like to take this opportunity to thank Dr. Jouke Heringa. He was always willing to help me when I need him, not only for work but also for some problem in life. During last five years, some Dutch mails and polices made me really very confuse and crazy, he always gave me a hand at that time. Also I would like to thanks for his help of translating the summary and propositions to Dutch words. Thanks Jouke!

I would like to thank Michel Steenvoorden, Kees Goubitz, Anton Lefering and Frans Ooms, Dr. Jonathan P. Wright (beam scientist in ESRF, Grenoble, France), for their technical support. I am also grateful to Ilse, Nicole and Trudy for their constant help to arrange everything for our group. Thanks also need go to Freek Labohm who guided me the NDP technique and made us the first group who could do the in-situ NDP measurement in conventional Li-ion battery in the world. Thanks are also address to my officemate and colleagues in FAME group. I am very lucky to work with you and to be a member of our research group. I am grateful to my officemate Prasad Gonugunta, Tang Nguyen and Jurrian H. Bakker. I also would like to thanks: Dr Zhiqiang Ou(欧志强), Dr. Shasha Zhang(张莎莎), Dr. Romain Blonde, Dr. Lei Ma(马磊), Prof. dr. Guihong Geng(耿桂宏), Dr. Guanglin Wang(王广林). Dr. Ming Ding(丁明), Dr. Lian Zhang(张练), Dr. Jie Yang(杨洁). Dr. Anna Grezech. Dr. Anca Anastasopol, Dr. Chao Wu(吴超), Dr. Lei Wang(王磊),

Haixing Fang(方海星), Wenqin Shi(施文琴), Yibole(伊博乐), Bouwer Huang(黄博微), Hongde Luo(罗宏德), Tiantian Yao(夭甜甜), Bei Tian(田北), Sibao Chen(陈思博). Thanks the couple Xuefei Miao(缪雪飞) and Fengjiao Qian(钱凤娇) from my Alma Mater, NUAA. For all of you, I enjoyed everyday we work together and this will always be a happy memory to me.

A lot of Chinese friends also made me a better life during the past five years and I need to enlist some of your name and our story as well.

Dr. Haiqiang Wang(王海强), we have known each other for more than 10 years since 2004 when we were studied in NUAA. At that time, I gave you the guidance as you were a freshman and I was a sophomore. Now you have already got your PhD diploma from TU Delft one year ahead of me and star your new life in Shanghai. You are a lucky bastard, aren't you! It was you who convinced me to choose TU Delft for my PhD study when I was agitated with my application for PhD positions in North American. You arranged the good accommodation for me at the very beginning when I arrived at the Netherland. As you said you were also the one who stand by me without any hesitant no matter what happened. I really appreciated that a lot. Although, at most of the time, I am the one who offered help. Now your wife, Dr. Qi Wu(吴琦), is going to give birth. Your daughter 'Muxin' (牧星) will soon join your family (ps: Please try to pronounce her name in an appropriate way). I would like to give my greeting to her as well. I am also looking forward to see her soon when I come back to China.

'Dr Zhou Zhou'(周舟) , when I stand on the platform for my thesis defense I am pretty sure you have already got your appointment for your defense date and will get your PhD degree soon after me. It is very lucky that I didn't make you a second 'Dr Wang' who graduated earlier than me but came later than me. As I do not want to admit you have a good talent amount most of the people I recognized, I will ascribe all your successes to your luck. For you, I would like to say 'a friend in need is friend indeed'. To me you are a brother more than a friend. During the most struggling time of mine in the past four years, you were the one who helped

me cheer up. Although sometimes your methods were not 'positive', as you taught me how to smoke, I enjoyed the freely talk in the smoking room with you everyday, where we talked a lot, shared a lot and I did learn a lot from you. Now I could view from different aspects and did not make so many stresses to myself. I know for sure wherever you were we will meet quite often later, cause we all need one person to talk, to drink and also to smoke like each other. Sooner after your defense I think we will meet in Shi Men at your wedding with Shan Shen (申珊). Congratulations to you in advance. Only one advice to Shan Shen (申珊) that do not lay him down in your bed after he got drunk. That is really something.

Also I would like to give my grateful to my friends in our group of '追梦赤子心'. Dr. Ke Tao (陶克), the legend of drinking during our party everytime. You still own me some white wins do you remember? Dr. Yongjia Li (李泳佳), gigantic wet, remember I told you, whenever you come to me you are always the VIP. Captain Mo (莫易雳), the future Chinese fighter planes designer, don't let us down. Xinyuan Mao (毛新愿), the chairman of ACSSNL and Dr. Beer, I would say I prefer your stout more than your IPA. Wish you a better life at TU Delft for the next 3 or 4 years with your wife Feifei Song (宋菲菲). Take it easy and don't be hurry. Also I would like to thank Zhijie Ren (任之劫), the team leader of 'Meng Meng Da' music band, and his girlfriend Yu Xin (辛瑜). I hope the next time I see you, you will not fall asleep during drinking. Don't do this as gigantic wet.

The grateful also give to my warcarft 3, DOTA, hearthstone and hero of the storm friends. They are Tianshi Lu(陆天石), Yanqing Hou(侯燕青), Yongjia Li (李泳佳), Xinyuan Mao (毛新愿), Hao Cui (崔浩), Zhaolong Li (李兆龙) and Zhou Zhou(周舟). I like to play with all of you especially with Tianshi Lu(陆天石) who shared the same interests with me and possess the comparable ability to me. I will miss the IKEA dinner with you and Zhou Zhou(周舟) although the meatballs were not so

delicious as they were. I still remember how excited the first time we got the legend cardback with you guys, however, some people are still struggling with that card back and you know whom I refer to. I still remember the DOTA night long time ago with little frog Hao Cui(崔浩) and our carry Xinyuan Mao (毛新愿).

Next time when we play DOTA again I would like to play carry for you guys and please share me with the 'chicken and eyes'. I also remember those days we played Hero of The Storm with God Long (李兆龙). Trust me I do remember those hard days and the worst illidan in Europe.

Furthermore, I would like to give my grateful to other people who also helped me a lot. They are Dr. Haoliang Huang (黄浩良) and his wife Qiwen Deng (邓绮文), Dr. Ping Liu (刘平) and his wife Dr. Yan Ni (倪燕), Dr. Huajie Shi (石华杰) and his wife Dr. Lu Zhang (张璐), Dr. Lu Wang (王璐) and her husband Shuzheng Wang (王树正), Dr. Xun Gong(功勋) and his wife Dr. Xuefei Mei(梅雪飞), Dr. Hao Cui (崔浩) and his wife Xinhui Xiang (向沁卉), Long Xu (徐龙) and his wife Mengting, Xiaojia Zhao (赵晓霞), and her husband Shuanghou Deng (邓双厚), Chang Wang(王菡) and his wife Jiajing Yao(姚嘉静). You have all shown me the good examples of making happy families. Although I missed this before, I would not let it go from now on. Special thanks to Dr. Hao Cui (崔浩) for his help and his look after for me in Delft and continues concerned after he moved to Oxford. I am very proud to be the godfather of your son Yu Cui (崔榆). It is sad that I do not have chance to go to England to see him face to face but I will fulfill my duty when you came back to China. Also I would like to tell Dr. Ping Liu (刘平), I am willing to see you and Yan Ni (倪燕) in Shanghai University if I finally get that job. I also would like to thank Feijia Yin(尹飞佳) Wei Meng(孟伟), Lei Shi(石磊), Chang Wang(王畅), Yu Hu(胡宇), Wenbo Zhang (张文博), Zenan Yang(杨泽男), Tianqi Fei(费天祁), Xin Guo (郭昕), Daquan He(何大全), Honglin Chen(陈洪林)... Due to the limited space, it is

not possible to list all the names here but I would like to express my humble thanks to all the people I know. The experience we had together will benefit me and will always be my treasure for all my rest of life

The China Scholarship Council (CSC) is acknowledged for its financial support for this study. The thanks also give to Franca Post and Cees Timmers from CICAT for their arrangement before and during my stay in the Netherlands.

Last but not the least, I would like to express my deep sense of gratitude and sincerely appreciated to my parents, grandparents and all the other my family members. Whatever I did, wherever I was, your always stood with me, supported me and encouraged me. I am who I am because of you. Without you I would get nothing but failure. I know I used to let you down, brought very difficult time to you and left a lot of troubles to you. I hope these would never happened and I will become the backbone of our family from now on. I love you forever.

最后，发自内心的感谢我的父母,我的爷爷奶奶和我所有亲人。无论我做错了什么你们总是在我身边，鼓励我，支持我。正是因为有你们的支持我才能一路走到今天。我会记住曾经给你们带来的困扰，失望，伤心。我希望这些不开心的经历能够永远的成为过去，希望从今以后我能够成为你们的强有力的支柱，撑起我们整个家。我爱你们，爸爸妈妈。

Xiaoyu Zhang(张晓禹)

November 2015

Delft, the Netherlands

List of publications

1. **Xiaoyu Zhang**, Martijn van Hulzen, Deepak P. Singh, Alex Brownrigg, Jonathan P. Wright, Niels H. van Dijk, and Marnix Wagemaker* ;

'Rate-Induced Solubility and Suppression of the First-Order Phase Transition in Olivine LiFePO₄'; *Nano Letters*, 14, 2279-2285, (2014)

2. **Xiaoyu Zhang**, Tomas W. Verhallen, Freek Labohm, and Marnix Wagemaker* ;

' Direct Observation of Li-ions under Non-equilibrium conditions by In-situ Neutron Depth Profiling'; *Advanced Energy Materials*, 5, 1500498-1500505 (2015)

3. **Xiaoyu Zhang**, Niels H. van Dijk, Martijn van Hulzen, Deepak P. Singh, Alex Brownrigg, Jonathan P. Wright, and Marnix Wagemaker* ;

'Direct view on the phase evolution in individual LiFePO₄ nanoparticles cycling of Li-ion battery electrode'; *Nature Communication*, 6, 8333, (2015)

Curriculum Vitae

Xiaoyu Zhang (张晓禹) was born on 24th of July 1984 in XuZhou, JiangSu Province, China. In 2003 after graduating from the Xuzhou Number One Middle School, he entered the department of Applied Physics in Nanjing University of Aeronautics and Astronautics (NUAA), China. In 2007 after he got his bachelor degree in applied physics he continued his studied in NUAA for his master degree. Three years later, in 2010, he got his master degree in the Condensed Matter Physics supervised by Prof. Xiaohong Yan (颜晓红). After seven years' studied and lived in Nanjing he moved to the Netherlands and started his PhD research from September 8th, 2010. He joined the group of Fundamental Aspect of Materials and Energy (FAME) at Delft University of Technology and focused his research on Li-ion batteries that supervised by Dr. Ir. Marnix Wagemaker and Prof. dr. Fokko Mulder. After five years research this thesis finally resulted.